

VARIATIONAL APPROACHES FOR DESPECKLING AND DEBLURRING OF IMAGES

Thesis

Submitted in partial fulfillment of the requirements for the degree of

DOCTOR OF PHILOSOPHY

by

BALAJI BANOTHU



DEPARTMENT OF MATHEMATICAL & COMPUTATIONAL SCIENCES

NATIONAL INSTITUTE OF TECHNOLOGY KARNATAKA

SURATHKAL, MANGALORE - 575025

October, 2018

Dedicated to...

*My beloved parents
and family members...*

&

All of my Teachers and Colleagues...

DECLARATION

By the Ph.D. Research Scholar

I hereby *declare* that the Research Thesis entitled **VARIATIONAL APPROACHES FOR DESPECKLING AND DEBLURRING OF IMAGES** which is being submitted to the **National Institute of Technology Karnataka, Surathkal** in partial fulfillment of the requirements for the award of the Degree of **Doctor of Philosophy in Mathematical and Computational Sciences** is a *bonafide report of the research work carried out by me*. The material contained in this Research Thesis has not been submitted to any University or Institution for the award of any degree.

Balaji Banothu

Reg. No.: 148051 MA14F02

Department of Mathematical and Computational Sciences

Place: NITK, Surathkal.

Date: October 26, 2018

CERTIFICATE

This is to *certify* that the Research Thesis entitled **VARIATIONAL APPROACHES FOR DESPECKLING AND DEBLURRING OF IMAGES** submitted by **BALAJI BANOTHU**, (Reg. No.: 148051 MA14F02) as the record of the research work carried out by him, is *accepted as the Research Thesis submission* in partial fulfillment of the requirements for the award of degree of **Doctor of Philosophy**.

(Dr. Jidesh P.)

Research Supervisor

Chairman - DRPC

ACKNOWLEDGEMENT

I would like to take this chance to thank those people who have made this thesis possible.

My deepest gratitude and appreciation goes first and foremost to my supervisor, *Dr. Jidesh P.*, Department of Mathematical and Computational Sciences, for all the generous support and precious guidance throughout my doctoral work. All your constant encouragement helped me to focus on my research for which I deeply thank you. It has been my honor to work with you.

I extend thanks to my RPAC members, *Dr. Pushparaj Shetty D.*, Department of Mathematical and Computational Sciences and *Dr. Shyam Lal*, Department of Electronics and Communication Engineering, for going through all my reports and giving valuable suggestions, which improved this research work. Also, I thank to *Prof. Mahmoud El-Sakka*, Department of Computer Science, University of Western Ontario, London, Canada and *Prof. Manas Kamal Bhuyan*, Department of EEE, IIT Guwahati, India, for evaluating my thesis and appreciating my work.

I am thankful to *Prof. Santhosh George*, former Head of the Department of Mathematical and Computational Sciences and *Prof. B.R. Shankar*, Head of the Department of Mathematical and Computational Sciences, for providing better facilities and extending good infrastructural support for the research activities in the department. I also thank all the teaching and non-teaching staff for all their support and help.

I take this opportunity to thank my fellow research scholars of the Department of Mathematical and Computational Sciences for making my stay at NITK wonderful and memorable.

Finally, I am thankful to my parents, wife, brother, sisters, daughters and friends for accepting my decision of opting for Ph.D. Their support was always there, as expected.

Place: NITK, Surathkal

Balaji Banothu

Date: October 26, 2018

ABSTRACT

Speckle reduction is an inevitable pre-processing activity in some of the medical and satellite imaging modalities. This work is dedicated to study the behaviour of speckles and reduce them in medical ultrasound images and synthetic aperture radar images. Three novel methods have been proposed in this thesis to despeckle and deblur the input data. The first two models being proposed are variational frameworks, where a constrained optimization problem is derived with an appropriate objective functional and a set of constraints. The behaviour of the objective functional deeply influences the restoration process. A non-local total bound variational prior is designed in the first place to restore the images from their speckled observations. This objective functional designed using this prior, duly respects the gradient oscillations due to edges in the images while despeckling them. The theory behind the design of the constrained optimization problem lies in the Bayesian maximum a posteriori estimation process, which is re-designed to suit the optimization problem under consideration. The noise distribution plays a vital role in the design of the functional, optimizing which leads to the desired solution eventually. In the second model, the energy (optimizing) functional is designed as mentioned earlier, however, the objective functional is a modified version of the well known Mumford Shah model. Though, Mumford Shah level-set model has been extensively used for image segmentation, its capacity to restore the data is being duly analyzed in this thesis. A controlled evolution of the level-sets under a well designed data-fidelity, duly despeckles and deblurs the data in the course of the evolution. These two variational regularization models are theoretically analyzed to study the conditions for existence of unique solution. The third model, is based on the Gradient fidelity of the image function and it duly alleviates speckles and blur from images while checking the possibility of a piecewise linear approximations which leads to visual discrepancies in the restored data. All models described in the thesis are experimentally verified using a large set of input data from ultrasound and synthetic radar imaging applications. Furthermore, the performance of these models along with the ones in the literature are statistically quantified. The required mathematical preliminaries, definitions and derivations have been incorporated in the Appendix for a seamless reading of this thesis.

Keywords: Image restoration; Gamma noise; Split-Bregman; Total bounded variation, Level-Set, Gradient fidelity.

Contents

Abstract	i
List of Figures	vi
List of Tables	ix
Nomenclature and Abbreviations	xi
1 INTRODUCTION	1
1.1 Image Degradations	2
1.1.1 Blurring defects	2
1.1.2 Noise Models	4
1.2 Analysis of a Speckle Noise Distribution	8
1.3 Data Correlated Noise Distribution	8
1.4 Motivation	11
1.5 Research Objectives	12
1.6 Organization and Contribution of the Thesis	14
2 IMAGE DESPECKLING METHODS	17
2.1 Statistical Despeckling Methods	17
2.1.1 Minimum Mean Square Error Based Non-iterative Adaptive Filters	17
2.2 PDE approaches	20
2.2.1 Anisotropic Diffusion Filter	20
2.2.2 Speckle Reducing Anisotropic Diffusion Filter	21
2.2.3 Details Preserving Anisotropic Diffusion	22
2.2.4 Oriented Speckle Reducing Anisotropic Diffusion (OSRAD) Filter	23
2.3 Wavelet Transforms for Speckle Reduction	25
2.4 Variational Model for Image Restoration Under an Additive Noise	26

2.4.1	Total Variation Regularization	26
2.4.2	Higher order PDEs for Image Restoration	28
2.5	Variational Models for Image Restoration Under Multiplicative Noise	31
2.5.1	Total Variation Model for Multiplicative Noise	32
2.5.2	Image Restoration in Log Compressed Domain	33
2.5.3	A Variational Model for Gamma Distribution	34
2.5.4	A Convex Regularization Model for Multiplicative Noise	35
2.5.5	Multiplicative Noise Removal via a Novel Variational Model	35
2.5.6	A Convex Regularization Model for Image Restoration	36
2.6	Non-local Total Variation (NLTV) Regularization	37
3	DESPECKLING ULTRASOUND IMAGES USING NON-LOCAL TOTAL BOUNDED VARIATION REGULARIZATION	39
3.1	Introduction	39
3.2	Contributions of the Proposed Model	40
3.3	The Proposed Variational Speckle Reduction Model	41
3.4	Numerical Implementation using Augmented Lagrangian	41
3.5	Experimental Results and Discussion	43
4	SPECKLE REDUCING LEVEL-SET APPROACH	59
4.1	Introduction	59
4.2	Speckle Reducing Level-Set Approach	60
4.3	Split-Bregman Iterative Scheme for the Model	63
4.4	Experimental Results	65
5	NON-LOCAL GRADIENT FIDELITY MODEL FOR MULTIPLICATIVE GAMMA NOISE REMOVAL	79
5.1	Introduction	79
5.2	The Proposed Non-Local Gradient Fidelity Model	81
5.3	Numerical Implementation of the Model	83
5.4	Experimental Results and Discussions	84
6	CONCLUSION AND FUTURE SCOPE	91
6.1	Concluding Remarks	91
6.1.1	Comparative analysis of the proposed models	92

6.2	Future Research Directions	94
Appendix A		95
A.1	Ultrasound Images	95
A.1.1	Ultrasound Image Formation	95
A.1.2	The Parts of an Ultrasound Machine	96
A.2	Synthetic Aperture Radar Images	98
A.2.1	Applications of the Synthetic Aperture Radar Imaging Systems	100
Appendix B		101
B.1	Theoretical Analysis of the Model	101
B.1.1	Existence and Uniqueness	102
B.2	Derivation of the MAP Estimator	104
B.3	MLE of Noise Parameters	105
B.4	Evaluation and Update of λ	107
B.5	Convergence Analysis	108
Appendix C		109
C.1	Existence of a Unique Solution	109
C.1.1	Ambrosio Tortorelli Approximations	110
Appendix D		113
D.1	Sample code of Augmented Lagrangian for Non-local Total Variation .	113
	Bibliography	117
	List of Publications	126

List of Figures

1.1	A model of the image degradation/restoration process.	2
1.2	Original cameraman image corrupted with different blurs	4
1.3	PDF of a Gaussian noise	5
1.4	PDF of a Rayleigh distributed noise	6
1.5	PDF of a Gamma distributed noise	7
1.6	Histogram of a selected region plotted for synthetic images corrupted with different noise	9
1.7	Intensity AIRSAR image, HH polarization, three looks	10
1.8	Intensity AIRSAR image, HH polarization, three looks	10
1.9	Original 1-Dimensional Data	12
1.10	Original synthetic image corrupted with noise and blur	13
2.1	Original phantom image	24
2.2	Original Lena image corrupted by Gaussian noise	31
3.1	Original Lena and Satellite images	47
3.2	Lena image	49
3.3	Synthetic image	50
3.4	Satellite image	51
3.5	Original Liver image	52
3.6	Original hepaticvein image	53
3.7	Original Kidney image	54
3.8	Original women breast image	55
3.9	Relative Error	56
3.10	Synthetic image	57

4.1	Original SAR image and corresponding histograms	73
4.2	Original SAR-Lynx image	74
4.3	Phantom image	75
4.4	Original Flevoland SAR image	76
4.5	Phantom image	77
4.6	Original Flevoland enlarged portion of the SAR image	78
5.1	Phantom image	87
5.2	Peppers image	88
5.3	Original noisy ultrasound image of a woman breast	89
5.4	Original SAR image from the Sandia National Laboratory	90
6.1	Comparative analysis of the proposed models by using lenna image	94
A.1	Ultrasound image of a growing fetus inside a mother's uterus.	96
A.2	The parts of an ultrasound machine.	97
A.3	Basic Block Diagram of Radar System	99
A.4	ERS Satellite SAR image	99

List of Tables

3.1	PSNR values of different images	47
3.2	SSIM values of different images	47
3.3	Number of iterations	48
3.4	Different parameter values of natural images	48
3.5	Different parameter values of US images	48
4.1	KL and JS divergence values for different regions of image	67
4.2	Quantitative evaluation of filters for the synthetic image	70
4.3	Quantitative evaluation of the second order statistics for the Synthetic data	71
4.4	Quantitative evaluation of the second order statistics for the real SAR (Flevoland image) data	71
4.5	Quantitative evaluation of the second order statistics for the real SAR (San Francisco bay image) data	71
4.6	Different parameter values used for the real test images (Phantom image and AIRSAR image) under various restoration models.	71
5.1	Number of iterations	85
5.2	PSNR values of different images	86
5.3	SSIM values of different images	86
6.1	PSNR values of different images	93
6.2	SSIM values of different images	93

Nomenclature and Abbreviations

Symbol notations followed in the Thesis

Matrices/two dimensional functions are denoted using **bold** case letters

Vectors are denoted using *bold-italic* letters

Scalars and functions are denoted using *italic* letters

Symbol	Representation	Symbol	Representation
\mathbf{u}_0	Input image	\mathbf{u}	Original image
\mathbf{n}	Noise matrices	σ	Standard deviation
ρ	Correlation coefficient	μ	Mean
*	Convolution operator	Ω	Image domain
BV	Bounded Variation	\mathbf{K}	Blurring operator
\mathbb{R}	Set of real numbers	Δ	Laplacian operator
Δ_{NL}	Non-Local Laplacian operator	∇	Gradient operator
∇_{NL}	Non-Local Gradient operator	div	Divergence function
div_{NL}	Non-Local divergence	∂	Partial derivative
$\ \cdot\ $	Euclidean norm	$ \cdot $	Absolute value
\prod	product	Σ	Summation
$\forall x$	for all the values of x	\mathbf{V}	Vector
\mathbf{z}	Gray Level	θ	Scale parameter
k	Shape parameter	$\hat{\mathbf{u}}$	Output image
\mathbf{W}	Weighted function	\mathbf{K}^*	The adjoint of the operator \mathbf{K}
λ	Regularization parameter	μ	Regularization parameter

Abbreviations and Expansions

BV	Bounded variation	SB	Split-Bregman
SAR	Synthetic aperture radar	US	Ultrasound
MAP	Maximum a posteriori	TV	Total variation
NLTV	Non-local Total Variation	PDF	Probability density function
PSF	Point spread function	ML	Maximum likelihood
IID	Identically and independently distributed	ISRAD	an improved speckle reducing anisotropic diffusion
AGWN	Additive gaussian white noise	NLM	Non-local means
CPU	Central processing unit	PET	Positron emission tomography
2D	Two-dimensional	ERS	European remote sensing
TBV	Total bounded variation	SURE	Stein's unbiased risk estimate
AA	Aubert and Aujol method	FANS	Fast adaptive nonlocal SAR
PPB	Probabilistic patch-based filter	ENL	Equivalent number of looks
KL	Kullback Leibler	JS	Jensen Shannon
BM3D	Block-matching and 3D transform	NLTBV	Non-local total bounded variation
MSE	Mean squares error	SSIM	Structural similarity index measure
PSNR	Peak signal to noise ratio	DPAD	Details preserving anisotropic diffusion
OSRAD	Oriented speckle reducing anisotropic diffusion	NLTVL	Non-local total variation by using Augmented Lagrangian method
AT	Ambrosio and Tortorelli	SRAD	speckle reducing anisotropic diffusion
MS	Mumford-Shah	SNR	Signal to noise ratio
RI	Ratio image	NLGF	Non-local gradient fidelity

Chapter 1

INTRODUCTION

Recovering of an original image from its distorted observation is a demanding task in various fields of imaging and image processing, such as Medical imaging, Satellite imaging, etc. The common degradations occur due to random fluctuations in the data (commonly termed as noise) and device related artefacts such as blur. Interference of these distortions occur during the acquisition (e.g. environmental conditions and quality of sensors), transmission (e.g. interference by lighting or other atmospheric disturbance) or processing (e.g. Image compression) of the data. Image restoration is literally an approximation problem, wherein we try to achieve an estimate of the original data from its distorted observation. Having said that, the proximity of the approximations depends on the accuracy of the model, thus simulated. Hence, a good approximation demands a proper modeling of the problem. As noticeable from the literature, restoration is an inverse problem which is generally ill-posed in the sense of Hadamard and Morse (1953) ¹. In other words, it is tedious to find the existence of a unique solution, even if one exists, it severely depends on the data or a small protuberance in the data causes large deviations in the solution, which eventually leads to irregularity in the solution. Therefore, prior information has to be pumped into the model to mollify the irregularity in the solution and improve the approximation. However, incorporating more assumptions regarding the a priori information weakens the model and results in a deviation from the actual scenario. In a nutshell, the prime objective of a restoration process is to retrieve images without losing meaningful features such as sharp edges, textures or fine details etc. The extent of challenge involved in this activity has attracted

¹(Hadamard and Morse, 1953) formulated the following conditions of well-posed problems. An inverse problem is said to be well-posed if the following three conditions are satisfied:

1. A solution exists.
2. The solution is unique.
3. The solution's behavior changes continuously with the initial conditions (stability),

the research community at large. A typical degradation/restoration model is portrayed in Figure 1.1.

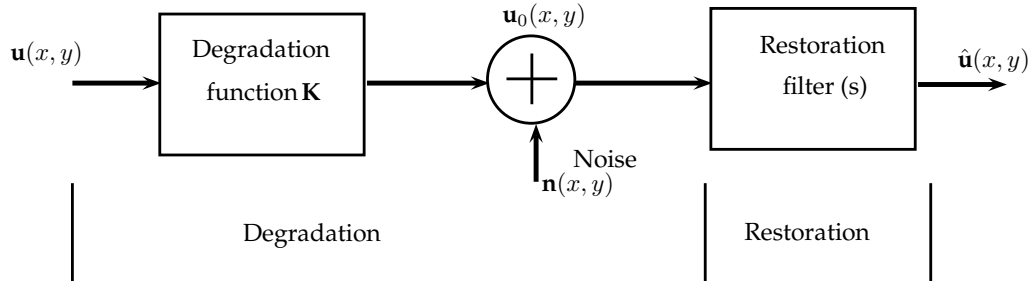


Figure 1.1 A model of the image degradation/restoration process.

1.1 Image Degradations

Images are generally degraded due to noise and blur. Blur is a common artefact integrated with the image formation. Blurring occurs due to various physical reasons, such as optical aberrations (out-of-focus blur), atmospheric distortions (including turbulence and aerosol scattering), movement of subject or object (motion blur), etc. (Gunturk and Li, 2012; Lu, 2017). When a real scene is imaged by a camera, some of the points are in focus while others not, this causes an out-of-focus blur. Out-of-focus blur is space-invariant in cases where the surface of a flat object is parallel to the image plane (Bertero and Boccacci, 1998). In addition to blur, image degradation is also caused by noise interference during image recording/transmission process.

1.1.1 Blurring defects

A blurred image \mathbf{u}_0 is being modeled as a linear system as follows:

$$\mathbf{u}_0(i, j) = \mathbf{K}\mathbf{u}(i, j), \quad (1.1)$$

where (i, j) represents spatial coordinates, $\mathbf{u}_0(i, j)$ is the observed image, which is noisy and blurred. \mathbf{K} is the blurring operator and $\mathbf{u}(i, j)$ is an original image. Equation (1.1) is rewritten in terms of a Point Spread Function (PSF) under the assumption of linearity and shift invariance as:

$$\mathbf{u}_0(i, j) = \mathbf{K}(i, j) * \mathbf{u}(i, j), \quad (1.2)$$

where $\mathbf{K}(i, j)$ is the PSF of the imaging system that causes blurring of image, and $*$ denotes two dimensional (2-D) linear convolution operation. PSF is the impulse response of an optical system subjected to a point source input.

The PSF of the shift-invariant or space-invariant out-of-focus blur (Hansen et al., 2006) is formulated as:

$$\mathbf{K}(i, j) = \begin{cases} \frac{1}{\pi r^2} & \text{if } (i-k)^2 + (j-l)^2 \leq r^2, \\ 0 & \text{elsewhere,} \end{cases} \quad (1.3)$$

where r is the radius of the blur and (k, l) is the center of the PSF.

Atmospheric blur or Gaussian blur is the distortion of image due to long time exposure, wind speed, fog and the random changes in the refractive index of the air through which light travels, see Hansen et al. (2006) for the details. The PSF for blurring caused by an atmospheric turbulence can be described as a two-dimensional Gaussian function, given by

$$\mathbf{K}(i, j) = \frac{1}{2\pi\sigma^2} e^{-\frac{i^2+j^2}{2\sigma^2}}, \quad (1.4)$$

where i is the distance from the origin on the horizontal axis, j is the distance from the origin on the vertical axis, and σ is the standard deviation of the Gaussian distribution.

Motion blur occurs when the image being recorded changes during the recording of a single exposure, either due to rapid movement or long exposure. The PSF of motion blur is defined as:

$$\mathbf{K}(i, j) = \begin{cases} 1 & \text{if } v_i j = v_j i, \text{ and } \sqrt{i^2 + j^2} = \sqrt{v_i^2 + v_j^2}, \\ 0 & \text{elsewhere,} \end{cases} \quad (1.5)$$

where the vector $V = (v_i, v_j)$ is the motion vector. The direction of V determines the orientation of $\mathbf{K}(i, j)$, and the magnitude of V determines the length of $\mathbf{K}(i, j)$. Figure 1.2 demonstrates the effect of various blurs on the input image. The image ‘‘cameraman’’ has been chosen for the representation purpose.

As seen in the previous works, the image formed under ultrasound (US) and Synthetic Aperture Radar (SAR) system are usually degraded by a Gaussian blur (modeled as linear and shift invariant).

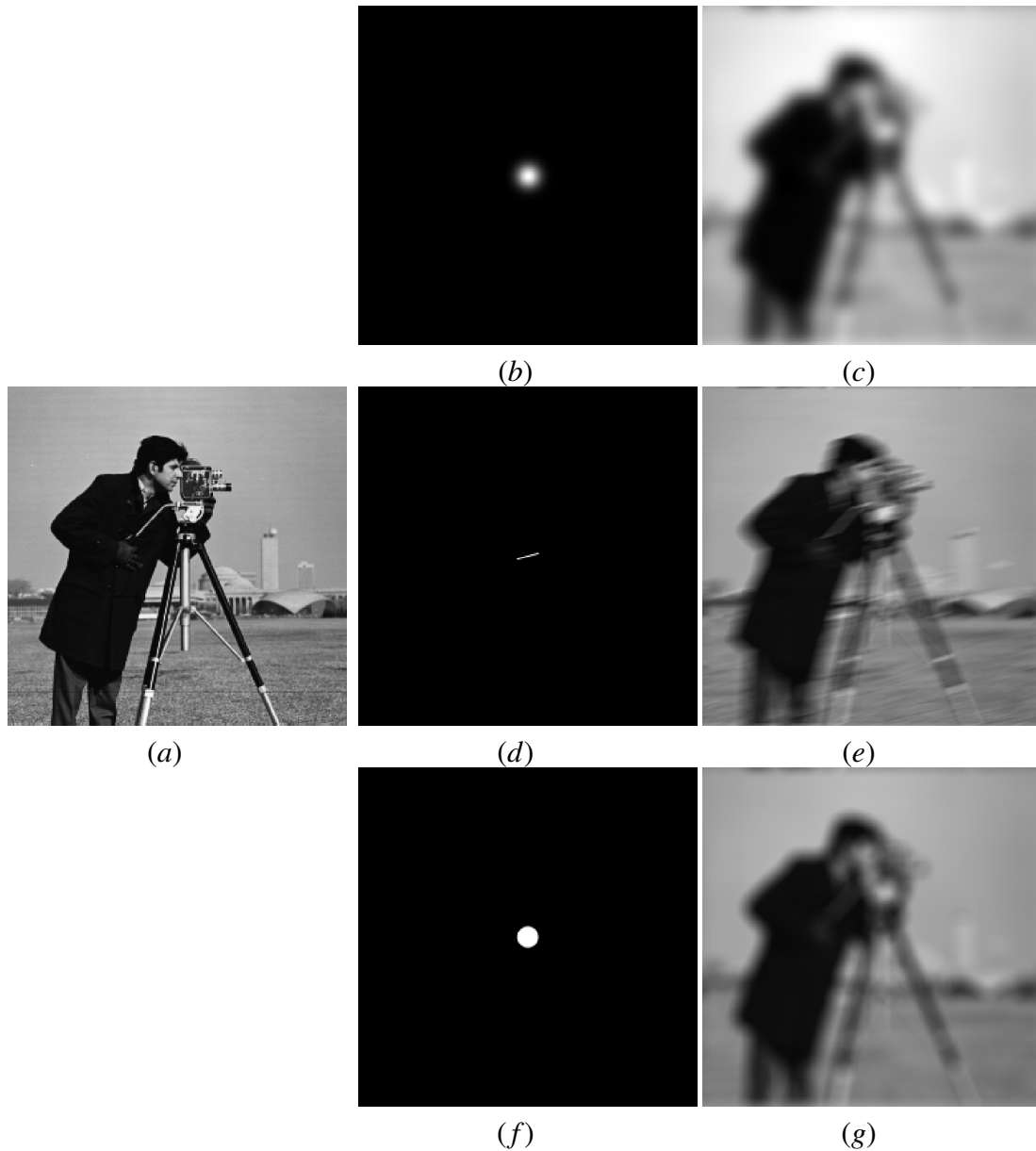


Figure 1.2 (a) Original image “cameraman” (b) PSF of an atmospheric blur (c) blurred due to the atmospheric interference (d) PSF of a motion blur (e) blurred due to the motion artefact (f) PSF of an out-of-focus blur (g) blurred due to the out-of-focus scenario.

1.1.2 Noise Models

Additive noise model

As already mentioned, \mathbf{u}_0 and \mathbf{u} are the observed and original images, respectively ² and \mathbf{n} is the zero mean additive noise which affects all pixels in the image, moreover, noise is identically and independently distributed (IID). The additive noise (in presence

²For the sake of clarity in the expressions we drop the index (i, j) from subsequent equations.

of a linear blur) is generally modeled as

$$\mathbf{u}_0 = \mathbf{K}\mathbf{u} + \mathbf{n}. \quad (1.6)$$

Here $\mathbf{K}\mathbf{u}$ denotes convolution of the blurring kernel/PSF \mathbf{K} with the original image \mathbf{u} . A zero mean Gaussian white noise is a good example of an additive noise model (Aubert and Kornprobst, 2002).

Gaussian White Noise:

A Gaussian noise also known as electronic noise is caused by natural sources such as sensor defects due to poor illumination or high temperature. The Probability Density Function (PDF) of a Gaussian function is:

$$p(\mathbf{z}|\mu, \sigma^2) = \frac{1}{\sqrt{2\pi}\sigma} e^{-\frac{(\mathbf{z}-\mu)^2}{2\sigma^2}}, \quad (1.7)$$

where \mathbf{z} is the gray level, μ is mean of random variable \mathbf{z} and σ^2 is the variance of \mathbf{z} . The Gaussian PDF for various parameter values is plotted in Figure 1.3.

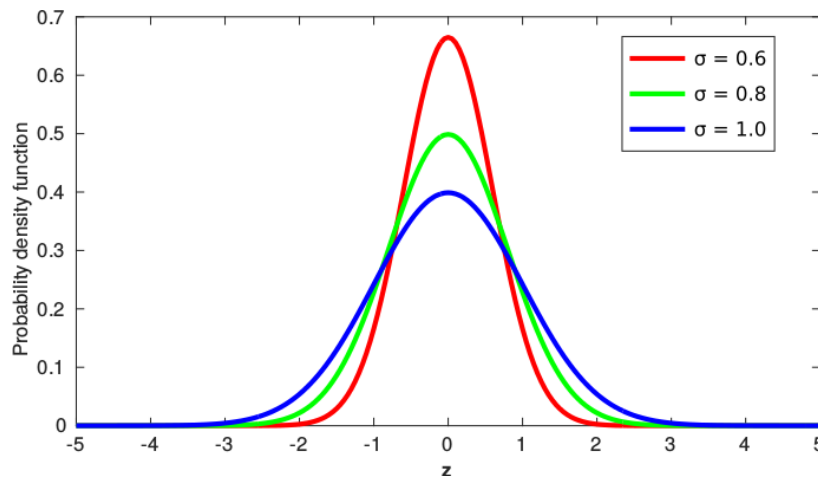


Figure 1.3 PDF of a Gaussian noise

Many efficient approaches have been proposed to reduce the additive Gaussian white noise in images. Among them, the most prominent ones are: stochastic approaches (Geman and Geman, 1984), wavelet approaches (Donoho and Johnstone, 1995a; Chan and Shen, 2005; Parrilli et al., 2012; Solbo and Eltoft, 2004), Partial Differential Equation (PDE) based approaches (Perona and Malik, 1990) and variational approaches (Rudin et al., 1992; You and Kaveh, 2000). Refer Chan and Shen (2005) for a detailed review of various restoration methods.

Restoration of images from additive Gaussian white noise is a well studied prob-

lem in the image processing literature. However, as observed in many previous works, the noise present in many medical and satellite imaging applications are found to be data-correlated. For instance, US and SAR images are found to be corrupted by data-correlated noise and more precisely it can be modeled as a multiplicative noise (Aubert and Aujol, 2008). The details are shared subsequently.

Multiplicative noise model

Multiplicative noise refers to an unwanted random data that gets multiplied to the true data during the capture or transmission of the image. A general multiplicative noise has the following model:

$$\mathbf{u}_0 = \mathbf{Kun}. \quad (1.8)$$

Here \mathbf{n} denotes a multiplicative noise. In the general Gamma noise and Rayleigh noise are multiplicative in nature, see Aubert and Aujol (2008) for the details.

Rayleigh Noise:

The Rayleigh noise is generally seen in the range based images. Its PDF is given by:

$$p(\mathbf{z}|\theta) = \begin{cases} \frac{\mathbf{z}}{\theta^2} e^{-\frac{\mathbf{z}^2}{2\theta^2}} & \text{if } \mathbf{z} \geq 0 \\ 0, & \text{if } \mathbf{z} < 0 \end{cases} \quad (1.9)$$

where mean $\mu = \theta\sqrt{\frac{\pi}{2}}$, variance $\sigma^2 = \frac{(4-\pi)}{2}\theta^2$ and $\theta > 0$ is the scale parameter of the distribution. The PDF of Rayleigh distribution is shown in Figure 1.4.

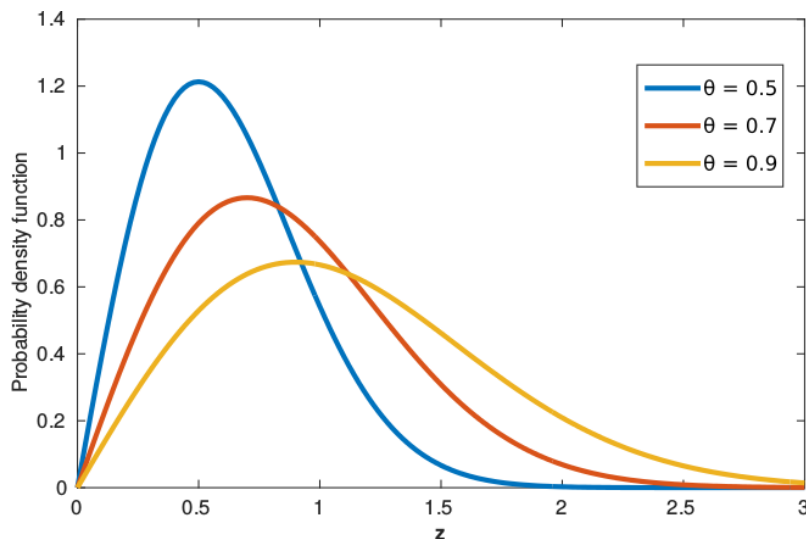


Figure 1.4 PDF of a Rayleigh distributed noise

Gamma Noise:

Gamma noise is generally seen in the laser based images. The PDF for Gamma distribution with shape parameter k and scale parameter θ is given by:

$$p(\mathbf{z}|k, \theta) = \begin{cases} \frac{1}{\Gamma(k)\theta^k} \mathbf{z}^{k-1} e^{-\frac{\mathbf{z}}{\theta}} & \text{if } \mathbf{z} \geq 0 \\ 0, & \text{if } \mathbf{z} < 0 \end{cases} \quad (1.10)$$

where $k, \theta > 0$, mean $\mu = k\theta$ and variance $\sigma^2 = k\theta^2$. Figure 1.5 shows the plot of Gamma PDF at various parameter values.

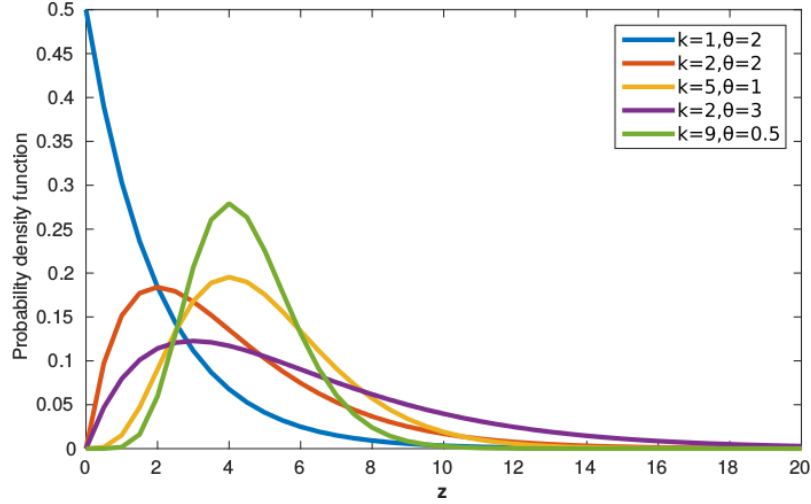


Figure 1.5 PDF of a Gamma distributed noise

Speckle Noise:

Multiplicative noise is commonly found in images obtained from many real-world image processing applications, such as laser imaging, microscopic imaging, SAR imaging, positron emission tomography (PET) and medical ultrasound imaging. SAR and medical ultrasound images are usually corrupted by a granular noise called speckle. The noise interference caused during the data recording process is being highlighted here. Figure 1.6 shows the histogram of a selected region extracted from a synthetic image corrupted by various noise distributions. For the multiplicative noise distributions, the dark regions in the image are contaminated more by the noise compared to the bright regions. However, for the additive Gaussian, the regions are uniformly contaminated. Owing to the data-independent nature of the noise. This thesis mainly focuses on restoration of the images corrupted by data-correlated speckle noise and linear blurring artefacts. The case study is mainly performed on US and SAR images due to their wide acceptability in medical and satellite imaging applications. A detailed description

of formation and representation of US and SAR images has been given in Appendix A.1,A.2.

1.2 Analysis of a Speckle Noise Distribution

As a primary step, it is required to analyze the distribution of the input noise. To this end a prior assumption is made regarding the distribution and a testing is performed to analyze the same. As observed in the literature, the speckles follow a Gamma law. If this argument can be substantiated with the input test data, then the model can be designed for the speckle distortion under the assumption that it follows a Gamma distribution. To justify this argument, homogeneous intensity regions (as the variance in such regions are mainly due to noise intervention) were extracted from the input noisy SAR and US images which are shown in Figures 1.7 and 1.8. The method discussed in Gomez et al. (2017) is adopted for finding the homogeneous regions. Next, the histogram of the pixels in the extracted regions is evaluated and the PDF is analyzed. Further, the parameters (scale and shape) were estimated using maximum likelihood (ML) estimator (See Appendix B.3 for the details of ML estimation of parameters of a Gamma distribution), assuming a Gamma distribution for each of the regions of interest, Gamma PDF curves were plotted with the estimated parameters. Finally, it is observed that the PDF (curves) generated from the histograms of the input noisy regions (extracted from the noisy image) closely resembles the PDF (curves) generated assuming the Gamma distribution with the estimated parameters: scale and shape using (B.29) and (B.30), respectively. This analysis is carried out using a large set of input US and SAR images collected from various sources before making conclusions regarding the PDF of the noise.

1.3 Data Correlated Noise Distribution

Multiplicative noises are much more difficult to eliminate from the degraded images, as the noise becomes correlated with the data. The noise variance changes with respect to the underlying intensity characteristics. The noise variance is high at high intensity regions whereas it is low at the other regions. The distribution of a multiplicative and an additive noise are provided in Figure 1.9, which shows a one-dimensional signal (in its original form) and the one corrupted by additive Gaussian noise and multiplicative Gamma noise, respectively. From these demonstrations, one can observe that much crucial information has been distorted in case of the Gamma noise corruption. Figure

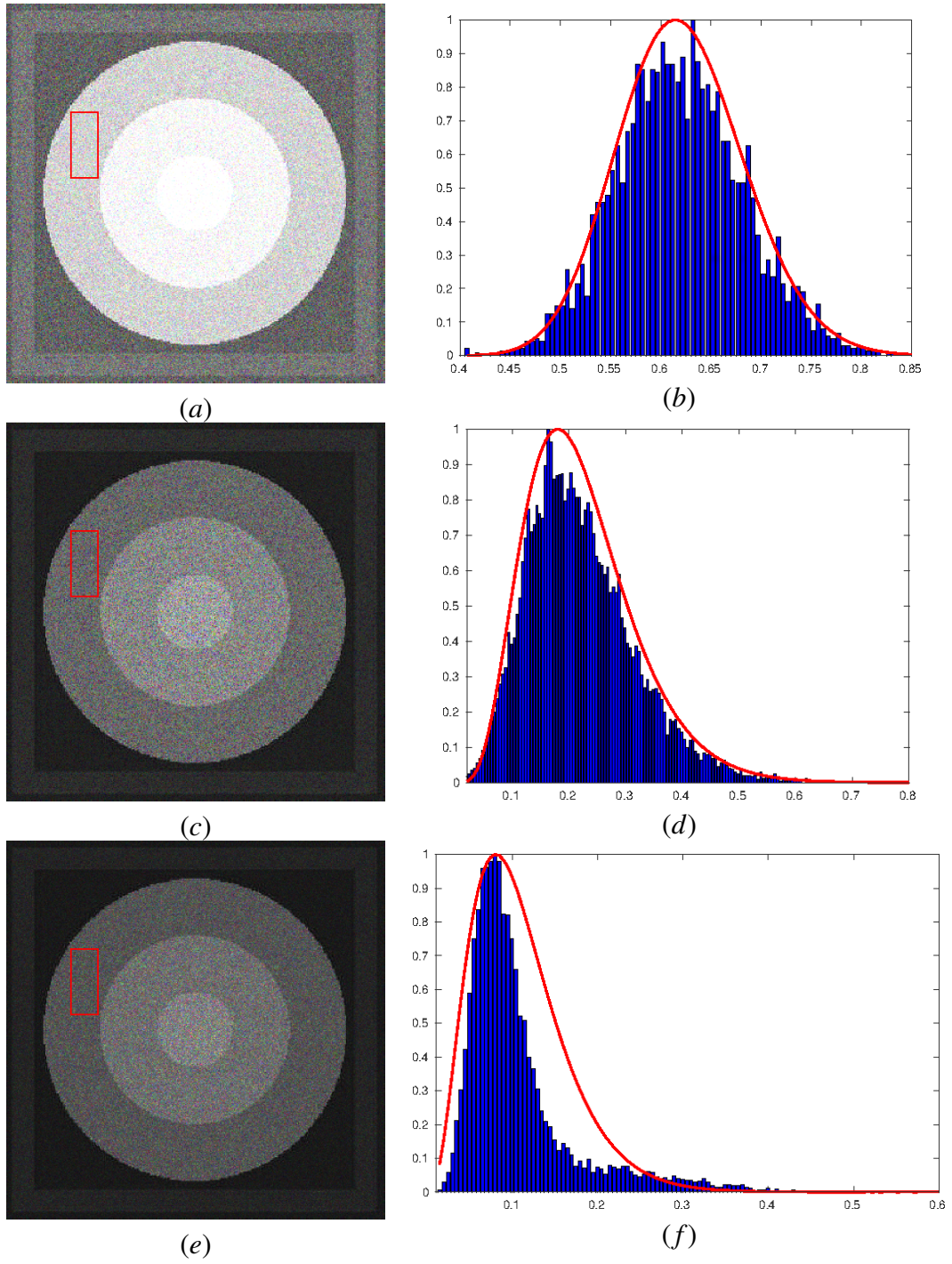


Figure 1.6 Histogram of a selected region plotted for images corrupted with (a) Gaussian (c) Rayleigh and (e) Gamma distributed noise.

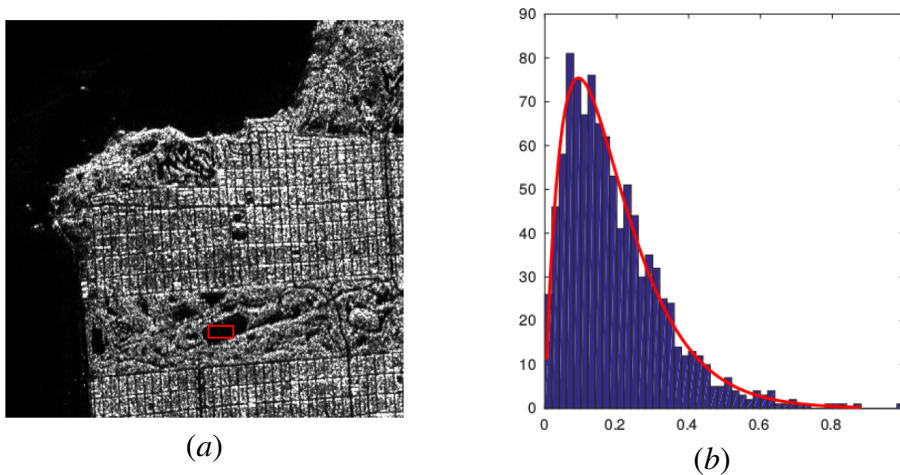


Figure 1.7 (a) Original San Francisco bay image (b) The PDF of the intensity distribution of the red colored region fitted with Gamma using the estimated parameters (Shape 2.0845 and Scale 0.0924).

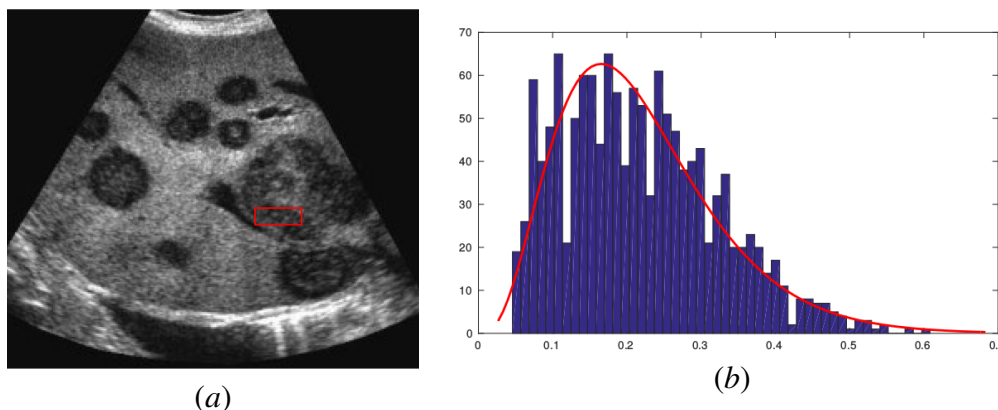


Figure 1.8 (a) Original Liver image (b) The PDF of the intensity distribution of the red colored region fitted with Gamma using the estimated parameters (Shape 1.9854 and Scale 0.0823).

1.9(a) shows original data which has a vertical axis (that represents the pixel intensity), that varies from 60 to 225, whereas Figure 1.9(b) shows the signal corrupted by an additive Gaussian noise of zero mean and standard deviation $\sigma = 20$, which has a vertical axis that runs from 10 to 280. Similarly, Figure 1.9(c) shows a Gamma noise corrupted signal with mean 1 and standard deviation 0.2 and the vertical axis runs from 40 to 320. The data-dependent nature of the Gamma noise (multiplicative) is pretty evident from the Figures 1.9 (b) and (c), as the noise variance is low at low intensity regions and high at high intensity regions, whereas, in Figure 1.9 (b) (which corresponds to a Gaussian distribution) the noise variation is almost the same in both low and high intensity regions (this gives a notion of data independence). A 2D representation of the above fact

has been demonstrated in Figure 1.10. The Figures 1.10 (b) and 1.10(c) show images corrupted by additive Gaussian white noise and blur, and multiplicative gamma noise and blur, respectively. From Figures 1.10(b) and (c) we can observe that noise variance in dark areas (low intensity points) are low compared to the bright ones. This signifies the fact that the noise depends largely on the underlying image features. However, in Figure 1.10(b) noise variance in low and high intensity regions are of almost the same, which in turn indicates that it is data independent. Removing the data-correlated multiplicative noise without distorting the significant image information is comparatively harder, which makes this study more meaningful in the context of denoising. Speckle (Gamma distributed) noise being common in many medical and satellite imaging applications the current study has a wider range of applications in the present context.

The focus of this thesis is oriented towards the restoration of images from data-correlated multiplicative noise, as it can cater to a wide range of imaging applications from the fields of medical and satellite imaging. In precise the field of US and SAR imaging demands a special attention due to the poor quality of acquired data used for analysis and diagnosis purpose.

1.4 Motivation

Image restoration under data-correlated noise has been a matter of interest for the last couple of decades. In the course of expansion of restoration methods their efficiency and accuracy also got improved. Speckles are the common kind of noise present in many medical and satellite imaging applications. Being data dependent, speckle noise forms a complex structure when gets intervened with the data. Speckle reduction has been a matter of interest among scientists and medical practitioners for decades altogether. As speckles form a skewed distribution, they are generally approximated using a Gamma or Rayleigh distribution. Further, it has been studied thoroughly about the formation of speckled and these studies have shown that the speckles are multiplicative in nature making the process more tedious unlike the additive noise models. Various ultrasound and synthetic aperture radar imaging systems are prone to these speckles when they form images using active sensing model. The waves used to probe the data get reflected and transmitted through the object on which they hit. The reflected waves finally form images. As the wave interference and diffraction results in out-of-phase waves when received at the sensor, the images are usually noisy or speckled. Speckles form high amplitude intensity variations in the resultant image. Since the characteristics of the noise varies with respect to the objects, the models devised for other noise distributions cannot be directly adopted for speckles. Therefore, the speckle noise dis-

tribution has to be thoroughly analyzed while designing the model. Though there are some models proposed for speckles specifically in the literature, many times they fail to restore the details when the speckle density is higher. Moreover, some of the models are theoretically unstable and does not provide a unique solution always. Whereas, some other models produce good results but converge slowly, yielding a lower convergence rate and subsequently decreasing the computational efficiency. All these facts motivate us to propose robust despeckling models which are computationally efficient and theoretically stable.

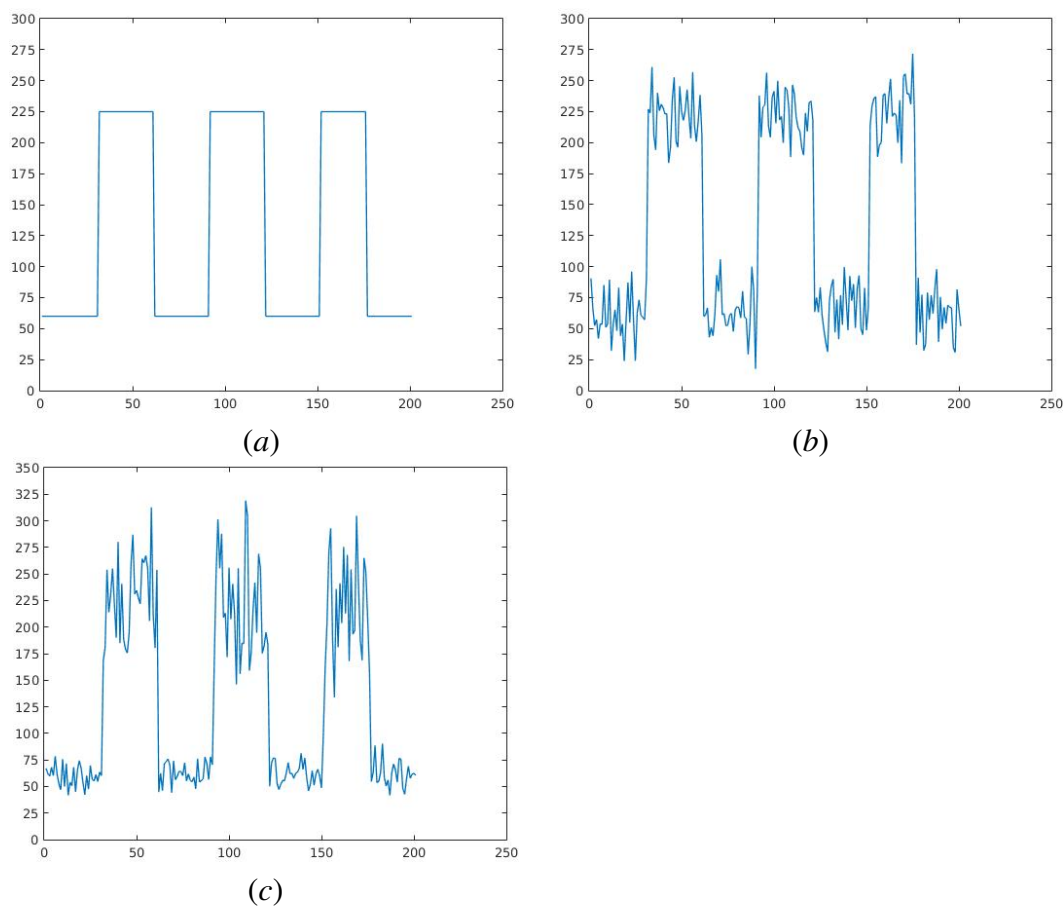


Figure 1.9 (a) Original 1-D Data (b) Degraded by additive Gaussian noise (c) Degraded by multiplicative Gamma noise.

1.5 Research Objectives

Since image restoration is an ill-posed inverse problem, it is hard to restore the actual data from a distorted observation. Though there has been a few approximations pro-

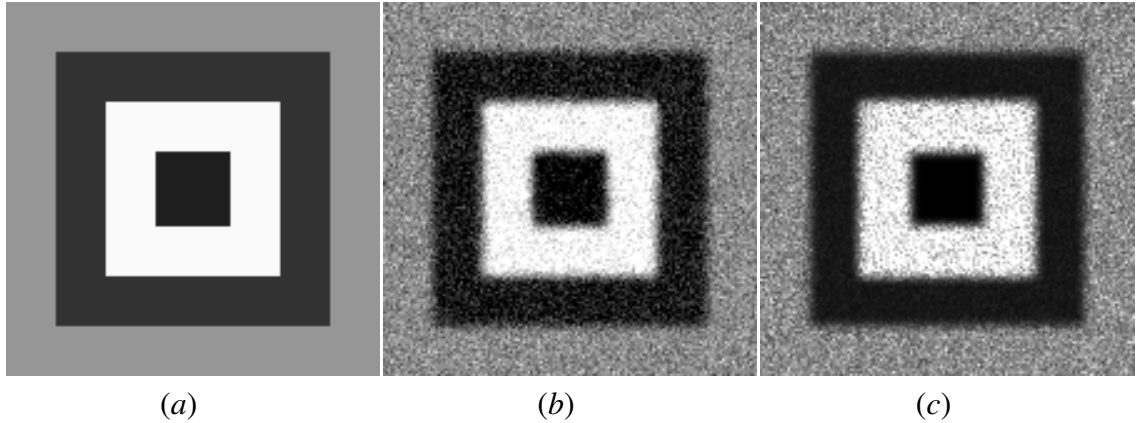


Figure 1.10 (a) Original synthetic image (b) Image corrupted by Gaussian noise and blur (c) Image corrupted by Gamma noise and blur.

posed over the last couple of decades, there is still scope for further improvements. The restoration is done with prior assumptions of the distortion model, such as distribution and nature of the noise and the behavior of the blurring artefacts. As the design of the model gets closely aligned with the actual degradation scenario, the restoration also consequently improves its performance. So the primary objective of the work is to mathematically model the degradation scenario to properly reflect the real-life situation. Once the degradation model is properly designed, the next step is to analyze the degradation scenario and comprehend the distortion aspects from a closer viewpoint. Since this work focuses on the distortions in the data due to data-correlated noise and linear blurring artefacts, the initial step is to analyze and study the nature of noise distributions and fine-tune the model to handle such distributions in an effective manner. Since the study focuses on the variational framework, the important task is to design an energy functional which properly captures the degradation scenario. The variational energy formulation can be done with a priori knowledge of the noise distribution and the blurring artefact. The functional should possess both regularization and data fidelity aspects in order to restore the data efficiently. The regularization term present in the model helps to regularize the fluctuations due to the noise distortions and ensures that minor perturbations in the data does not lead to major ones in the solution. Further, the data fidelity term ensures the minimal deviation from the actual solution as well as compliance of the model with reference to the assumed noise distribution. The overall objectives of the thesis work are summarized as follows:

1. Design of variational models to reflect the actual degradation scenario.
2. Devising the regularization and data-fidelity terms so as to restore the data effectively with due care and attention to the inherent image features (like edges, fine

details etc.) and reduce the damages to their natural appearance.

3. Analyze and study the model both theoretically and experimentally and compare with the state of the art restoration models. The analysis includes studying the condition for the existence of a unique solution.
4. The restoration model is to be designed to handle data-correlated speckles (which essentially follows a Gamma law) and linear blurring artefacts which are commonly observed in many medical and satellite imaging applications, which uses active sensing techniques.
5. To improve the models in terms of convergence by employing faster numerical approximations and ensuring the stability aspects of the model and making it less sensitive to the tunable parameters.
6. The parameters are to be adaptively tuned to ensure optimal solutions under various degradation conditions.

1.6 Organization and Contribution of the Thesis

The remaining chapters of the thesis are organized as follows: In the second chapter, the basic speckle suppression methods in the recent literature is reviewed. Speckle reduction methods are being extensively analyzed in this chapter. Various PDE and variational models are proposed in the literature to handle speckle noise distortions in the input data. The pros and cons of various algorithms proposed in the literature for speckle reduction are being analyzed and the research gaps are identified in this chapter. A further introduction to the motivation behind the proposed strategy is also highlighted therein.

Chapter 3: Despeckling of Ultrasound Images Using Non-Local Total Bounded Variation Regularization

In this Chapter, a non-local total bounded variation (NLTBV) regularization model is proposed for restoring the images corrupted with data-correlated speckles and linear blurring artefacts. The energy functional of the model is derived using a maximum a posteriori (MAP) estimate of the noise PDF. The non-local total bounded variation prior regularizes the model while the data fidelity is derived using the MAP estimator of the noise PDF. The computational efficiency of the model is improved using a fast numerical scheme based on the Augmented Lagrange formulation. The proposed model

is employed to restore US and SAR images, which are usually speckled and blurred. The numerical results are presented and compared. The efficiency of a NLTBV over the usual TV method is analyzed in this chapter. The condition for the existence of a unique minimizer for this model has been analyzed. The details are provided in the Appendix B.1. The additions of a parameter controlled L^2 penalty term in the Total bounded variation (TBV) model helps the model to denoise the data while preserving the meaningful information.

Chapter 4: Speckle Reducing Level-Set Approach

In this Chapter, a modified Mumford-Shah (MS) level-set model tuned to handle speckles and blur in SAR imagery is presented. The proposed model is formulated using a non-local regularization framework. Hence, the model duly cares about the local gradient oscillations (corresponding to the fine-details/textures), during the evolution process. It is assumed that the speckle intensity is Gamma distributed while designing the MAP Estimator of the functional. The parameters of the Gamma distribution (i.e., scale and shape) are estimated using the Maximum Likelihood (ML) Estimator. The regularization parameter of this model is evaluated adaptively using these (estimated) parameters at each iteration. The Split-Bregman (SB) iterative scheme is employed to improve the convergence rate of the model. The proposed and the state-of-the-art despeckling models are experimentally verified and compared using a large number of speckled and blurred SAR images. The statistical quantifiers are used to numerically evaluate the performance of various models under consideration. The model is further analyzed theoretically and condition for the existence of a unique minimizer for this model is analyzed in detail in Appendix C.1. The level-set formulation has been extensively used for image segmentation however, there are limited initiatives in the direction of its applicability in terms of denoising the data. This capability has been thoroughly analyzed in this chapter.

Chapter 5: Non-Local Gradient Fidelity Model for Multiplicative Gama Noise Removal

In this Chapter, a non-local gradient vector flow model is designed for restoring the images corrupted with Gamma distributed speckle noise and linear blur. The filter is found to preserve edges and finer details in the course of its evolution due to the presence of the non-local TV based diffusion term and the piecewise linear approximation is reduced considerably by the gradient fidelity term present in the model. The model

is found suitable for the restoration of various images from the field of satellite and clinical imaging. The experimental results are shown and compared for different image data sets both visually and qualitatively using various statistical measure.

Chapter 6: Conclusions and Future Research Directions

The last chapter concludes the entire research work presented and describes the avenues of possible future research works in this area. Since image restoration is an unavoidable pre-processing activity in most of the imaging applications, it finds a deserving place in the image processing literature. Further, the restoration being an ill-posed inverse problem, the restored data is always an approximation/estimation of the original one. The proximity of the estimated solution to the original one depends on how close the designed/simulated model is to the original one. Since all the models are designed under certain assumptions and conditions, there is still scope for further improvement in terms of the accuracy of the model and its computational efficiency. With the advent of various computationally efficient numerical techniques, the solution to such inverse problems has been improvised drastically.

Appendix

In this Appendix, theoretical results on the existence and uniqueness of the solutions and properties of the proposed models discussed in Chapter 3 and Chapter 4 are presented. Also, mathematical preliminaries are presented to improve readability of the thesis and ensure completeness in explanations. The detailed derivation of Bayesian MAP and ML estimators are also detailed in here. Sample codes used for implementing some of the models discussed in this thesis are also provided as a part of the Appendix.

Chapter 2

IMAGE DESPECKLING METHODS

The objective of this chapter is to provide an overview of the existing image restoration techniques for a speckled data. Several categories of methods have been proposed to remove speckle noise from images. Among them, the notable ones are statistical methods, PDE models, wavelet approaches, and variational methods.

2.1 Statistical Despeckling Methods

The methods which use the statistical properties of data to restore them had attracted the attention of the researchers. Though there were several modifications and updations done on these models to improve their efficiency and cater to various other noise features, the underlying principle remained more or less the same. Minimizing the error in the data was, in fact, the ultimate purpose of these models. A brief discussion of these models is provided in the next section and their role in motivating other restoration models (such as PDE models) has been highlighted in subsequent sections.

2.1.1 Minimum Mean Square Error Based Non-iterative Adaptive Filters

Adaptive filters are introduced in the literature for removing speckle noise and blur from SAR and ultrasound images. These filters usually adapt to the properties of an image locally and eliminate speckle noise from it. The local image statistics such as variance, mean and spatial correlation are being used by these filters to remove noise, while simultaneously preserving edges and features. Some examples of adaptive mean filters for speckle reductions include: Lee (Lee, 1980), Frost (Frost et al., 1982) and Kaun's filters (Kuan et al., 1985). By employing these filters, denoising shall be achieved up to a considerable extent, however, they eventually result in blurring of edges and poor

preservation of the details. A brief mathematical description of the standard spatial filters (filters defined in the spatial domain of the image) are given below:

Lee Filter

Based on the assumption of a linear speckle noise model, minimum mean square error (MMSE) approach was designed with a hope that it can reduce speckles while preserving the details in the image, which was later termed as the Lee filter. It removes speckle noise from images while retaining edges and details to an extent. The formulation of the Lee filter (Lee, 1980) is

$$\hat{\mathbf{u}}(i, j) = \bar{\mathbf{u}}_0(t) + \mathbf{W}(i, j)(\mathbf{u}_0(t) - \bar{\mathbf{u}}_0(t)), \quad (2.1)$$

where $\hat{\mathbf{u}}(i, j)$ is the output image intensity data (or the estimated output intensity), $\bar{\mathbf{u}}_0(t)$ is the average value of the intensity of the observed image (\mathbf{u}_0) within a filter window size $n \times n$, $\mathbf{W}(i, j)$ is the weighted function (the return value of $\mathbf{W}(\cdot)$ is 0 for flat regions and 1 is for the other regions) calculated as follows,

$$\mathbf{W}(i, j) = 1 - \frac{C_{\mathbf{u}}^2}{C_{\mathbf{u}_0}^2(t)}, \quad (2.2)$$

where $C_{\mathbf{u}_0}$ denotes the coefficient of variation of the image \mathbf{u}_0 and it is defined as

$$C_{\mathbf{u}_0} = \frac{\sigma_{\mathbf{u}_0}}{\bar{\mathbf{u}}_0}, \quad (2.3)$$

where $\sigma_{\mathbf{u}_0}$ is the standard deviation of the image \mathbf{u}_0 within the filter window. Similarly, $C_{\mathbf{u}}$ stands for the coefficient of variation of noisy image \mathbf{u} and it is determined by the expression:

$$C_{\mathbf{u}} = \frac{\sigma_{\mathbf{u}}}{\bar{\mathbf{u}}}. \quad (2.4)$$

Perhaps one can notice that the value of $\mathbf{W}(i, j)$ is zero in homogeneous areas, whereas it is unity near the edges. The main setback of the Lee-filter is that it tends to ignore the speckle noise near edges.

Frost Filter

Yet another improvement in this direction is, the introduction of Frost Filter, see Frost et al. (1982) for the details. The Frost filter replaces the pixel of interest with a weighted sum of the values within the $n \times n$ moving kernel. The weighing factors decrease with distance from the pixel of interest and increase for the central pixels, as their variance

within the kernel increases. This filter assumes a multiplicative noise and the noise statistics are assumed as stationary. The model amounts to the definition:

$$\hat{\mathbf{u}}(i, j) = \sum_p \sum_q \mathbf{m}(i+p, j+q) \mathbf{u}_0(i+p, j+q), \quad (2.5)$$

where p and q are the indices of the filter window and weighting function \mathbf{m} is defined as follows.

$$\mathbf{m}(i+p, j+q) = k_0 \exp(-K_1 C_{\mathbf{u}_0}^2(t) \sqrt{p^2 + q^2}), \quad (2.6)$$

where K_1 is a damping factor and k_0 is a normalizing constant and the other symbols are already defined earlier. The factor K_1 is chosen such that, in a homogeneous region $K_1 C_{\mathbf{u}_0}^2$ approaches 0 and the value of $\mathbf{m} = 1$, giving the mean filter output. In other regions (non-homogeneous ones) $K_1 C_{\mathbf{u}_0}^2$ tends to become large and the value of $\mathbf{m} = 0$ for the pixel surrounding (i, j) , and remain as 1 for the pixel (i, j) . Therefore, edges are preserved better compared to the Lee-filter. However, the assumption regarding the stationary properties of the noise statistics does not fit well in many practical scenarios.

Kuan Filter

Kuan Filter (Kuan et al., 1985) is derived from MMSE criteria under the assumption of a non-stationary mean and non-stationary variance (NMNV), unlike the Lee filter. Though, it is pretty similar to the Lee-filter in many aspects, it is regarded more efficient and robust as it does not require any approximation in the total derivation. The formulation of the filter follows:

$$\hat{\mathbf{u}}(i, j) = \bar{\mathbf{u}}_0(t) + \mathbf{W}(i, j)(\mathbf{u}_0(t) - \bar{\mathbf{u}}_0(t)). \quad (2.7)$$

The Kuan filter weighting function $\mathbf{W}(i, j)$ is defined as follows:

$$\mathbf{W}(i, j) = \frac{1 - C_{\mathbf{u}}^2 / C_{\mathbf{u}_0}^2(t)}{1 + C_{\mathbf{u}}^2}, \quad (2.8)$$

where both $C_{\mathbf{u}_0}$ and $C_{\mathbf{u}}$ follow the definition similar to the ones in the Lee filter. The difference between these two filters is, the term $1 + C_{\mathbf{u}}^2$. In the case of uniform regions $C_{\mathbf{u}} = C_{\mathbf{u}_0}$ which gives $\mathbf{W}(i, j) = 0$, yielding the result similar to a mean filter. In the area other than uniform regions like edges, details etc. $C_{\mathbf{u}_0} = \infty$ and the value of $\mathbf{W}(i, j) = 1$, this tends to eventually modify pixels near edges.

Although these filters perform well in removing speckle noise, they have the major limitations in preserving sharp features. This issue is duly addressed in non-linear PDE

models detailed in the subsequent sections.

2.2 PDE approaches

PDEs were used extensively for image denoising for decades. All these flagged-off their start, when the linear heat equation was adopted for image processing activities. Since images are the discrete array of pixels, they tend to act as energy points or more precisely as point sources of heat energy. A noisy image seems to have randomly distributed abrupt energy points which gives a noisy outlook to the corrupted image. Heat diffusion theory was introduced to image processing in Iijima (1962). However, it did not get much attention among the researchers due to the isotropic nature of the linear heat PDE. The PDE based image processing models geared up ever since a non-linear PDE was introduced for image restoration by Perona and Malik (1990). Thereafter, there were quite a few models proposed in the literature for image restoration. Some of the prominent proposals are highlighted in this section.

2.2.1 Anisotropic Diffusion Filter

Linear diffusion filters being isotropic, do not care much about the image details when they evolve in time. As a result, the images get smoothed along the time-frame, eventually resulting in blurred/coarse data. This causes difficulties in many computer vision algorithms, especially when the data needs to be analyzed for structures and objects present in it. The boundaries are smoothed along with the interior regions resulting in poor edge resolution. This was a major concern among the researchers till a non-linear PDE method was introduced by Perona and Malik (1990). This is a non-linear smoothing filter that diffuses based on the underlying image characteristics. The nonlinear PDE in Perona and Malik (1990) is defined as follows,

$$\begin{cases} \frac{\partial \mathbf{u}(x,y,t)}{\partial t} = \text{div}(g(|\nabla \mathbf{u}|) \nabla \mathbf{u}(x,y,t)), \\ \mathbf{u}(x,y,0) = \mathbf{u}_0(x,y), \end{cases} \quad (2.9)$$

where ∇ is the gradient operator, $|\cdot|$ denotes the magnitude, div is the divergence operator, $g(\cdot)$ is a non-increasing edge diffusivity function which allows isotropic diffusion in uniform regions and low diffusion near edges, the other symbols are defined already. Here the magnitude of diffusion is controlled by the function $g(\cdot)$, which is a function of the gradient magnitude. Two different alternatives are proposed for the coefficient

function $g(\cdot)$, by the authors:

$$g(\mathbf{y}) = e^{-(\mathbf{y}^2/k_2^2)}, \quad (2.10)$$

or

$$g(\mathbf{y}) = \frac{1}{1 + \mathbf{y}^2/k_2^2}, \quad (2.11)$$

where k_2 is a contrast parameter. In this model, the gradient magnitude is used to detect the edges and boundaries in the image, as sharp discontinuities. The advantage of Perona-Malik's anisotropic diffusion filter is that it has the ability to preserve edges while smoothing the rest of the image, but it tends to generate multiple false edges and the denoising does not happen along the edges. This method is more suitable for removing additive Gaussian white noise but fails to restore effectively when the noise is correlated with the data.

2.2.2 Speckle Reducing Anisotropic Diffusion Filter

Yu and Acton (2002) introduced a new filter based on the non-linear diffusion method in Perona and Malik (1990), which was named Speckle Reducing Anisotropic Diffusion (SRAD). This method uses both the Laplacian and gradient magnitudes for detecting discontinuities, unlike just the gradient magnitudes in Perona and Malik (1990). SRAD is a despeckling version of the non-linear PDE (Perona and Malik, 1990), whose coefficient of variation controls the diffusion magnitude without much destructing the significant details present in images. This filter performs better than the anisotropic model (Perona and Malik, 1990) in case of speckled images, as the coefficient of variation is designed to handle the speckles in images. Given an initial image $\mathbf{u}_0(i, j)$ having finite power and non-zero values over the image support Ω , the resulting image $\mathbf{u}(x, y; t)$ is obtained as a solution of the following PDE:

$$\begin{cases} \partial \mathbf{u}(i, j; t) / \partial t = \text{div}[c(\mathbf{g}) \nabla \mathbf{u}(i, j; t)], \\ \mathbf{u}(i, j; 0) = \mathbf{u}_0(i, j), \\ (\partial \mathbf{u}(i, j; t) / \partial \vec{n})|_{\partial \Omega} = 0, \end{cases} \quad (2.12)$$

where $\partial \Omega$ denotes the borders of Ω , \vec{n} is the outer normal to the $\partial \Omega$, t represents diffusion time and

$$c(\mathbf{g}) = \frac{1}{1 + \frac{[\mathbf{g}^2(i, j; t) - \mathbf{g}_0^2(t)]}{[\mathbf{g}_0^2(t)(1 + \mathbf{g}_0^2(t))]}}, \quad (2.13)$$

or

$$c(\mathbf{g}) = \exp - [\mathbf{g}^2(i, j; t) - \mathbf{g}_0^2(t)] / [\mathbf{g}_0^2(t)(1 + \mathbf{g}_0^2(t))], \quad (2.14)$$

where $\mathbf{g}(i, j, t)$ is the instantaneous coefficient of variation and is given by:

$$\mathbf{g}(i, j, t) = \sqrt{\frac{(1/2)(|\nabla \mathbf{u}/\mathbf{u}|)^2 - (1/4)^2(\nabla^2 \mathbf{u}/\mathbf{u})^2}{[1 + (1/4)(\nabla^2 \mathbf{u}/\mathbf{u})]^2}}. \quad (2.15)$$

If the image is degraded by speckles, then the above mentioned function $\mathbf{g}(\cdot)$ helps to detect the edges of the image. At high contrast regions and edges, this function returns high values. In uniform regions it gives low values, $\mathbf{g}_0(t)$ here denotes the speckle scale function and $\mathbf{g}(i, j, t)$ fluctuates around $\mathbf{g}_0(t)$. The function $\mathbf{g}_0(t)$ is used to effectively control the smoothing of the image during the filtering process. The function $\mathbf{g}_0(t)$ can be approximated by (Yu and Acton, 2002).

$$\mathbf{g}_0(t) \approx \mathbf{g}_0 \exp(-\rho t), \quad (2.16)$$

therefore, it is expected that in homogeneous regions the diffusion should be isotropic. Adopting a discrete isotropic diffusion gives:

$$\mathbf{u}_{i,j}^{t+\Delta t} = \mathbf{u}_{i,j}^t + \frac{\Delta t}{4}(\mathbf{u}_{i+1,j}^t + \mathbf{u}_{i-1,j}^t + \mathbf{u}_{i,j+1}^t + \mathbf{u}_{i,j-1}^t - 4\mathbf{u}_{i,j}^t), \quad (2.17)$$

where ρ is a constant, which retards the decrease of $\mathbf{g}_0(\cdot)$ during the iteration and Δt denotes the time step.

The SRAD algorithm provides better performance compared to many despeckling algorithms, in terms of smoothing flat regions and at the same time preserves edges and features. However, in an anisotropic diffusion filter, the diffusion function depends on the accuracy of recognizing the edges, which in turn depends on the threshold selected for this purpose. So the performance of SRAD is sensitive to the selection of the threshold value. Even though SRAD has a dynamic threshold value, its accuracy of edge recognition is not that commendable, especially when the edges are weak. Therefore, though SRAD is a well-known method for removing speckles from images, still it seems to perform slightly on the lower side in preserving weak edges and the details.

2.2.3 Details Preserving Anisotropic Diffusion

To overcome the problems of SRAD method, Aja-Fernandez and Alberola-Lopez proposed a new method by modifying the SRAD using the Kuan filter (Kuan et al., 1985). They use a larger neighborhood to estimate the diffusion coefficients, it is named as detail-preserving anisotropic diffusion (DPAD) (Aja-Fernández and Alberola-López,

2006). DPAD computes the coefficient of variation as follows:

$$c(\mathbf{g}) = \frac{1 + \frac{1}{\mathbf{g}(i,j;t)^2}}{1 + \mathbf{g}_0^2(t)}, \quad (2.18)$$

and the DPAD diffusion coefficient function is given as:

$$\mathbf{g}(i, j; t) = \sqrt{\frac{\frac{1}{|\eta_{i,j}|-1} \sum_{p \in \eta_{i,j}} (\mathbf{u}_p - \bar{\mathbf{u}}_{i,j})^2}{(\bar{\mathbf{u}}_{i,j})^2}}, \quad (2.19)$$

where $|\eta_{i,j}|$ is a square $z \times z$ neighborhood of the pixel at location (i, j) , p is any pixel in the window, \mathbf{u}_p is the intensity of the pixel p , $\bar{\mathbf{u}}_{i,j}$ is the mean intensity value of the pixels in the window and the value of scaling factor $\mathbf{g}_0(t)$ is:

$$\mathbf{g}_0^2(t) = \text{Median}_{i,j}(\mathbf{g}^2(i, j; t)). \quad (2.20)$$

The median based estimation of the scaling factor helps to keep edge details better compared to the mean based estimation techniques. Though it works well for speckles in the homogeneous regions the performance of these non-linear diffusion models is not that appreciable along the edge features. Moreover, like the Perona and Malik (1990) model this model also fails to handle the noise features along the edges. This issue is addressed considerably well by the Oriented Speckle Reducing Anisotropic Diffusion filter whose details follow.

2.2.4 Oriented Speckle Reducing Anisotropic Diffusion (OSRAD) Filter

Krissian et al. (2007) have added a non-scalar component to the SRAD filter which performs directional filtering of images along the structures, which eventually filter-out the noise components along the edges as well. The OSRAD is defined as:

$$\begin{aligned} \frac{\partial \mathbf{u}}{\partial t} &= \text{div}((1 - k_3) \nabla \mathbf{u}), \\ &= \text{div} \left(\begin{bmatrix} (1 - k_3) & 0 & 0 \\ 0 & (1 - k_3) & 0 \\ 0 & 0 & (1 - k_3) \end{bmatrix} \nabla \mathbf{u}, \end{aligned} \quad (2.21)$$

where k_3 is a function of the diffusion time t . The diffusion matrix $\mathbf{D} = (1 - k_3)\mathbf{I}$, where \mathbf{I} denotes the identity matrix. The direction of gradient and the principal cur-

vatures of the image are used for guiding the diffusion process. Local orientation is used for preserving the structures having minimum intensities. Enhanced images can be obtained by combining enhancement in gradient direction and smoothing techniques applied in the curvature direction. Therefore diffusion matrix can be redefined, in the basis (v_0, v_1, v_2) , as

$$\mathbf{D} = \begin{bmatrix} (1 - k_3) & 0 & 0 \\ 0 & c_{max} & 0 \\ 0 & 0 & c_{min} \end{bmatrix}, \quad (2.22)$$

where c_{max} denotes the smoothing along the direction of maximal curvature and c_{min} along the direction of minimal curvature. The results obtained after processing the input image using various methods discussed above in this section are shown in Figure 2.1.

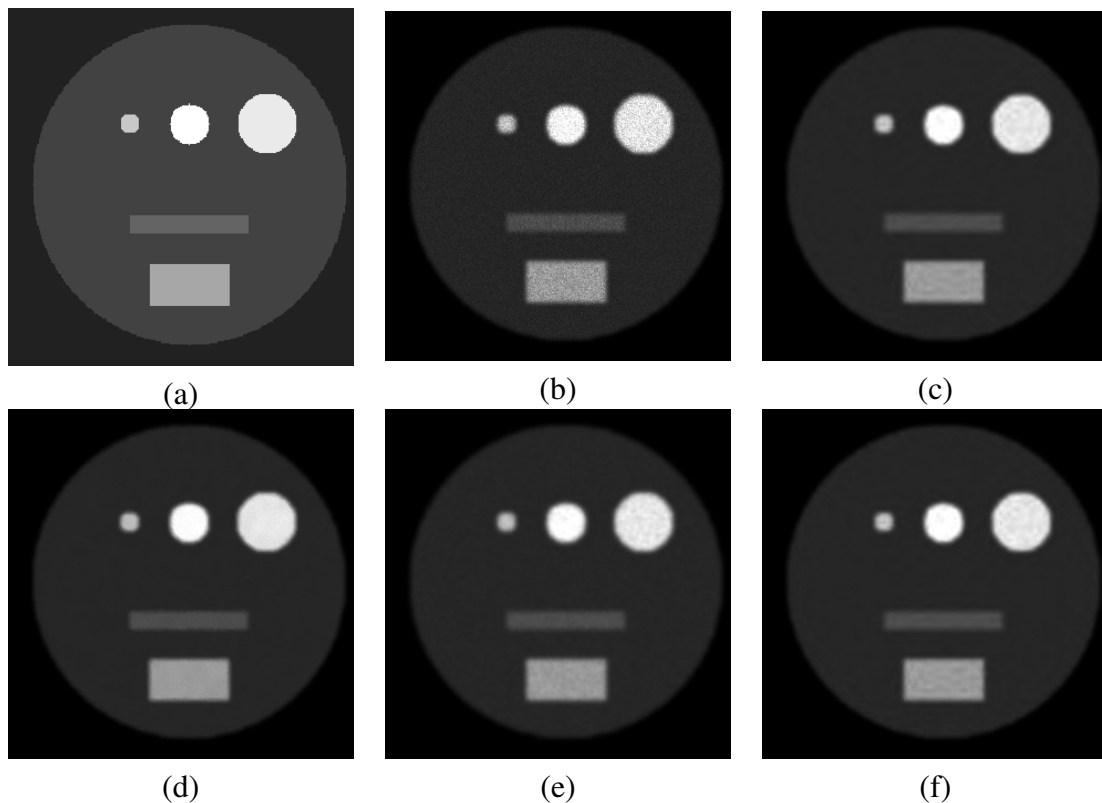


Figure 2.1 (a) Reference image (b) Noisy image with mean 1, noise variance 0.1 and Gaussian blur with kernel spread 4 (c) Restored using Anisotropic Diffusion method (d) Restored using SRAD method (e) Restored using DPAD method (f) Restored using OSRAD method

Many of these second order diffusion models tend to smooth-out the gradient oscillations along with the speckles and results in homogeneous intensity images; causing severe damages to the textures and details. As commonly observed, some of these

second order non-linear diffusion models perform linear approximations for non-linear functions; resulting in piecewise-linear stair formation, eventually making the output visually less appealing. Moreover, the noise distribution is not directly accounted for the design of the model making it vulnerable to the noise variance. Though, these speckle reducing filters (discussed above) are the improved versions of the Perona and Malik (1990) model, still they carry some of the basic limitations of this model especially when removing the noise along the edges. The convergence of these models depends on the chosen time-step. For an appropriately chosen time step these models converge under a gradient-descent scheme, however it takes a large number of iterations if the chosen time step is too small and shoot-out from the optimal solution under a large time-step. Therefore, selection of an appropriate time-step is crucial for their improved performance. Restoration in scale-space domain has been actively analyzed in the literature. Wavelet based approaches are the ones which have attracted the attention of the researchers in the recent literature. A brief discussion about the wavelet despeckling models are done in the next section.

2.3 Wavelet Transforms for Speckle Reduction

Another category of filters introduced during the recent past based on wavelet transformation are found in Ranjani and Thiruvengadam (2010); Amirmazlaghani and Amin-davar (2012); Argenti et al. (2012), since wavelet-transforms are universally recognized as powerful tools for analyzing non-stationary signals and images, as they capture the attention of the researchers to a considerable extent. Although these methods perform better than the known classical filters (Lee, 1980; Frost et al., 1982; Kuan et al., 1985; Yu and Acton, 2002), the noise distribution is least bothered while denoising the data, moreover they eventually form ringlike artefacts similar to the ones formed by classical low-pass/bandpass filters, leading to the so called Gibbs phenomena when hard-thresholds are used. This undesired phenomenon can be reduced by using soft-thresholding schemes instead of hard ones, but at the cost of high computational expense (Donoho, 1995; Donoho and Johnstone, 1995b; Chang et al., 2000). A major issue in the wavelet despeckling methods is the computation of appropriate threshold. There are several choices, which can be adopted for this purpose: Universal threshold (Donoho, 1995), Stein's unbiased risk estimate (SURE) threshold (Donoho and Johnstone, 1995b), and Bayes shrink threshold (Chang et al., 2000) are some classical options available in the literature. Yet another recent development in thresholding schemes is the analytical wavelet shrinkage model (proposed for SAR imagery) based on maximum a posteriori criteria, introduced in Li et al. (2013). In this model the es-

estimates for noise-free wavelet coefficients are found by heterogeneity-adaptive thresholding scheme. Another shrinkage operator is being dealt-with in (Gao et al., 2016), where the authors use a S-Transform shrinkage in place of wavelet-shrinkage. It provides frequency-dependent resolution while maintaining a direct relationship with the Fourier spectrum. It has been also pointed out that the S-Transform can be applied to noisy signals or the ones with complicated time-frequency structure. Nevertheless, these filters largely rely on the detection of an appropriate threshold to perform the shrinkage operation. Detection of an appropriate threshold is challenging in cases where the noise is correlated with the signal. Moreover, the noise distribution is neglected in many of these models therefore, their performance is limited in case of data-correlated noise observations, through they perform well for data-independent noise distributions such as additive-Gaussian. The variational models are capable of handling various data-correlated noise distortions in an effective way. They tend to optimize a given energy functional to obtain the desired solution. The functional thus designed is capable of incorporating the noise related a priori information into the model, making it more robust and stable in denoising various noise distributions. The details follow.

2.4 Variational Model for Image Restoration Under an Additive Noise

In general, the image restoration using variational algorithms follow the minimization problem (Rudin et al., 1992) given below.

$$\min_{\mathbf{u}} \left\{ E(\mathbf{u}) = \int_{\Omega} \phi(|\nabla \mathbf{u}|) \, dx \, dy + \lambda \int_{\Omega} H(\mathbf{u}) \, dx \, dy \right\}. \quad (2.23)$$

Here $H(\mathbf{u})$ denotes data-fitting term which ensures a less deviation to the restored image from the original image. The term $\nabla \mathbf{u}$ denotes the gradient of the image \mathbf{u} and λ is a regularization parameter. Variational models have been extremely successful in a wide variety of image restoration problems such as image denoising, deblurring and inpainting. Variational model is one of the most active areas of research in image processing and computer vision. Some of the well studied variational formulations for image restoration are discussed in this section.

2.4.1 Total Variation Regularization

Several variational models have been proposed for Additive Gaussian White Noise (AGWN) (Rudin et al., 1992; You and Kaveh, 2000; Lysaker et al., 2003). Among

them, the Total Variation (TV) regularization or Rudin Osher Fatemi (ROF) model (Rudin et al., 1992) is quite explored. The constrained minimization problem of TV regularization is to minimize the objective function:

$$\text{minimize } \int_{\Omega} |\nabla \mathbf{u}| \, dx \, dy, \quad (2.24)$$

subject to the constraint

$$\int_{\Omega} \mathbf{K} \mathbf{u} \, dx \, dy = \int_{\Omega} \mathbf{u}_0 \, dx \, dy. \quad (2.25)$$

Assuming a zero mean Gaussian noise \mathbf{n} with variance σ^2 , the above expression stands modified as:

$$\int_{\Omega} \frac{1}{2} (\mathbf{K} \mathbf{u} - \mathbf{u}_0)^2 \, dx \, dy = \sigma^2. \quad (2.26)$$

Here $|\nabla \mathbf{u}| = \sqrt{(\mathbf{u}_x^2 + \mathbf{u}_y^2)}$, where \mathbf{u}_x and \mathbf{u}_y are the partial derivatives of \mathbf{u} with respect to x and y , respectively. The above constrained optimization problem can be transformed to an unconstrained minimization problem using the Lagrange formulation as follows:

$$\min_{\mathbf{u}} \left\{ E(\mathbf{u}, \lambda) = \int_{\Omega} |\nabla \mathbf{u}| \, dx \, dy + \frac{\lambda}{2} \|\mathbf{K} \mathbf{u} - \mathbf{u}_0\|_{L^2}^2 \, dx \, dy \right\}, \quad (2.27)$$

here \mathbf{K} is a real blurring kernel given in equation(1.4) (Chan and Wong, 1998), Ω denotes the image domain, which is usually a rectangle region and here $\|\cdot\|_{L^2}$ denotes the usual L^2 norm of the functional. In the above equation first term on the right hand side denotes the TV regularization term, that is used to smooth the image \mathbf{u} , the second term denotes the data fidelity, which ensures a minimal deviation from the observed data \mathbf{u}_0 and $\lambda > 0$ is the Lagrange multiplier. The above mentioned unconstrained minimization problem can be solved as a convex optimization, as the objective function is convex (not in the strict sense). To solve this problem the general approach is to define a Euler-Lagrange derivative for the above functional $E(x, y, \mathbf{u}, \mathbf{u}', \lambda)$, where x and y are independent variables, \mathbf{u} and \mathbf{u}' are the image function and its first derivative, respectively. The solution is sought for a function \mathbf{u} which minimizes this functional. The Euler-Lagrange (E-L) derivative of a function $F(x, \mathbf{u}, \mathbf{u}')$ is $\frac{dF}{d\mathbf{u}} - \frac{d}{dx} \left(\frac{\partial \mathbf{u}}{\partial \mathbf{u}'} \right) = 0$. Applying E-L derivative on the above minimization problem and defining an iterative gradient descent solution gives:

$$\frac{\partial \mathbf{u}}{\partial t} = \nabla \cdot \left(\frac{\nabla \mathbf{u}}{|\nabla \mathbf{u}|} \right) - \lambda (\mathbf{K}^* (\mathbf{K} \mathbf{u} - \mathbf{u}_0)) \quad \text{in } \Omega. \quad (2.28)$$

where \mathbf{K}^* is the adjoint of the operator \mathbf{K} . The initial and boundary conditions are as follows:

$$\text{initial condition : } \mathbf{u}(x, y, 0) = \mathbf{u}_0 \quad \text{in } \Omega, \quad (2.29)$$

$$\text{boundary condition : } \frac{\partial \mathbf{u}}{\partial \vec{n}} = 0, \quad \text{on } \partial\Omega, \quad (2.30)$$

where \vec{n} is normal to the boundary. Unless defined otherwise, all the partial differential equations in this thesis consider the above mentioned initial and boundary conditions. Note that when $\mathbf{K} = \mathbf{I}$ in the equation (2.27), we obtain an image denoising problem.

As already pointed out, the method works well for a data-independent Gaussian noise, however, it fails to restore data efficiently in case of data-correlated noise distributions. Moreover, like the second order PDE models this model also performs a piecewise linear approximations to the input data, leading to the so called ‘‘staircase effect’’. Furthermore, the gradient descent approaches converge slowly and their convergence rate depends on the regularization parameter and the time-step. For an appropriately chosen time-step, the gradient descend formulations yields a unique solution for this convex optimization problem. There are many fast numerical solvers proposed in the literature such as Chambolle projection method (Chambolle, 2004), SB iteration method Goldstein and Osher (2009) and Augmented Lagrangian method Chan et al. (2011) to overcome these problems.

2.4.2 Higher order PDEs for Image Restoration

Although the anisotropic diffusion model is an effective way for denoising images, it is observed that it produces the staircase effect in the course of its evolution, as mentioned earlier. In order to overcome the staircase effect and improve the restorability of second order PDEs, fourth order PDE filtering techniques have been proposed, see (You and Kaveh, 2000) for the details. The functional of this model is stated below.

$$E(\mathbf{u}) = \int_{\Omega} g(|\nabla^2 \mathbf{u}|) \, dx \, dy, \quad (2.31)$$

where ∇^2 denotes Laplacian operator of the image \mathbf{u} and the function $g(\cdot) \geq 0$ is an increasing function. The corresponding Euler-Lagrange equation is

$$\nabla^2 [g'(|\nabla^2 \mathbf{u}|) \text{sign}(\nabla^2 \mathbf{u})] = 0, \quad (2.32)$$

which is also written in the following form,

$$\nabla^2 \left[g'(|\nabla^2 \mathbf{u}|) \frac{\nabla^2 \mathbf{u}}{|\nabla^2 \mathbf{u}|} \right] = 0. \quad (2.33)$$

The Euler equation stated above is solved following the gradient descent procedure as:

$$\frac{\partial \mathbf{u}}{\partial t} = -\nabla^2 \left[g'(|\nabla^2 \mathbf{u}|) \frac{\nabla^2 \mathbf{u}}{|\nabla^2 \mathbf{u}|} \right] = -\nabla^2 [c(|\nabla^2 \mathbf{u}|) \nabla^2 \mathbf{u}]. \quad (2.34)$$

This fourth order PDE employs a piecewise planar approximation in place of piecewise linear one, eventually leading to a natural outlook to the filtered data. On the other hand, it reduces the staircase effect but tends to leaves isolated black and white speckles in the resulting image.

The numerical instability which leads to the speckle-like formation in the above model has been addressed in yet another fourth order PDE model introduced in (Lysaker et al., 2003). In this model, the authors put forth an idea to minimize the total variation norm of the functional ∇u . The corresponding energy minimization functional takes the following form:

$$E(\mathbf{u}) = \arg \min_{\mathbf{u}} \left\{ \int_{\Omega} |\nabla^2 \mathbf{u}| \, dx \, dy + \frac{\lambda}{2} \int_{\Omega} \|\mathbf{u} - \mathbf{u}_0\|_{L^2}^2 \, dx \, dy \right\}. \quad (2.35)$$

Here the regularization functional is the magnitude of the Laplacian, therefore the model adopts a planar approximation as already pointed out in the aforementioned fourth order PDE model. Moreover, the authors suggest two different definitions for the magnitude of the Laplacian, which in turn measures the degree of oscillations in the input data, they are

$$|\nabla^2 \mathbf{u}| = \begin{cases} |\Sigma \mathbf{u}| = \int_{\Omega} (|\mathbf{u}_{xx}| + |\mathbf{u}_{yy}|) \, dx \, dy & \text{or} \\ |\theta \mathbf{u}| = \int_{\Omega} (\mathbf{u}_{xx}^2 + \mathbf{u}_{xy}^2 + \mathbf{u}_{yx}^2 + \mathbf{u}_{yy}^2)^{\frac{1}{2}} \, dx \, dy. \end{cases} \quad (2.36)$$

Adopting the first definition for the magnitude Laplacian (i.e. $|\nabla^2 \mathbf{u}| = |\Sigma \mathbf{u}|$), the E-L formulation takes the form:

$$\left(\frac{\mathbf{u}_{xx}}{|\mathbf{u}_{xx}|} \right)_{xx} + \left(\frac{\mathbf{u}_{yy}}{|\mathbf{u}_{yy}|} \right)_{yy} + \lambda (\mathbf{u} - \mathbf{u}_0) = 0, \quad (2.37)$$

the gradient descent approximation of the above model amounts to:

$$\frac{\partial \mathbf{u}}{\partial t} = - \left(\frac{\mathbf{u}_{xx}}{|\mathbf{u}_{xx}|} \right)_{xx} - \left(\frac{\mathbf{u}_{yy}}{|\mathbf{u}_{yy}|} \right)_{yy} - \lambda (\mathbf{u} - \mathbf{u}_0). \quad (2.38)$$

The value of the regularization parameter λ can be determined from the steady-state solution of the above PDE, i.e

$$\lambda = -\frac{1}{\sigma^2} \int_{\Omega} \left(\frac{\mathbf{u}_{xx}}{|\mathbf{u}_{xx}|} (\mathbf{u} - \mathbf{u}_0)_{xx} + \frac{\mathbf{u}_{yy}}{|\mathbf{u}_{yy}|} (\mathbf{u} - \mathbf{u}_0)_{yy} \right) dx dy. \quad (2.39)$$

Alternatively, if the second definition is adopted for the magnitude Laplacian (i.e. $|\nabla^2 \mathbf{u}| = |\theta \mathbf{u}|$), the E-L derivation results in:

$$\left(\frac{\mathbf{u}_{xx}}{|\Delta \mathbf{u}|} \right)_{xx} + \left(\frac{\mathbf{u}_{xy}}{|\Delta \mathbf{u}|} \right)_{yx} + \left(\frac{\mathbf{u}_{yx}}{|\Delta \mathbf{u}|} \right)_{xy} + \left(\frac{\mathbf{u}_{yy}}{|\Delta \mathbf{u}|} \right)_{yy} + \lambda (\mathbf{u} - \mathbf{u}_0) = 0. \quad (2.40)$$

Further the gradient descent method is defined as:

$$\frac{\partial \mathbf{u}}{\partial t} = - \left(\frac{\mathbf{u}_{xx}}{|\Delta \mathbf{u}|} \right)_{xx} - \left(\frac{\mathbf{u}_{xy}}{|\Delta \mathbf{u}|} \right)_{yx} - \left(\frac{\mathbf{u}_{yx}}{|\Delta \mathbf{u}|} \right)_{xy} - \left(\frac{\mathbf{u}_{yy}}{|\Delta \mathbf{u}|} \right)_{yy} - \lambda (\mathbf{u} - \mathbf{u}_0). \quad (2.41)$$

Here

$$|\Delta \mathbf{u}| = (|\mathbf{u}_{xx}|^2 + |\mathbf{u}_{xy}|^2 + |\mathbf{u}_{yx}|^2 + |\mathbf{u}_{yy}|^2)^{\frac{1}{2}}.$$

In order to avoid the singularities in the above mentioned solutions, $|\Delta \mathbf{u}|$ is generally replaced with $|\Delta \mathbf{u}|_{\varepsilon} = \sqrt{|\Delta \mathbf{u}|^2 + \varepsilon}$, where ε is a small positive constant. This model provides a better restoration compared to the previous fourth order PDE model. Nevertheless, these higher order models are designed under the assumption of a data uncorrelated random noise. Moreover, unlike the second order models, the fourth order models lead to the over-smoothing of the data due to the presence of a Laplacian in place of the gradient operator for the detection of intensity variations. Furthermore, the higher order filters converge to a solution at a lower rate even if the time-step is chosen appropriately. Attempts have been made to fine-tune the Laplacian based fourth order model to cater to data-correlated noise distributions such as speckles (Chen et al., 2012; Liu et al., 2013; Bini and Bhat, 2013). However, they are not devoid of the setbacks of the fourth order PDEs discussed so far. The results obtained after processing the input image using various methods discussed in the section above are shown in Figure 2.2.

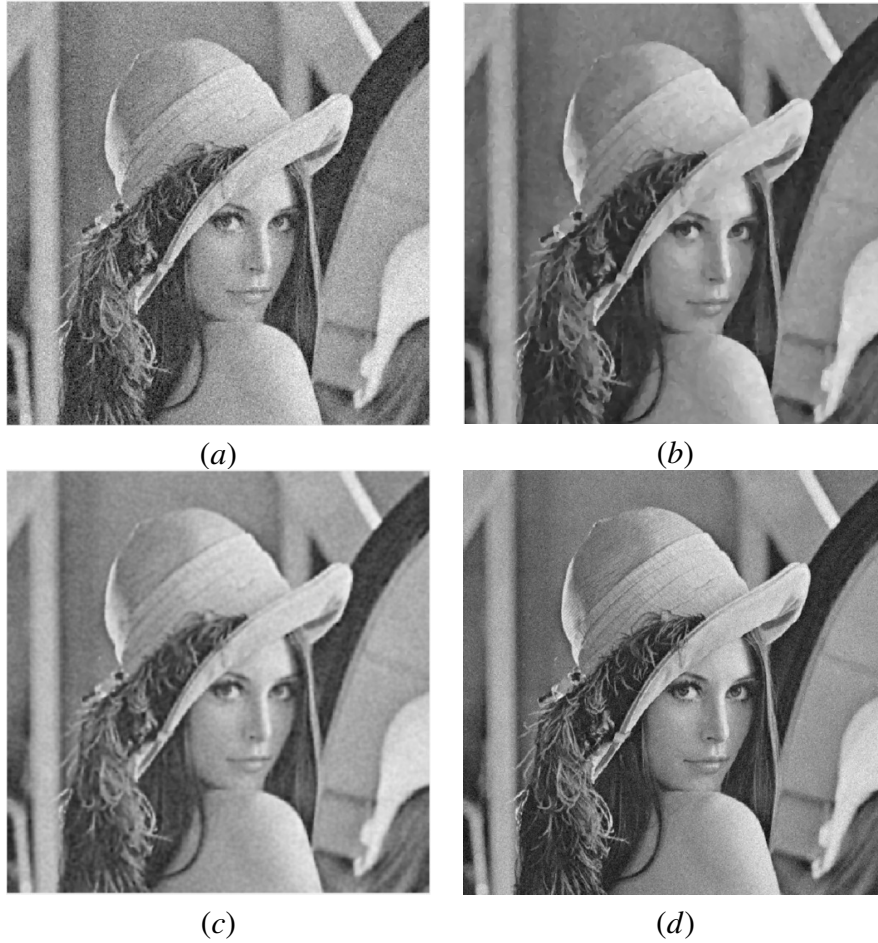


Figure 2.2 (a) Original Lena image corrupted by Gaussian noise with mean 0 and variance 0.15 (b) Restored using ROF (TV) method (c) Restored using (You and Kaveh, 2000) method (d) Restored using (Lysaker et al., 2003) method.

2.5 Variational Models for Image Restoration Under Multiplicative Noise

Since speckle formation is not an independent random process, the speckles are generally regarded as data-correlated noise. Moreover, the speckles are multiplicative in nature i.e., $\mathbf{u}_0 = \mathbf{K}\mathbf{u}$, (where $\mathbf{u} \in \mathbb{R}^N$ and $\mathbf{u}_0 \in \mathbb{R}^N$ (Note : $N = m \times n$ size of the image) are the original and noisy images, respectively) in the sense it gets multiplied with the intensity values making the data depend on it. This data-correlated nature of a speckle makes its removal tedious. In this section, we discuss about some of the well-known regularization frameworks proposed for image restoration beginning with the Total Variation regularization proposed for a multiplicative Gaussian noise. This model is motivated by the Total Variation model proposed by Rudin et al. (1992).

2.5.1 Total Variation Model for Multiplicative Noise

Rudin et al. (2003) proposed a variational framework for multiplicative Gaussian noise. This was the first of this kind, being proposed for a data-correlated noise environment. The optimization functional takes the form:

$$\text{minimize } \int_{\Omega} |\nabla \mathbf{u}| \, dx \, dy, \quad (2.42)$$

subject to the constraint

$$\int_{\Omega} \frac{\mathbf{u}_0}{\mathbf{K}\mathbf{u}} = 1, \quad (2.43)$$

which yields

$$\int_{\Omega} \frac{1}{2} \left(\frac{\mathbf{u}_0}{\mathbf{K}\mathbf{u}} - 1 \right)^2 = \frac{\sigma^2}{2} = \int_{\Omega} \frac{1}{2} \left(\left(\frac{\mathbf{u}_0}{\mathbf{K}\mathbf{u}} \right)^2 - 1 \right). \quad (2.44)$$

Note: $\int_{\Omega} \mathbf{n} = 1$ and $\int_{\Omega} (\mathbf{n} - 1)^2 = \sigma^2$ are the mean and the variance of the noise distribution, respectively. An unconstrained formulation of the above problem is:

$$\min_{\mathbf{u}} \left\{ E(\mathbf{u}) = \int_{\Omega} \left(|\nabla \mathbf{u}| + \frac{\lambda}{2} \left(\frac{\mathbf{u}_0^2}{(\mathbf{K}\mathbf{u})^2} - 1 \right) + \mu \frac{\mathbf{u}_0}{\mathbf{K}\mathbf{u}} \right) \, dx \, dy \right\}. \quad (2.45)$$

The gradient descent solution for equation(2.45) is as follows:

$$\mathbf{u}_t = \text{div} \left(\frac{\nabla \mathbf{u}}{|\nabla \mathbf{u}|} \right) - \lambda \mathbf{K}^* \left(\frac{\mathbf{u}_0}{(\mathbf{K}\mathbf{u})^2} \right) \left(\frac{\mathbf{u}_0}{\mathbf{K}\mathbf{u}} - 1 \right) - \mu \mathbf{K}^* \left(\frac{\mathbf{u}_0}{(\mathbf{K}\mathbf{u})^2} \right). \quad (2.46)$$

It may be noted that, if \mathbf{K} is identity operator, then the gradient descent solution for equation(2.45) is given by:

$$\mathbf{u}_t = \text{div} \left(\frac{\nabla \mathbf{u}}{|\nabla \mathbf{u}|} \right) - \lambda \frac{\mathbf{u}_0^2}{\mathbf{u}^3} - \mu \frac{\mathbf{u}_0}{\mathbf{u}^2}, \quad (2.47)$$

where *div* stands for divergence operator. In the above functional, the last two terms are the data fidelity terms, λ and μ are the regularization parameters (Lagrange multipliers). Here these two Lagrange multipliers are dynamically updated to satisfy the constraints as explained in Rudin et al. (2003). This method is designed for multiplicative Gaussian noise and performs hardly well for the other data-correlated distribution such as Gamma. Nevertheless, many medical and satellite imaging modalities are observed to follow Gamma or Rayleigh distributions, therefore the practical applicability of this models is limited.

2.5.2 Image Restoration in Log Compressed Domain

Image restoration is well explored for data-independent noise distribution such as Gaussian. This paved the way to re-formulate multiplicative models in log compressed domain. An ideal workaround to deal with multiplicative noise in general, is the transformation of the intensities to the log domain, where the noise appears close in similarity to the data-uncorrelated Gaussian. Thereby making the process of despeckling literally similar to Gaussian denoising (for an additive noise model), see Krissian et al. (2005); Shi and Osher (2008); Yahya et al. (2014); Sumaiya and Kumari (2017) for the details. After completing the restoration activity on the transformed data the data needs to be transformed back to its original domain using an inverse logarithmic transform or an exponential transform. Krissian et al. (2005), proposed a technique designed for log compressed images. The noise model considered here is:

$$\mathbf{u}_0 = \mathbf{u} + \sqrt{\mathbf{u}\mathbf{n}}. \quad (2.48)$$

The data fidelity term is derived as: $\int_{\Omega} \frac{(\mathbf{u}_0 - \mathbf{u})^2}{\mathbf{u}}$. The corresponding gradient descent solution is given as:

$$\mathbf{u}_t = \text{div} \left(\frac{\nabla \mathbf{u}}{|\nabla \mathbf{u}|} \right) - \lambda \left(\frac{\mathbf{u}_0^2}{\mathbf{u}^2} - 1 \right). \quad (2.49)$$

However, as known from the literature (Aubert and Aujol, 2008), even in log compressed images the noise does not become totally independent of data. Hence this model does not perform well for speckled images (especially at a higher noise density), where the noise is data-correlated.

Scale-space Method for Convex Multiplicative Noise

Yet another model proposed for the multiplicative noise in Shi and Osher (2008) adopts a strategy based on the log transform to derive a convex functional to yield a globally converging solution. This proposed model is a non-linear scale-space method for convex multiplicative noise, the details are stated below. Consider the multiplicative noise model in (1.8), and perform a log (ln) transform on both sides of the expression to get

$$\ln(\mathbf{u}_0) = \ln(\mathbf{K}\mathbf{u}) + \ln(\mathbf{n}), \quad (2.50)$$

which essentially converts the multiplicative model into an additive one. The additive noise problem has already been successfully treated using the ROF method (Rudin et al., 1992). Now consider $\mathbf{z}_1 = \ln(\mathbf{K}\mathbf{u})$ and $\mathbf{p}_1 = \ln(\mathbf{u}_0)$, this leads to the following convex

optimization problem:

$$\mathbf{z}_1 = \arg \min_{\mathbf{z}_1 \in BV(\Omega)} \left\{ |\nabla \mathbf{z}_1| + \frac{\lambda}{2} \|\mathbf{z}_1 - \mathbf{p}_1\|_{L^2}^2 \right\}. \quad (2.51)$$

Though it provides a globally convex solution to a multiplicative noise model, the restoration efficiency is severely challenged due to the assumption regarding the data-independent nature of the noise. As already pointed out, the log transform cannot completely remove the correlation between the data and the noise.

2.5.3 A Variational Model for Gamma Distribution

Variational formulations started gearing up ever-since Rudin et al. (2003) framed their model to handle multiplicative Gaussian noise. The first initiative in this direction for Gamma noise can be found in Aubert and Aujol (2008) (AA model), where the authors formulated the data fidelity based on the MAP (see Appendix B.2 for the derivation) estimate of the noise distribution and the diffusion term is borrowed from TV regularization. With the above assumptions the model is formulated as:

$$\min_{\mathbf{u}} E(\mathbf{u}) = \min_{\mathbf{u}} \left\{ \int_{\Omega} |\nabla \mathbf{u}| \, dx \, dy + \lambda \int_{\Omega} \left(\ln(\mathbf{u}) + \frac{\mathbf{u}_0}{\mathbf{u}} \right) \, dx \, dy \right\}. \quad (2.52)$$

Duly considering the devise related linear blurring artefacts in the above model, we get

$$\min_{\mathbf{u}} E(\mathbf{u}) = \min_{\mathbf{u}} \left\{ \int_{\Omega} |\nabla \mathbf{u}| \, dx \, dy + \lambda \int_{\Omega} \left(\ln(\mathbf{K}\mathbf{u}) + \frac{\mathbf{u}_0}{(\mathbf{K}\mathbf{u})} \right) \, dx \, dy \right\}, \quad (2.53)$$

where Ω is the area of support and \mathbf{K} is a linear blurring operator. The corresponding Euler Lagrange equation is as follows:

$$-\nabla \cdot \left(\frac{\nabla \mathbf{u}}{|\nabla \mathbf{u}|} \right) + \lambda \mathbf{K}^* \left(\frac{\mathbf{K}\mathbf{u} - \mathbf{u}_0}{(\mathbf{K}\mathbf{u})^2} \right) = 0. \quad (2.54)$$

The gradient descent solution of for equation(2.53) is as follows:

$$\mathbf{u}_t = \operatorname{div} \left(\frac{\nabla \mathbf{u}}{\sqrt{|\nabla \mathbf{u}|^2 + \beta}} \right) + \lambda \mathbf{K}^* \left(\frac{\mathbf{u}_0 - \mathbf{K}\mathbf{u}}{(\mathbf{K}\mathbf{u})^2} \right), \quad (2.55)$$

where $\lambda > 0$ is the Lagrange multiplier, \mathbf{K} is linear blurring operator and for finding the λ value one has to multiply the equation (2.55) with $\mathbf{K}^*(\mathbf{u}_0 - \mathbf{K}\mathbf{u})$, and integrate it over

the image domain i.e.:

$$\lambda = -\frac{1}{\sigma^2} \int_{\Omega} \left(\frac{\nabla \mathbf{u}}{\sqrt{|\nabla \mathbf{u}|^2 + \beta}} \right) \nabla \mathbf{K}^* (\mathbf{u}_0 - \mathbf{K}\mathbf{u}) \, dx \, dy, \quad (2.56)$$

where new data fitting term $H(\mathbf{u}, \mathbf{u}_0) = \int (\ln(\mathbf{K}\mathbf{u}) + \frac{\mathbf{u}_0}{\mathbf{K}\mathbf{u}})$ is strictly convex for $\mathbf{u} \in (0, 2\mathbf{u}_0)$. So the model is conditionally convex. Therefore, a unique solution cannot always be guaranteed. Further, the choice of the parameter β affects the restoration process. For a larger β value the scheme converges faster but the restoration seems to be poor. There should be a trade-off between the accuracy and efficiency in choosing β .

2.5.4 A Convex Regularization Model for Multiplicative Noise

The conditionally convex nature of the Aubert and Aujol (2008) model was concerning the research community, as a unique solution could not be guaranteed for this model. In Huang et al. (2009), the authors derive a convex functional (for removing multiplicative noise), which is unconditionally convex. They consider an auxiliary variable $\mathbf{z}_1 = \ln(\mathbf{u})$ and $\mathbf{K} = \mathbf{I}$ substitute in the Aubert Aujol model. The unconstrained denoising problem is given by

$$\min_{\mathbf{z}_1} \left\{ E(\mathbf{z}_1) = \int_{\Omega} |\nabla \mathbf{z}_1| \, dx \, dy + \lambda \int_{\Omega} (\mathbf{z}_1 + \mathbf{u}_0 e^{-\mathbf{z}_1}) \, dx \, dy \right\}. \quad (2.57)$$

The corresponding gradient descent equation follows the definition

$$\mathbf{z}_{1_t} = \text{div} \left(\frac{\nabla \mathbf{z}_1}{\sqrt{|\nabla \mathbf{z}_1|^2 + \beta}} \right) - \lambda (1 - \mathbf{u}_0 e^{-\mathbf{z}_1}). \quad (2.58)$$

The main advantage of using new fidelity term $(\mathbf{z}_1 + \mathbf{u}_0 e^{-\mathbf{z}_1})$ is that its second derivative with respect to \mathbf{z}_1 is $\mathbf{u}_0 e^{-\mathbf{z}_1}$. Therefore new fidelity term is strictly convex for all values of \mathbf{z}_1 . The main advantage of this new model is that, it provides a theoretically stable solution which converges globally to a unique solution. However, this method also converges slowly similar to many other second order gradient descent methods.

2.5.5 Multiplicative Noise Removal via a Novel Variational Model

Huang et al. (2010) proposed a non-convex Bayesian type variational model for multiplicative noise removal, which includes the total variation (TV) and Weberized TV as regularizes. This method is superior to the AA model in terms of the visual appearance

of the filtered image. The energy minimization problem considered in this work is

$$\min_{\mathbf{u}} \left\{ E(\mathbf{u}) = \alpha_1 \int_{\Omega} |\nabla \mathbf{u}| \, dx \, dy + \alpha_2 \int_{\Omega} \frac{|\nabla \mathbf{u}|}{\mathbf{u}} \, dx \, dy + \int_{\Omega} \left(\ln(\mathbf{u}) + \frac{\mathbf{u}_0}{\mathbf{u}} \right) \, dx \, dy \right\}. \quad (2.59)$$

Here α_1 and α_2 are the regularization parameters, taking $\phi(\mathbf{u}) = \alpha_1 + \frac{\alpha_2}{\mathbf{u}}$, the gradient descent solution can be written as

$$\mathbf{u}_t = \phi(\mathbf{u}) \operatorname{div} \left(\frac{\nabla \mathbf{u}}{|\nabla \mathbf{u}|} \right) + \left(\frac{\mathbf{u}_0 - \mathbf{u}}{\mathbf{u}^2} \right). \quad (2.60)$$

Though, the weberized TV model works better than normal TV model in terms of the intensity enhancement, it carries all the drawbacks of a second order variational model under a gradient descent scheme.

2.5.6 A Convex Regularization Model for Image Restoration

Jidesh (2014) introduced a new variational method that can handle blocky effect by using a convex combination of TV and Tikhonov filter which are defined in the space of bounded variation $(BV(\Omega))^1$ and an L^2 (square integrable function) spaces, respectively further, the author assumes that $\mathbf{K} = \mathbf{I}$. The corresponding energy minimization problem is given as follows:

$$\min_{\mathbf{u}} \left\{ E(\mathbf{u}) = \int_{\Omega} |\nabla \mathbf{u}| \, dx \, dy + \lambda_1 \int_{\Omega} \left(\ln(\mathbf{u}) + \frac{\mathbf{u}_0}{\mathbf{u}} \right) \, dx \, dy \right\}, \quad (2.61)$$

and

$$\min_{\mathbf{v}} \left\{ E(\mathbf{v}) = \int_{\Omega} |\nabla \mathbf{v}|^2 \, dx \, dy + \lambda_2 \int_{\Omega} \left(\ln(\mathbf{v}) + \frac{\mathbf{v}_0}{\mathbf{v}} \right) \, dx \, dy \right\}, \quad (2.62)$$

The gradient descent solutions of equations (2.61) and (2.62) are as follows:

$$\mathbf{u}_t = \operatorname{div} \left(\frac{\nabla \mathbf{u}}{|\nabla \mathbf{u}|} \right) + \lambda_1 \left(\frac{\mathbf{u}_0 - \mathbf{u}}{\mathbf{u}^2} \right), \quad (2.63)$$

$$\mathbf{v}_t = (\nabla^2 \mathbf{v}) + \lambda_2 \left(\frac{\mathbf{v}_0 - \mathbf{v}}{\mathbf{v}^2} \right). \quad (2.64)$$

The proposed technique is given as:

$$\mathbf{u} = \phi(\mathbf{c}) \mathbf{v}_t + (1 - \phi(\mathbf{c})) \mathbf{u}_t, \quad (2.65)$$

¹ $BV(\Omega)$ is the space where total variation: $\int_{\Omega} |\nabla u| \, dx \, dy < \infty$ is bounded.

where \mathbf{c} denotes $|\nabla \mathbf{u}|$, the function $\phi(\mathbf{c}) = \frac{1}{1+\mathbf{c}}$. However, as this is an extension of Aubert and Aujol (2008) method, this method also possesses some of the drawbacks such as slow convergence, non-unique nature of the functional (leading to sub-optimal solutions) etc.

However, adopting a TV prior to the regularization term makes the results less appealing due to heavy penalization of gradient oscillations present in the textured data. Preserving image features is an important activity as far as most of the imaging modalities are concerned. As observed in many modalities, image features play a vital role in characterizing the objects present in images. This comes handy when dealing with medical and satellite image data. There are some models which are specially designed to cater these image features. The details follow.

2.6 Non-local Total Variation (NLTV) Regularization

These non-local models are motivated by the Non-Local Means (NLM) filter proposed by Buades et al. (2005) and its variational version proposed by Gilboa and Osher (2008). The TV model under a non-local framework takes the following form:

$$\min_{\mathbf{u}} J_{\text{NLTV}}(\mathbf{u}) + \lambda \|\mathbf{K}\mathbf{u} - \mathbf{u}_0\|_{L^2}^2. \quad (2.66)$$

Here $\|\cdot\|_{L^2}$ denotes the usual L^2 norm of the functional and $J_{\text{NLTV}}(\mathbf{u})$ denotes the non-local Total Variation defined as:

$$\begin{aligned} J_{\text{NLTV}}(\mathbf{u}) &= \int_{\Omega \times \Omega} \phi(|\nabla_{\text{NL}} \mathbf{u}|^2) \, dx \, dy, \\ &= \int_{\Omega} \phi \left(\int_{\Omega} (\mathbf{u}(y) - \mathbf{u}(x))^2 \mathbf{w}(x,y) \, dy \right) \, dx. \end{aligned} \quad (2.67)$$

The non-local Gradient in the above expression $\nabla_{\text{NL}} \mathbf{u}(x) : \Omega \rightarrow \Omega \times \Omega$ is defined as

$$(\nabla_{\text{NL}} \mathbf{u})(x,y) = (\mathbf{u}(y) - \mathbf{u}(x)) \sqrt{\mathbf{w}(x,y)}. \quad (2.68)$$

The non-local divergence of the non-local vector $\text{div}_{\text{NL}} \vec{v} : \Omega \times \Omega \rightarrow \Omega$ is defined as follows:

$$\text{div}_{\text{NL}} \mathbf{d}(x) = \int_{\Omega} (\mathbf{d}(x,y) - \mathbf{d}(y,x)) \sqrt{\mathbf{w}(x,y)} \, dy : \Omega \rightarrow \mathbb{R}. \quad (2.69)$$

(see Gilboa and Osher (2008)) and non-local Laplacian is

$$\Delta_{\text{NL}}(\mathbf{u}(k)) = \sum_{l \in \mathcal{N}_k} \mathbf{w}(k,l) (\mathbf{u}(l) - \mathbf{u}(k)) \quad (2.70)$$

where $\mathbf{w}(x, y)$ is the smoothing non-local window function given by

$$\mathbf{w}(x, y) = \mathbf{d}_\sigma(x, y)^{-2} \quad (2.71)$$

and the distance function is given by

$$\mathbf{d}_\sigma(\mathbf{u}(x), \mathbf{u}(y)) = \int_{\Omega} G_\sigma(t) |\mathbf{u}(x+t) - \mathbf{u}(y+t)|^2 dt \quad (2.72)$$

where $G_\sigma(t)$ denotes the Gaussian convolved version of t with σ as the spread of the Gaussian kernel.

The models discussed so far have their own pros and cons. As already examined in the literature most second order nonlinear models converge to piece-wise linear functions in the course of their evolution and results in staircase formation in the restored data. They eventually fail to respect the local gradient oscillations causing severe damages to the detailed structures present in the data. These facts motivate us to propose models which can handle the major setbacks of the second order diffusion models while restoring the images. Yet another common requirement for any diffusion method is the fast convergence rate which opens up the possibility of its real-time implementations. Since we deal with data-correlated noise distribution (which are non-Gaussian models) the noise statistics play a vital role in the design of a model. The rest of the thesis is dedicated to analyze the aforementioned issues and provide favourable solutions.

In the next chapter, we try to explore the possibility of introducing a novel framework, where the model restores images with due care to the edges and fine details. Moreover, the devise artefacts resulting in linear blurring phenomena is also being handled by the proposed framework. The convergence rate of the model is reasonably improved by employing a faster technique like the Augmented Lagrangian method instead of the commonly used explicit schemes.

Chapter 3

DESPECKLING ULTRASOUND IMAGES USING NON-LOCAL TOTAL BOUNDED VARIATION REGULARIZATION

3.1 Introduction

Ultrasound is one of the widely used modalities in medical imaging due to its capability to provide images of moderately good quality without using the ionizing radiations. Moreover, the method is non-invasive in nature and causes relatively less harm to the subject. There are different models of US imaging and most of the conventional systems employ amplitude based or intensity based techniques for acquiring images. In amplitude based techniques, the amplitude of the sound signal is recorded as a function of time and in intensity based techniques intensity is used in place of amplitude. There are other US models as well and some of them use Doppler frequency information, see Stergiopoulos (2000) for details. A detailed description of US image formation and speckle generation was given in the subsection A.1.1. However, to ensure the continuity in the explanation and improve the readability of the thesis some of the concepts relevant to the present chapter have been revisited here.

Ultrasound signals transmitted by the systems undergo three major types of scattering depending on the characteristic of the object on which it is falling. The major types of scattering are specular, diffusive and diffractive. The specular scattering is due to the large size of the object compared to the wavelength of the signal and causes speckles in the captured data. Due to the presence of the speckles the signal intensity shoots up at the concerned pixel value causing the signal to fluctuate its the intensity values between a high range. It is shown in Huang et al. (2009) that when the scatter density is more than 10 the speckle noise is found to follow Rayleigh distribution. However, the images (both satellite and medical) are formed adding different image slices whose

intensity values follows a negative exponential law and the summed data is found to follow Gamma law. In US and SAR imaging the intensity of the resultant image is formulated as a product of reflectance of the sound and speckle (i.e., $\mathbf{u}_0 = \mathbf{u} \times \mathbf{n}$) therefore, the speckles are also found to follow the Gamma law.

This Chapter is arranged as follows. In the Section 3.2 the novel contributions of the proposed work is highlighted. Further, in the Section 3.3 the proposed framework for restoration of the images corrupted with data-correlated speckle and linear blurring artefacts is detailed. Section 3.4 covers the numerical implementation of the model using the Augmented Lagrangian (AL) framework. And finally we give detailed experimentation results in the Section 3.5.

3.2 Contributions of the Proposed Model

The variational methods discussed so far are either the variants of Aubert and Aujol (2008) (AA) model, where the regularization term is a TV norm of the image functional or log transformed versions of multiplicative noise modalities (Krissian et al., 2005; Shi and Osher, 2008). In the first category of methods, (i.e., AA model and its variants) the TV norm in the regularization term eventually leads to piecewise linear approximation of the output; causing visual discrepancies. On the other hand, in the second category, (log transformed techniques) the signal-noise correlation is completely neglected under the assumption that the noise is independent of the data in the log domain. These setbacks are effectively addressed in this research work by introducing a novel regularization framework whose unique contributions are detailed below.

In this chapter, we design a model with a non-local total bounded variation prior in place of the ordinary TV norm prior to preserve edges and local gradient oscillations while reducing the device dependent blurring artefacts. The reactive term of the model is designed to handle the existing noise-signal correlation, duly caring the distribution of noise in the data. Moreover, the fast computation of the model has been ensured by employing AL method in place of the explicit methods, which categorically opens up a possibility for its real-time implementation in real-world applications. The regularization parameter is evaluated in each iteration (instead of hard-coding the same for each input data) considering the noise variance evaluated using MLE of the input data. Furthermore, a detailed theoretical study is employed to analyze the condition for existence of a unique solution of the model and its convergence characteristics. The detailed design of the model is discussed in the next section.

3.3 The Proposed Variational Speckle Reduction Model

As already introduced in the Chapter 1, speckles are data-dependent and modeled as

$$\mathbf{u}_0 = \mathbf{K}\mathbf{u}\mathbf{n}, \quad (3.1)$$

where \mathbf{n} represents the multiplicative speckles following the Gamma law and \mathbf{K} is the linear blurring operator. Now borrowing the concepts from the non-local TV (NLTV) in Gilboa and Osher (2008) and Aubert and Aujol (2008) (models discussed in the previous chapter), we derive the following non-local framework for handling speckles:

$$\min_{\mathbf{u}} \int_{\Omega} |\nabla_{\text{NL}}\mathbf{u}| dx dy + \lambda \int_{\Omega} \left(\ln(\mathbf{K}\mathbf{u}) + \frac{\mathbf{u}_0}{(\mathbf{K}\mathbf{u})} \right) dx dy. \quad (3.2)$$

The above model is derived based on the MAP method discussed in Aubert and Aujol (2008), see Appendix B.2 for the details of the derivation. Now taking the non-local total Bounded Variation (BV) norm in place of TV norm gives:

$$\min_{\mathbf{u}} \int_{\Omega} \left(|\nabla_{\text{NL}}\mathbf{u}| + \frac{\beta}{2} \|\mathbf{u}\|_{L^2}^2 \right) dx dy + \lambda \int_{\Omega} \left(\ln(\mathbf{K}\mathbf{u}) + \frac{\mathbf{u}_0}{(\mathbf{K}\mathbf{u})} \right) dx dy. \quad (3.3)$$

where $\beta > 0$, is a small positive scalar constant that controls the magnitude of NLTV and L^2 norms of the regularization term. Employing non-local total BV norm in place of the NLTV norm provides better visual appeal to the restored output due to the presence of the extra penalty term and the details are discussed in Liu and Huang (2010). The mathematical analysis of the proposed model is given in Appendix B.1, where the existence and uniqueness of the solution of the model is discussed in detail.

3.4 Numerical Implementation using Augmented Lagrangian

To solve the (3.3), first we introduce an auxiliary variable \mathbf{d} for $\nabla_{\text{NL}}\mathbf{u}$ and transform problem (3.3) into an equivalent problem as follows:

$$\min_{\mathbf{u}, \mathbf{d}} \int_{\Omega} \left(|\mathbf{d}| + \frac{\beta}{2} \|\mathbf{u}\|_{L^2}^2 \right) dx dy + \lambda \int_{\Omega} \left(\ln(\mathbf{K}\mathbf{u}) + \frac{\mathbf{u}_0}{(\mathbf{K}\mathbf{u})} \right) dx dy \quad (3.4)$$

subject to $\mathbf{d} = \nabla_{\text{NL}}\mathbf{u}$.

The augmented Lagrangian of the above equation is:

$$\begin{aligned} \min_{\mathbf{u}, \mathbf{d}} \max_{\mathbf{b}} L_{NLTV}(\mathbf{u}, \mathbf{d}, \mathbf{b}) &= \int_{\Omega} \left(|\mathbf{d}| + \frac{\beta}{2} \|\mathbf{u}\|_{L^2}^2 \right) + \lambda \int_{\Omega} \left(\ln(\mathbf{K}\mathbf{u}) + \frac{\mathbf{u}_0}{(\mathbf{K}\mathbf{u})} \right) \\ &+ \int_{\Omega} \mathbf{b} \cdot (\mathbf{d} - \nabla_{NL}\mathbf{u}) + \frac{g}{2} \int_{\Omega} \|\mathbf{d} - \nabla_{NL}\mathbf{u}\|_{L^2}^2, \end{aligned} \quad (3.5)$$

where g is a positive scalar constant and $\mathbf{b} \in \mathbb{R}^N \times \mathbb{R}^N$ is yet another Lagrange multiplier and “ \cdot ” denotes the standard inner product. The idea of the Augmented Lagrangian method is to find a saddle point of $L_{NLTV}(\mathbf{u}, \mathbf{d}, \mathbf{b})$, which is also the solution of original problem in (3.3).

The Augmented Lagrangian method uses an iterative procedure to solve (3.5), see Algorithm 1. The iterative scheme runs until some stopping condition is satisfied. To solve the problem (3.12) it is divided into the following two sub-problems (Wang et al., 2008, 2007).

$$\begin{aligned} \mathbf{u}_{n+1} = \arg \min_{\mathbf{u}} & \int_{\Omega} \lambda \left(\ln(\mathbf{K}\mathbf{u}) + \frac{\mathbf{u}_0}{(\mathbf{K}\mathbf{u})} \right) + \int_{\Omega} \frac{\beta}{2} \|\mathbf{u}\|_{L^2}^2 \\ & + \int_{\Omega} \mathbf{b}_n \cdot (\mathbf{d} - \nabla_{NL}\mathbf{u}) + \frac{g}{2} \int_{\Omega} \|\mathbf{d} - \nabla_{NL}\mathbf{u}\|_{L^2}^2 \end{aligned} \quad (3.6)$$

and

$$\mathbf{d}_{n+1} = \arg \min_{\mathbf{d}} \left\{ \int_{\Omega} |\mathbf{d}| + \int_{\Omega} \mathbf{b}_n \cdot (\mathbf{d} - \nabla_{NL}\mathbf{u}) + \frac{g}{2} \int_{\Omega} \|\mathbf{d} - \nabla_{NL}\mathbf{u}\|_{L^2}^2 \right\}, \quad (3.7)$$

when solving the \mathbf{u} sub-problem in (3.6), the optimality condition gives a linear equation of the form

$$\lambda \left(\frac{\mathbf{K}^*(\mathbf{K}\mathbf{u} - \mathbf{u}_0)}{(\mathbf{K}\mathbf{u})^2} \right) + \beta\mathbf{u} + \nabla_{NL}\mathbf{b} - g\nabla_{NL} \cdot (\mathbf{d} - \nabla_{NL}\mathbf{u}) = 0, \quad (3.8)$$

where \mathbf{K}^* is the adjoint of the operator \mathbf{K} . Hence, (3.8) has a solution:

$$\mathbf{u}_{n+1} = \mathcal{F}^{-1} \left[\frac{\mathcal{F}[\lambda\mathbf{K}^*\mathbf{u}_0 + (\mathbf{K}\mathbf{u})^2(g\nabla_{NL}\mathbf{d} - \nabla_{NL}\mathbf{b})]}{\lambda|\mathcal{F}[\mathbf{K}]|^2 + g|\mathcal{F}[\Delta_{NL}]|(\mathbf{K}\mathbf{u})^2 + \beta(\mathbf{K}\mathbf{u})^2} \right] \quad (3.9)$$

where \mathcal{F} and \mathcal{F}^{-1} denotes the Fourier transform and inverse Fourier transform, respectively. To solve \mathbf{d} sub-problem (3.7), the shrinkage formula is being used, as given below:

$$\mathbf{d}_{n+1} = \mathit{shrink}(\nabla_{NL}\mathbf{u} - \frac{\mathbf{b}}{g}, \frac{1}{g}), \quad (3.10)$$

where

$$\mathit{shrink}(x, y) = \frac{x}{|x|} * \max(|x| - y, 0). \quad (3.11)$$

The parameter λ (regularization parameter / Lagrangian multiplier) is evaluated and updated as mentioned in Appendix B.4. As noticed in many previous works, the parameter λ is a function of the noise variance σ^2 , therefore the noise variance needs to be estimated for an arbitrary noisy data. This is done using the MLE as detailed in Appendix B.3.

Algorithm 1: Augmented Lagrangian method for the non local total bounded variation model

Initialization: \mathbf{u}_0 = initial noisy image, $\mathbf{d}_0 = 0, \mathbf{b}_0 = 0; \varepsilon = 10^{-4}$

while $\frac{\|\mathbf{u}_{n+1} - \mathbf{u}_n\|}{\|\mathbf{u}_{n+1}\|} > \varepsilon$ **do**

Compute $(\mathbf{u}_{n+1}, \mathbf{d}_{n+1})$ as a minimizer of the Augmented Lagrangian method for the Lagrange multiplier \mathbf{b}_n , i.e.,

$$(\mathbf{u}_{n+1}, \mathbf{d}_{n+1}) = \arg \min_{\mathbf{u}, \mathbf{d}} L_{\text{NLTV}}(\mathbf{u}, \mathbf{d}, \mathbf{b}_n), \quad (3.12)$$

where $L_{\text{NLTV}}(\mathbf{u}, \mathbf{d}, \mathbf{b}_n)$ is defined in equation(3.5) and update

$$\mathbf{b}_{n+1} = \mathbf{b}_n + g(\mathbf{d}_{n+1} - \nabla_{\text{NL}} \mathbf{u}_{n+1}) \quad (3.13)$$

and λ using (B.32).

Increment n.

3.5 Experimental Results and Discussion

In this section, experimental results are presented to demonstrate the performance of the studied restoration method. The efficiency of the studied restoration method has been tested using different category of test images such as Lena (a natural image), satellite image, synthetic image and original US images of human liver, hepatic vein, kidney and women breast. These images (except the real speckled images) are also tested under various noise and blur degradations (synthetically generated using Matlab code). The noise parameters (for the Gamma distributed noise) shape and scale are set manually for synthetically generated noisy images and they are estimated based on MLE for the original noisy data. The parameter estimation process is described in Appendix B.3. All test images in its original form are shown in Figure 3.1. Various state-of-the-art despeckling models available in the literature are being compared with the proposed restoration method. The PDE based models such as DPAD and OSRAD along with

the variational model proposed in Aubert and Aujol (2008) and its non-local version (with explicit scheme and Augmented Lagrangian formulation) are considered here for the comparative study. Furthermore, the state-of-the art non-local averaging model in K. Dabov and Egiazarian (2007) is also being used for the comparative purpose. The results obtained after processing these input images using various methods discussed above are shown in this section. Figures 3.2, 3.3 and 3.4, show images (Lena, phantom and satellite) restored using various methods (the input images are artificially corrupted with synthetic noise). Figures 3.5, 3.6, 3.7 and 3.8, show results for real US input speckled images (obtained from <http://www.medison.ru/ultrasound/>). The figure captions highlight the corresponding method used for the restoration. The proposed restoration model is shown in sub-figure (i) of each figure. The enlarged portion portion of the phantom image is shown in Figure 3.10.

The performances of various comparative methods are demonstrated in the Figures 3.2, 3.3, 3.4, 3.5, 3.6, 3.7 and 3.8 as discussed above. From these results one can observe that the PDE based models such as SRAD, DPAD and OSRAD performs a non-linear and anisotropic diffusion to regularize the data. Nevertheless, they fail to preserve the resolution leading to piecewise patch formation in the output. The textures and details are severely penalized in the course of the evolution. Moreover, the PDE models do not possess a functional which can be studied theoretically to substantiate various properties of the model such as stability, uniqueness convergence etc. In the variational framework the AA model and its non-local version are comparatively easy to analyse theoretically as the functional is readily available in these models. These models are designed under a Bayesian framework to duly care about the noise distribution while designing the functional. Moreover, the non-local version of AA model preserves textures to a better extent compared to the PDE counterparts. Nevertheless, the piecewise approximation of the functional still prevails in these models. The proposed strategy uses a total-bounded variation functional in place of ordinary TV functional, the functional thus designed can reduce the piecewise functional approximation as it combines both L^1 and L^2 norms by appropriately weighing them. Therefore, the results are found to be more impressive in comparison to the other comparative models.

As one can observe, the restoration with the given model outperforms other models (visually) in terms of despeckling and de-blurring of the images.

The results obtained for seven input images are shown in this experimental study. The images belong to various categories such as: a partially textured natural image, a non-textured synthetic image, a satellite image and four US images. As we can observe from the Figure 3.2 (i), that the proposed strategy has retained finer details and edges present in the data and moreover the homogeneous regions are despeckled considerably.

The deblurring effect of the filter is obvious from the result. Similarly, in Figure 3.3 (i) the despeckled results of a synthetic image (synthetically corrupted with speckles and blur) is demonstrated, the constant intensity regions, corners and edges are preserved well by the proposed strategy and the regions are despeckled well in comparison to the other models. Figure 3.4(i) shows the restoration results of a satellite image (corrupted with speckle and blur), the details are preserved by the proposed model in this case too. Finally the restoration capability of the proposed model is well demonstrated in case of US images in Figures 3.5 - 3.8. These figures contain numerous details which are duly respected in the evolution of the proposed model. Moreover, the local gradient oscillations are evidently recovered in the proposed restoration model.

The relative error is plotted against the number of iterations in Figure 3.9. As observed from this figure the relative error of the proposed model becomes steady after a finite number of iterations. This provides a notion of convergence. The details are given in Appendix B.5.

The performance of various models considered for the comparative purpose is evaluated using the statistical quantifiers such as the peak signal to noise ratio(PSNR) and the structural similarity index measure(SSIM) (Wang et al., 2004) . The PSNR is defined using mean squares error (MSE) as follows. Given original image u and its noisy approximation u_0 , MSE is defined as follows:

$$MSE = \frac{1}{mn} \sum_{i=0}^{m-1} \sum_{j=0}^{n-1} (\mathbf{u}(i, j) - \mathbf{u}_0(i, j))^2. \quad (3.14)$$

The PSNR (in dB) is defined as:

$$PSNR = 10 \log_{10} \frac{MAX_{\mathbf{u}}^2}{MSE}, \quad (3.15)$$

where MAX_u is the maximum possible pixel value of the image. A higher PSNR value indicates a better noise removal and in the sequel, a good restoration. The SSIM indicates the structure and contrast preservation ability of the model under consideration. The values obtained under this measure are in the range $[0 - 1]$, where 0 and 1 indicates, poor and ideal preservation capabilities, respectively. It is evaluated on various windows from an image. The measure between two windows x_1 and x_2 of size $N \times N$ is

$$SSIM(\mathbf{u}, \mathbf{u}_0) = \frac{(2\mu_{\mathbf{u}}\mu_{\mathbf{u}_0} + C_1)(2\sigma_{\mathbf{u}\mathbf{u}_0} + C_2)}{(\mu_{\mathbf{u}}^2 + \mu_{\mathbf{u}_0}^2 + C_1)(\sigma_{\mathbf{u}}^2 + \sigma_{\mathbf{u}_0}^2 + C_2)}, \quad (3.16)$$

where $\mu_{\mathbf{u}}$ and $\mu_{\mathbf{u}_0}$ are averages of \mathbf{u} and \mathbf{u}_0 respectively, $\sigma_{\mathbf{u}}$ and $\sigma_{\mathbf{u}_0}$ are the variances of \mathbf{u} and \mathbf{u}_0 respectively and $\sigma_{\mathbf{u}\mathbf{u}_0}$ is the covariance of \mathbf{u} and \mathbf{u}_0 . C_1 and C_2 are two

positive constants to stabilize the division with weak denominator.

The PSNR and SSIM values are tabulated in Tables 3.1 and 3.2, respectively (note that the PSNR and SSIM values are evaluated only for images whose ground-truth is available). The statistical verifications are in line with the visual inferences. The PSNR and SSIM denotes the denoising and structure preserving capabilities of the models under consideration. The PDE based models such as SRAD, OSRAD and DPAD performs at par with the other models as the diffusion results in denoising. The average PSNR of the restored images for these models amount to 25 dB approximately. Whereas, the PSNR values shows a considerable difference among the models for the PDE models the average performance in terms of SSIM is close to 0.75, whereas the value is 0.8 and 0.83, respectively for variational models (AA and NLTV) and the proposed one. The performance is well justified by the characteristics of the total bounded variation norm.

As one can observe, the values corresponding to the given restoration model is higher in comparison to the other models. As mentioned earlier, PSNR denotes the noise removing capacity of the method and SSIM indeed shows the extent of structure and contrast preservation. These values in-turn indicate the denoising and deblurring capability of the model in quantitative terms. The number of iterations required for each method to converge is shown in Table 3.3. As evident from this table, the given restoration method takes less number of iterations to converge to the desired solution. The fast convergence of the proposed method is due to its implementation under AL scheme, whereas the other iterative models use explicit time marching schemes. The faster convergence is justified by the adoption of Augmented Lagrangian scheme instead of the usual explicit schemes. The parameter sensitivity of each model is demonstrated in Tables 3.4 and 3.5 for synthetically corrupted and real noisy images respectively. The values chosen for each parameter in various methods are tabulated in Tables 3.4 and 3.5. The values are empirically set to obtain the optimal results in terms of visual and quantitative representations. It is worth noting that the performance of all these iterative schemes is considerably impacted by the choice of these parameter values.

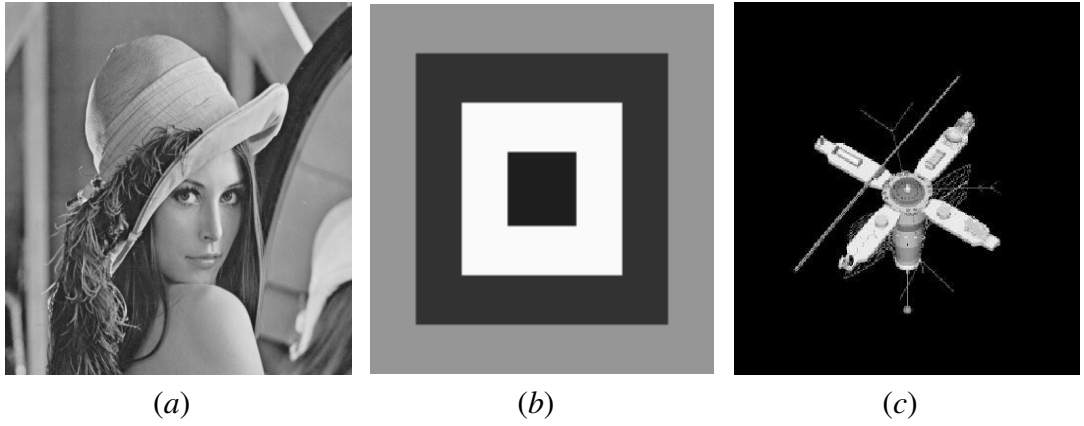


Figure 3.1 Images [(a) Lena (b) Synthetic (c) Satellite] in their original form.

Table 3.1 PSNR (Blurring kernel size and noise variance: 2, 0.1, respectively) evaluated for different images using various restoration models.

Image name	Noisy & Blurred image	SRAD	DPAD	OSRAD	AA	NLTV	BM3D	NLTVAL	Proposed method
Lena	25.83	26.35	26.45	26.48	27.37	27.46	27.65	26.14	27.89
Satellite	25.26	25.53	25.71	25.80	26.70	26.28	25.68	25.56	26.97
Synthetic	19.42	21.12	21.42	21.65	22.55	22.46	22.68	22.65	22.96

Table 3.2 SSIM (Blurring kernel size and noise variance: 2, 0.1, respectively) evaluated for different images using various restoration models.

Image name	Noisy & Blurred image	SRAD	DPAD	OSRAD	AA	NLTV	BM3D	NLTVAL	Proposed method
Lena	0.60	0.72	0.74	0.75	0.77	0.76	0.77	0.77	0.78
Satellite	0.85	0.87	0.89	0.89	0.90	0.91	0.91	0.90	0.91
Synthetic	0.49	0.75	0.80	0.80	0.82	0.85	0.82	0.82	0.83

In summary, the designed model is capable of restoring images from their speckled

Table 3.3 Number of iterations taken by each method to converge to the desired solution for various test images.

Image name	Noisy & Blurred image	SRAD	DPAD	OSRAD	AA	NLTV	NLTVAL	Proposed method
Lenna	0.1,2	600	610	550	400	250	55	50
Satellite	0.1,2	500	710	500	500	250	50	50
Synthetic	0.1,2	450	420	400	350	250	60	52
Liver	-	350	350	250	200	150	45	40
Hepatic vein	-	500	450	450	350	200	50	45
Kidney	-	360	355	240	190	130	35	30
Women breast	-	450	420	410	250	150	40	35

Table 3.4 Different parameter values used for the test images: Lena, satellite and synthetic images (corrupted by blur and noise variance $\{2, 0.1, 2, 0.2\}$, respectively) under various restoration models.

Method Name	λ	δ	β	g
SRAD	{0.01,0.03}	-	-	-
DPAD	{0.01,0.04}	-	-	-
OSRAD	{0.009,0.02}	-	-	-
AA	{0.01,0.02}	{0.09,0.047}	-	-
NLTV	{0.01,0.03}	{0.002,0.002}	-	-
NLTVAL	{9.5,5.1}	-	-	{0.033,0.032}
Proposed method		-	{0.001,0.001}	{0.05,0.55}

Table 3.5 Different parameter values used for the real US test images under various restoration models.

Method Name	λ	δ	β	g
SRAD	{0.03,0.04}	-	-	-
DPAD	{0.02,0.048}	-	-	-
OSRAD	{0.012,0.025}	-	-	-
AA	{0.018,0.029}	{0.15,0.071}	-	-
NLTV	{0.01,0.03}	{0.0052,0.0042}	-	-
NLTVAL	{11,7.4}	-	-	{0.053,0.042}
Proposed method		-	{0.0021,0.0031}	{0.05,0.65}

and blurred observation without significantly disturbing the inherent image features present in them. This makes it ideal for US imaging applications where the images are speckled and blurred and moreover, the image contains significant details in it. The study has proved the efficiency of the model using a large set of test data from the ultrasound imaging domain. In the next Chapter we design another despeckling cum deblurring model designed specifically for SAR imagery.



Figure 3.2 (a) Speckled and Blurred Lena image [Gamma noise variance: 0.1 and Blur kernel size: 2] (b) The restored image by SRAD method (c) The restored image by DPAD method (d) The restored image by OSRAD method (e) The restored image by AA method (f) The restored image by NLTv method (g) The restored image by BM3D method (h) The restored image by NLTv using AL method (i) The restored image by proposed method

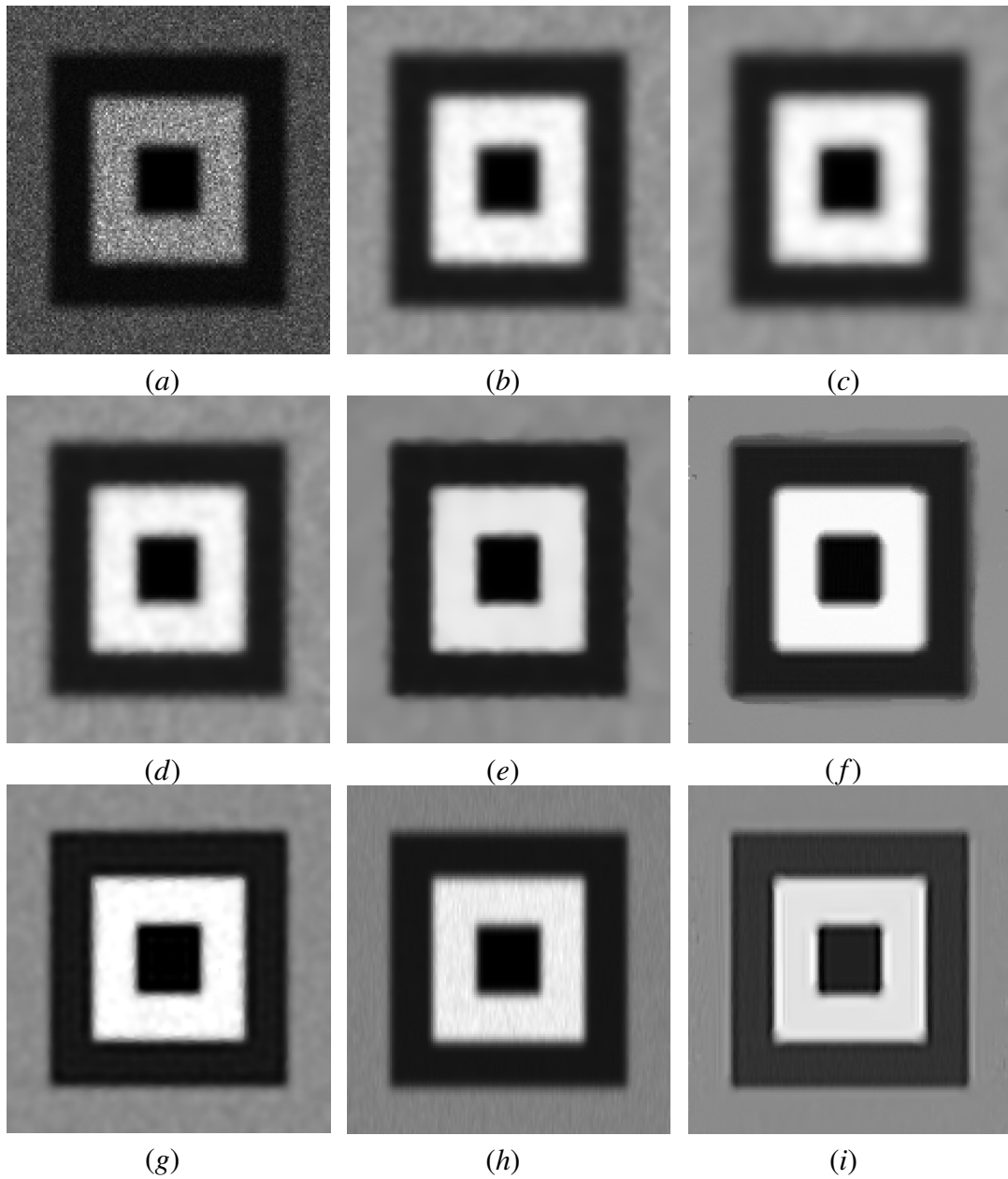


Figure 3.3 (a) Speckled and blurred phantom image [Gamma noise variance: 0.1 and Blur kernel size: 2] (b) The restored image by SRAD method (c) The restored image by DPAD method (d) The restored image by OSRAD method (e) The restored image by AA method (f) The restored image by NLTV method (g) The restored image by BM3D method (h) The restored image by NLTV using AL method (i) The restored image by proposed method

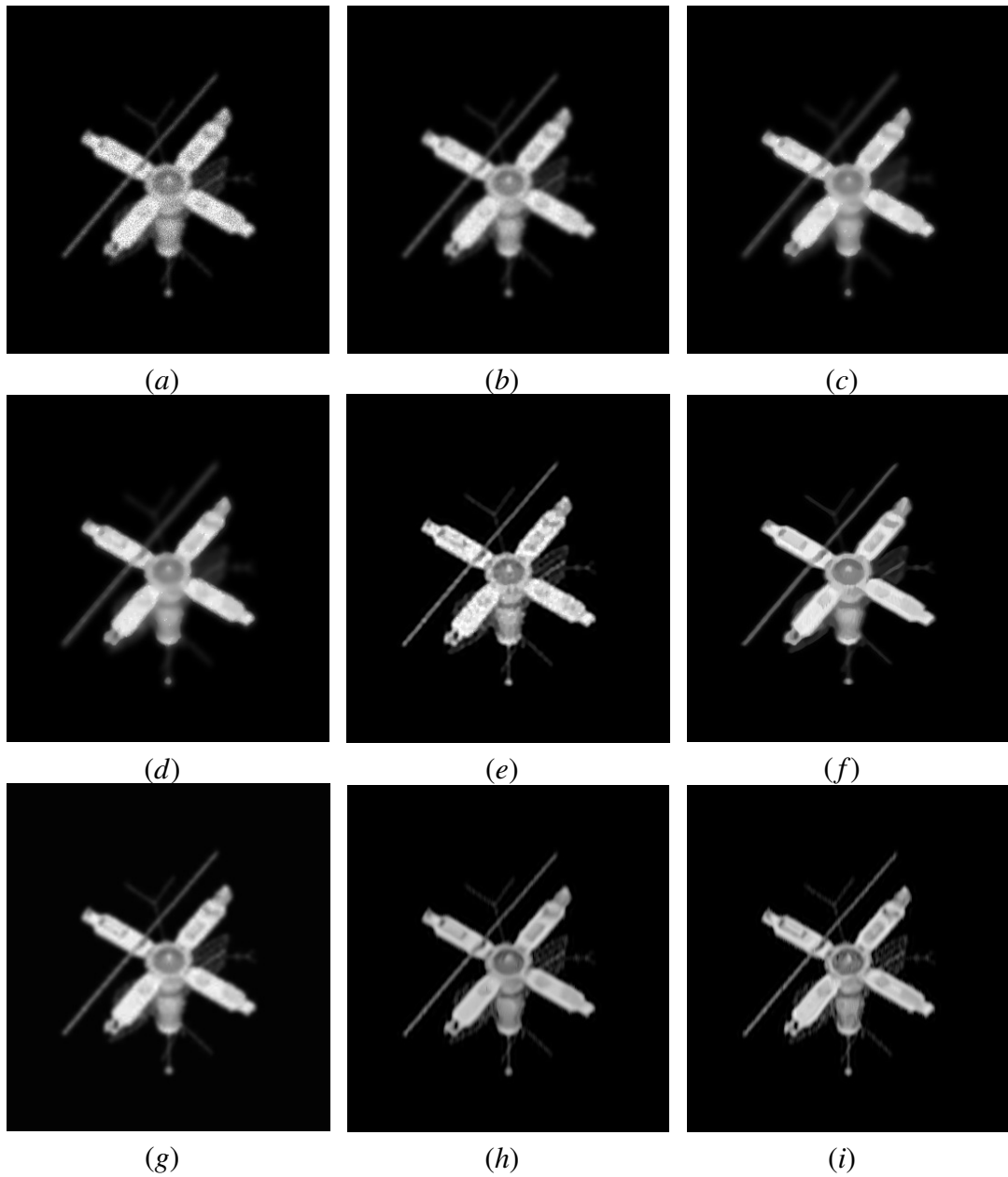


Figure 3.4 (a) Speckled and Blurred Satellite image [Gamma noise variance: 0.1 and Blur kernel size: 2] (b) The restored image by SRAD method (c) The restored image by DPAD method (d) The restored image by OSRAD method (e) The restored image by AA method (f) The restored image by NLTV method (g) The restored image by BM3D method (h) The restored image by NLTV using AL method (i) The restored image by proposed method

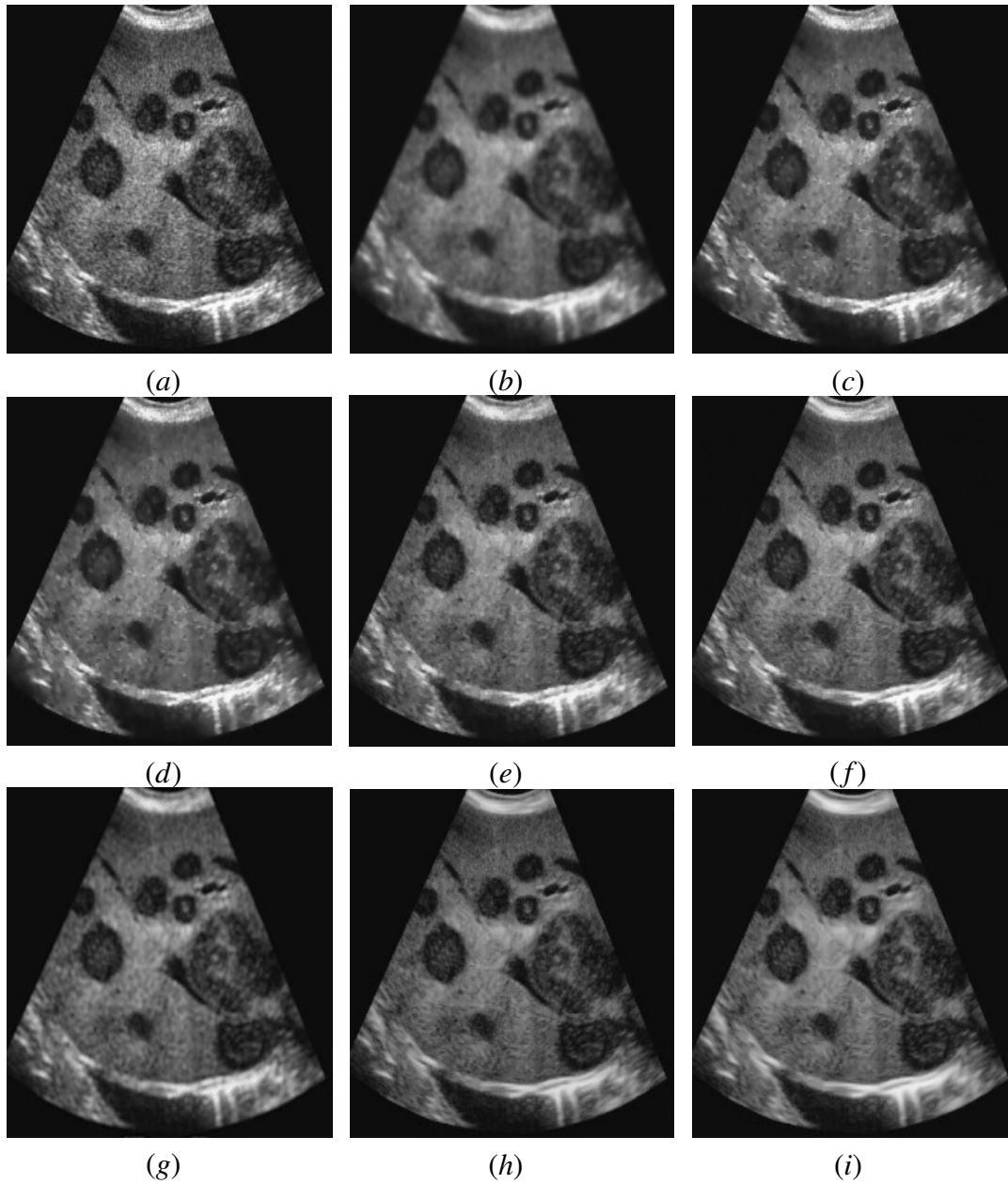


Figure 3.5 (a) Original ultrasound image of human Liver (Speckled and Blurred image) (b) Image restored by SRAD (c) The image restored by DPAD (d) The image restored by OSRAD (e) The image restored by AA model (f) The image restored by NLTV method (g) The restored image by BM3D method (h) The restored image by NLTV using AL method (i) The restored image by proposed method.

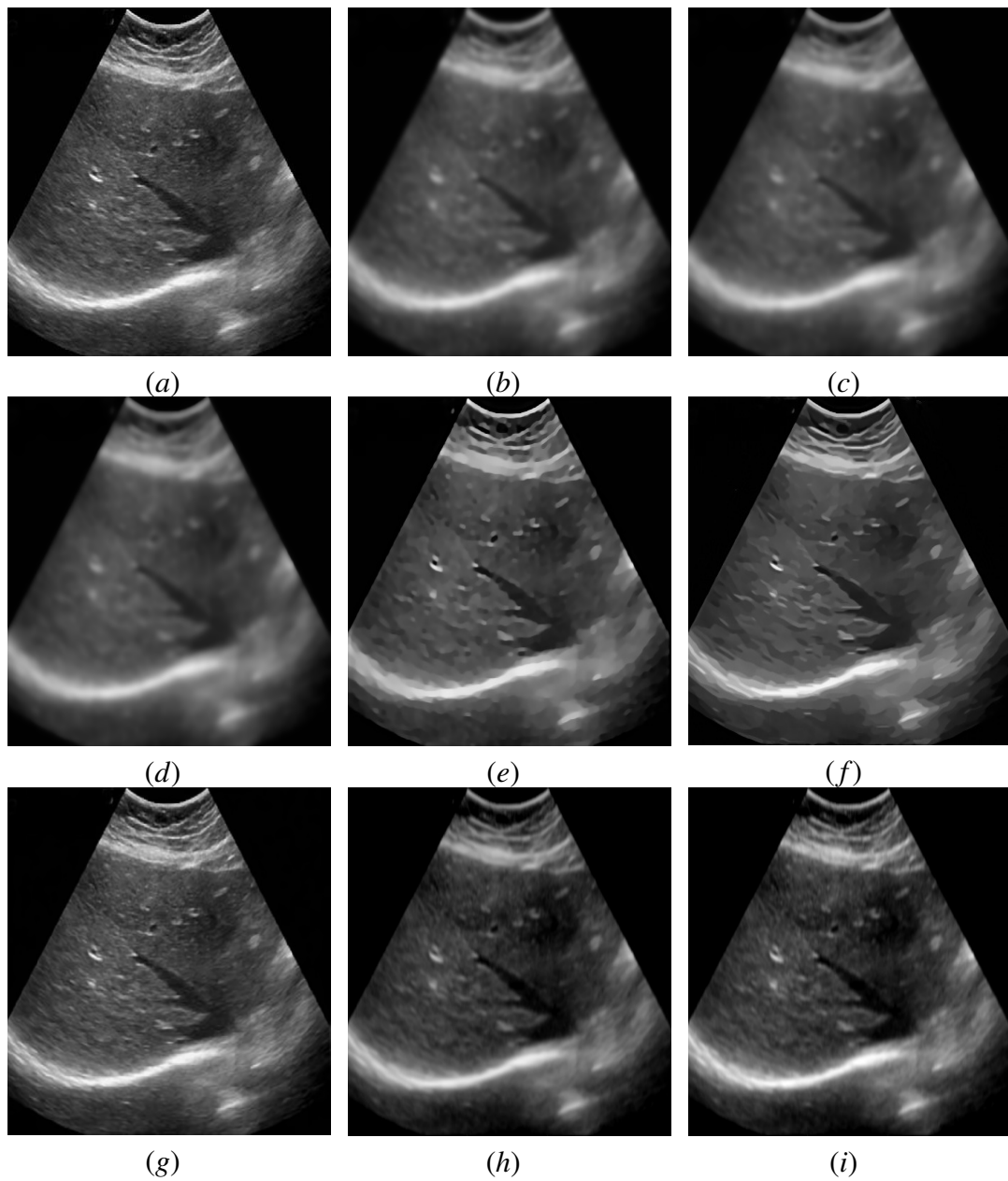


Figure 3.6 (a) Real and noisy hepatic vein image (b) Image restored by SRAD (c) The image restored by DPAD (d) The image restored by OSRAD (e) The image restored by AA model (f) The image restored by NLTV method (g) The restored image by BM3D method (h) The restored image by NLTV using AL method (i) The restored image by proposed method

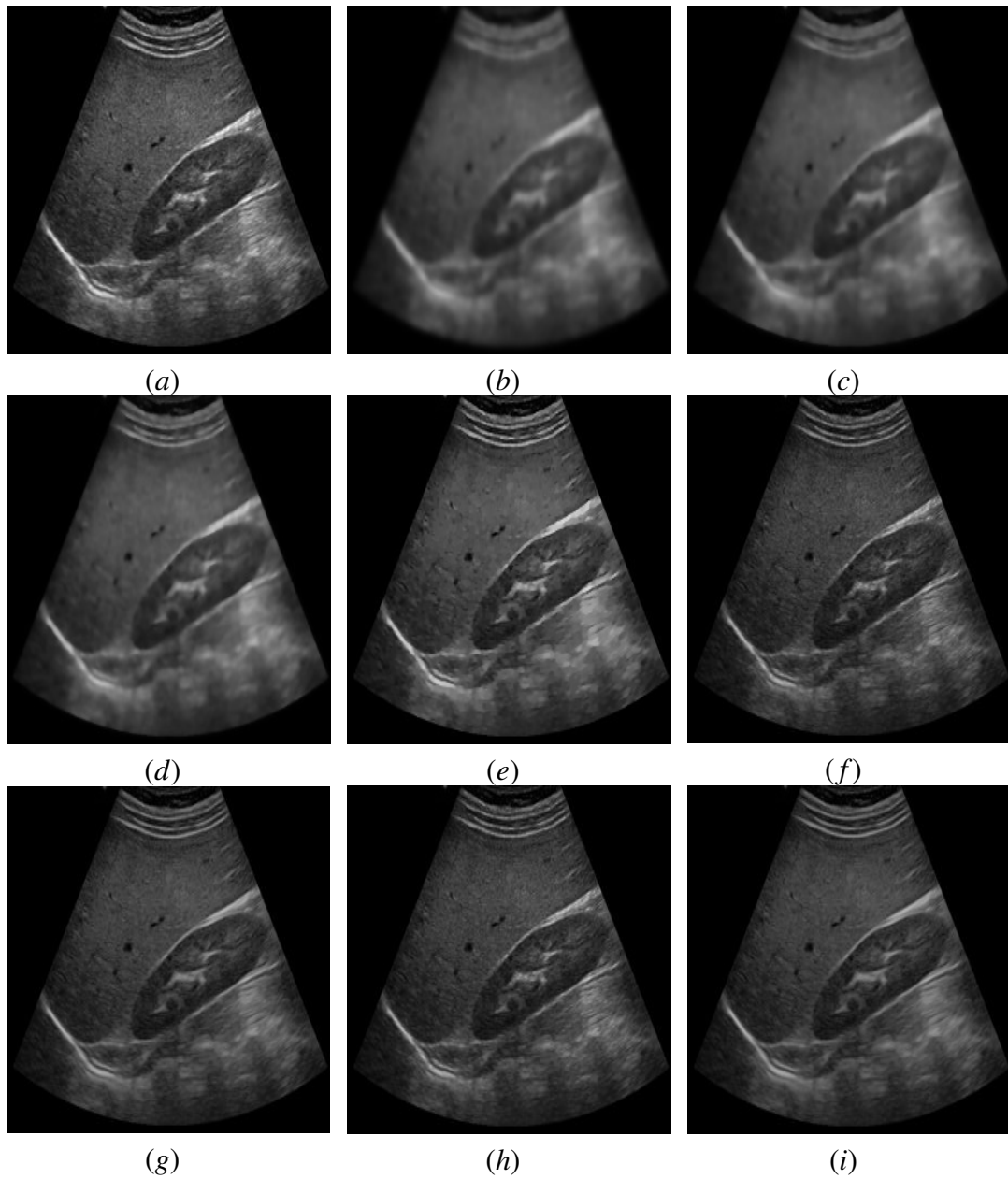


Figure 3.7 (a) Original Kidney image (b) The restored image by SRAD method (c) The restored image by DPAD method (d) The restored image by OSRAD method (e) The restored image by AA method (f) The restored image by NLTV method (g) The restored image by BM3D method (h) The restored image by NLTV using AL method (i) The restored image by proposed method

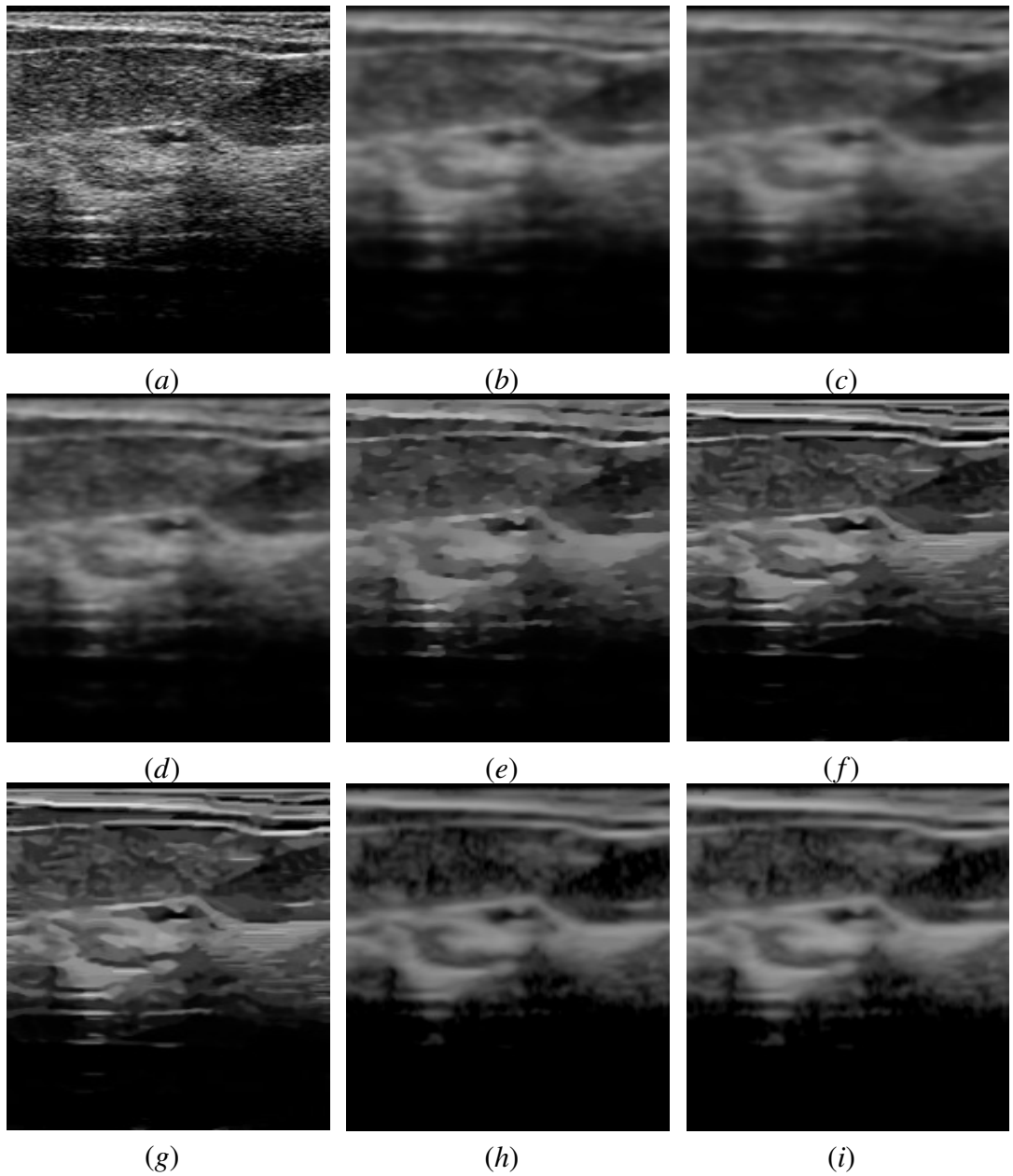
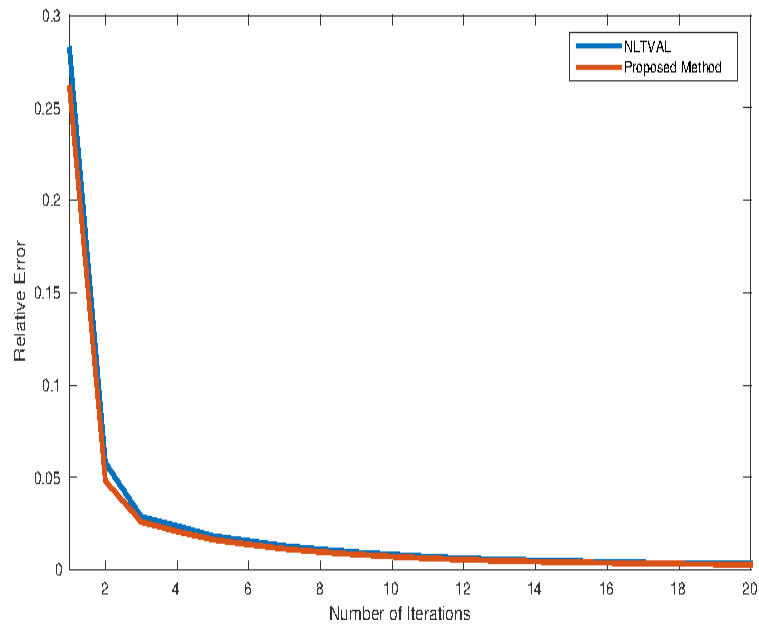
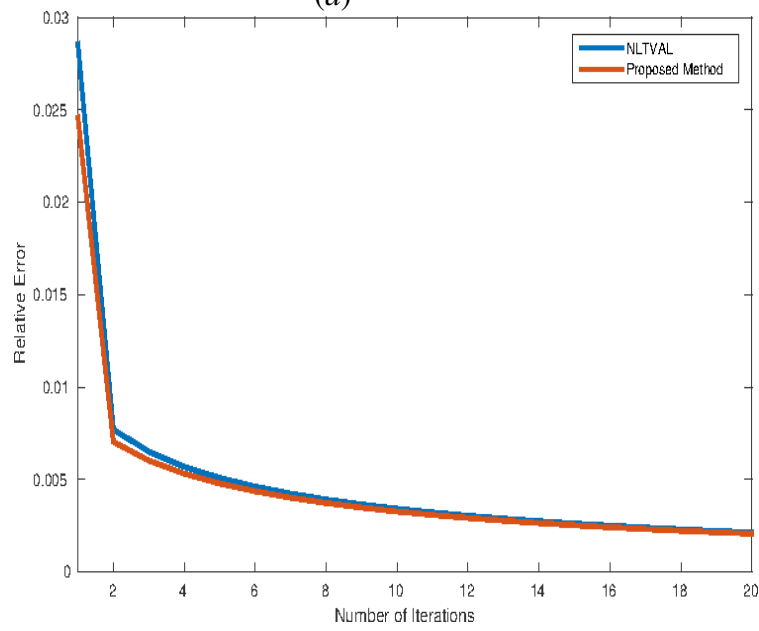


Figure 3.8 (a) Original noisy women breast image (b) The restored image by SRAD method (c) The restored image by DPAD method (d) The restored image by OSRAD method (e) The restored image by AA method (f) The restored image by NLTV method (g) The restored image by BM3D method (h) The restored image by NLTV using AL method (i) The restored image by proposed method



(a)



(b)

Figure 3.9 Relative Error $\frac{\|\mathbf{u}_{n+1} - \mathbf{u}_n\|}{\|\mathbf{u}_{n+1}\|}$ plotted for the images: SAR and US liver image, respectively (the relative error follows a similar pattern for other images as well).

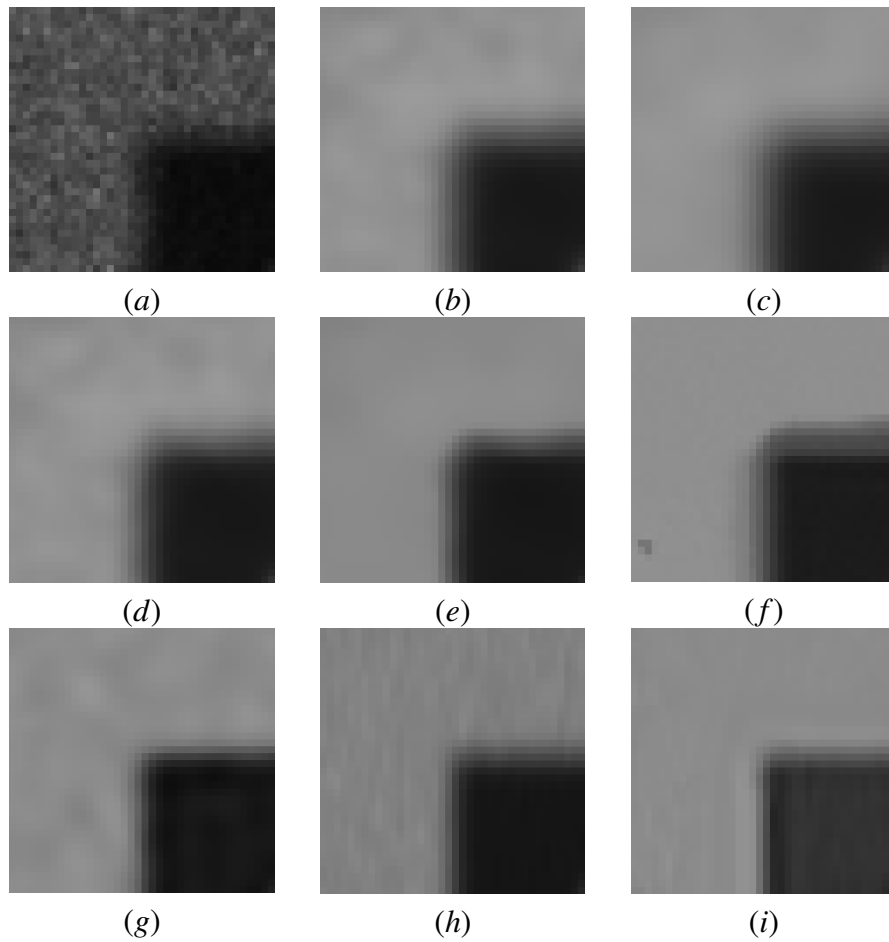


Figure 3.10 (a) Speckled and blurred phantom enlarged portion of the image [Gamma noise variance: 0.1 and Blur kernel size: 2] (b) The restored image by SRAD method (c) The restored image by DPAD method (d) The restored image by OSRAD method (e) The restored image by AA method (f) The restored image by NLTV method (g) The restored image by BM3D method (h) The restored image by NLTV using AL method (i) The restored image by proposed method.

Chapter 4

SPECKLE REDUCING LEVEL-SET APPROACH

4.1 Introduction

In much US, laser and sonar imagery the acquired data is found to be corrupted by granules commonly known as speckles. In active imaging modalities, images are formed based on the characteristics of the surface on which the signal falls. Depending on the scatter-density (number of scatters per cell) of the wave that hits on the object and reflects, high amplitude signals called speckles are generated. As analyzed in many previous works, the noise distribution of the speckle directly depends on the scatter density of the wave (Goodman, 1976). So in many studies reported in the literature, the speckle intensity is approximated to a Gamma distribution with shape (k) and scale (σ) parameters (Aubert and Aujol, 2008). Here it may be noted that, the PDF for a Gamma distribution is $\Gamma(k, \sigma) = \frac{1}{\Gamma(k)\sigma^k} \mathbf{x}^{k-1} e^{-\frac{\mathbf{x}}{\sigma}}$, where the scalars $k, \sigma > 0$ and $\mathbf{x} \in (0, \infty)$. In SAR imagery a pixel at a given location in the observation plane is formed from superimposition of the magnitude of complex functions. These complex functions are generated from different scattering points on the surface of the object. Subsequently, the amplitude of these complex magnitude functions (depending on the roughness of the surface) gets added with different phase characteristics results in interference of complex patterns superimposed on the pixel of interest. Eventually resulting in high amplitude data-granules called speckles. These speckles in SAR imagery hinder proper interpretation of data and severely affect the analysis phase, readers are invited to refer Goodman (1976) for further details of a speckle formation. Further, the presence of speckles in the acquired signal drastically reduces the probability of target detection in a radar system and also causes the system to lose track of the target. Thus speckle suppression is a subject of major practical interest to scientists and engineers working in the field of satellite and radar data analysis.

A detailed discussion about various despeckling models was done in Chapter 2 of this thesis. In addition to those methods there are some methods specifically designed for SAR images. The state-of-the-art restoration filter is based on the non-local averaging and block-matching 3D transform (BM3D) (K. Dabov and Egiazarian, 2007). BM3D was also proposed for SAR images, which is introduced as a SAR despeckling-version of the BM3D (SAR-BM3D) filter, see (Parrilli et al., 2012). The SAR-BM3D demonstrates good performance in preserving structures but gives poor smoothing results for homogeneous regions. Moreover BM3D based models do not consider the noise distribution as well as the data-correlated nature of the noise. The above discussed methods are primarily based on an additive noise model, where the noise is assumed to be data-independent. However, as observed in many recent works the speckles present in SAR images are found to be data-dependent and they follow multiplicative noise model. Therefore, recently some SAR despeckling methods have been proposed which attempt to transform the multiplicative noise into additive noise based on homomorphic filtering approach (input data is transformed to the log domain, where the multiplicative noise becomes additive), see Amirmazlaghani and Amindavar (2012); Parrilli et al. (2012); Li et al. (2011) for the details. As a relatively new approach, methods based on sparse representation (SR) give good results when dealing with the processing of various natural images (viz. denoising and classification) see Lu et al. (2016). Most of the models described in previous sections do not consider the data-dependent nature of speckle and moreover the distribution of the noise is being neglected while processing the data. This puts a limitation to these models, as the noise distribution eventually affects the restoration process. There are a few models proposed in the literature that duly cares the noise distribution in speckles. For instance in Aubert and Aujol (2008), the authors propose a variational model derived based on the MAP estimate of the noise PDF. This model tunes its data-fidelity based on the MAP estimator. There were some improvements proposed for this model as well, see Jin and Yang (2011) for details.

The remaining sections of this chapter are organized as follows. In the next section a speckle reducing level-set approach is proposed along with its formulations. In the Section 4.3, we highlight the SB formulation for the proposed model. The experimental results and discussions are provided in the Section 4.4.

4.2 Speckle Reducing Level-Set Approach

The Mumford-Shah functional was introduced as a tool for image segmentation in Mumford and Shah (1989). Let Ω be a bounded open subset of \mathbb{R}^2 (the screen) and \mathbf{u}_0 be a bounded measurable function defined on the image (which represents the noisy

image in a matrix format). The functional $J(\mathbf{u}, S)$ where S is a closed subset and \mathbf{u} is the function (which represent the original image matrix) belonging to the Sobolev space (space of differentiable functions) defined by

$$J(\mathbf{u}, S) = \mathcal{H}^{d-1}(S) + \int_{\Omega \setminus S} (\alpha |\nabla \mathbf{u}|^2 + \lambda \|\mathbf{u} - \mathbf{u}_0\|_{L^2}^2) dx dy, \quad (4.1)$$

where the first term $\mathcal{H}^{d-1}(S)$ is the Hausdorff $d - 1$ -dimensional measure of S in \mathbb{R}^2 (here $d > 1$ is a scalar integer), $\lambda > 0$ is a positive scalar regularization parameter, $\alpha \in (0, \infty)$ is a scalar positive constant, $|\cdot|$ denotes the absolute value of the function, L^2 norms of the regularization term and $\Omega \subset \mathbb{R}^2$ is an open and bounded set. Further, without loss of generality let us define $\nabla \mathbf{u}$ as the non-local gradient operator of the image function \mathbf{u} , \mathbf{u}_0 is the observed image, and Δ as the non-local Laplacian operator, readers are invited to refer Gilboa and Osher (2008) for the details of non-local variational formulation. The third term of this functional reduces the deviation of \mathbf{u} from \mathbf{u}_0 , whereas the second term ensures the regularization of the function \mathbf{u} making the variation slow on Ω . Since no regularity is assumed for \mathbf{u} across the singular set S (corresponding to discontinuities/edges in \mathbf{u}), let us hope that for such a minimizer, S is the hyper-surface across which \mathbf{u}_0 has great variations. The numerical evaluation of this functional is not easy in its present form due to the presence of the term containing Hausdorff measure. In Ambrosio and Tortorelli (1990) (AT) the authors proposed an approximation to this functional by introducing an extra variable \mathbf{v} which eventually approaches the solution of \mathbf{u} .

$$A_\rho(\mathbf{u}, \mathbf{v}) = \min_{\mathbf{u}, \mathbf{v}} \left\{ \int_{\Omega} \left[\rho |\nabla \mathbf{v}|^2 + \alpha \left(\mathbf{v}^2 |\nabla \mathbf{u}|^2 + \frac{(\mathbf{v} - 1)^2}{4\alpha\rho} \right) + \lambda \|\mathbf{u} - \mathbf{u}_0\|_{L^2}^2 \right] dx dy \right\}, \quad (4.2)$$

where $\rho > 0$ is a fixed scalar parameter and \mathbf{v} is a smooth edge indicator (i.e. $\mathbf{v} \rightarrow 0$ when $|\nabla \mathbf{u}| \rightarrow \infty$). The other symbols are as defined earlier. Further the authors have proved that $A_\rho(\mathbf{u}, \mathbf{v})$ admits a solution and $A_\rho(\mathbf{u}, \mathbf{v})$ converges to Mumford-Shah functional in (4.1) as $\rho \rightarrow 0$. The Euler equation associated with the above expression is

$$\begin{cases} \lambda(\mathbf{u} - \mathbf{u}_0) - \alpha \nabla(\mathbf{v}^2 \nabla \mathbf{u}) & = 0 \\ -\Delta \mathbf{v} + \frac{1+4\alpha\rho|\nabla \mathbf{u}|^2}{4\rho^2} \left(\mathbf{v} - \frac{1}{1+4\alpha\rho|\nabla \mathbf{u}|^2} \right) & = 0. \end{cases}$$

To reduce the complexity of the solution involving two parameters (\mathbf{u} and \mathbf{v}), a modified version of this model is proposed, which eliminates the parameter \mathbf{v} and make the functional depend only on \mathbf{u} (the original image function). The modification amounts

to

$$G_\sigma(\mathbf{u}) = \min_{\mathbf{u}} \left\{ \int_{\Omega} \left[\alpha \left[\chi(\mathbf{u})^2 |\nabla \mathbf{u}|^2 + \frac{1}{4\alpha\rho} (\chi(\mathbf{u}) - 1)^2 \right] + \lambda \|\mathbf{u} - \mathbf{u}_0\|_{L^2}^2 \right] dx dy \right\}, \quad (4.3)$$

where

$$\chi(\mathbf{u}) = \frac{1}{1 + 4\alpha\rho |\nabla \mathbf{u}|^2}. \quad (4.4)$$

This model assumes a data-independent additive noise as one can observe from the data fidelity term. The constraint $\|\mathbf{u} - \mathbf{u}_0\|_{L^2}^2$ denotes the squared error in the approximation of \mathbf{u} ($\|\mathbf{u}\|_{L^2}^2 \triangleq \int_{\Omega} \mathbf{u}^2 dx dy$ denotes the square of the L^2 norm of the functional \mathbf{u}). This is derived based on the assumption that the noise is additive and the model appears $\mathbf{u}_0 = \mathbf{u} + \mathbf{n}$, where \mathbf{n} is the data-independent additive noise. As evident from the literature (from central limit theorem) when the sample size of the noise is sufficiently large the noise follows a Gaussian distribution (under the assumption that the noise pixels are derived from independent sources). However, as already pointed out earlier in this work, speckles are data-dependent noise which follows a Gamma law. Moreover, speckle noise is generally observed to be multiplicative. Incorporating this assumption as a constraint to the regularization functional and deriving the MAP for the Gamma distribution yields (see Aubert and Aujol (2008) for the details) :

$$G_\sigma(\mathbf{u}) = \min_{\mathbf{u}} \left\{ \int_{\Omega} \left[\alpha \phi(\mathbf{u}) + \lambda \left(\ln(\mathbf{u}) + \frac{\mathbf{u}_0}{\mathbf{u}} \right) \right] dx dy \right\}, \quad (4.5)$$

where $\phi(\mathbf{u})$ is the regularization prior defined as $\phi(\mathbf{u}) = \chi(\mathbf{u})^2 |\nabla \mathbf{u}|^2 + \frac{1}{4\alpha\rho} (\chi(\mathbf{u}) - 1)^2$. Considering a linear blurring artefact in the acquired image, one can modify the above expression as

$$G_\sigma(\mathbf{u}) = \min_{\mathbf{u}} \left\{ \int_{\Omega} \left[\alpha \phi(\mathbf{u}) + \lambda \left(\ln(\mathbf{K}\mathbf{u}) + \frac{\mathbf{u}_0}{\mathbf{K}\mathbf{u}} \right) \right] dx dy \right\}, \quad (4.6)$$

where \mathbf{K} is a bounded linear operator corresponding to a linear blur. One usual way to solve the above optimization problem is using the explicit scheme by converting the unconstrained problem to a non-linear PDE with the help of the Euler-Lagrange (E-L) formulation (E-L derivative for a functional $F(x, \mathbf{u}, \mathbf{u}')$ is $\frac{\partial F}{\partial \mathbf{u}} - \frac{d}{dx} \left(\frac{\partial F}{\partial \mathbf{u}'} \right) = 0$). The Euler derivative of the above functional using artificial time marching scheme is written as

$$-\alpha \nabla \cdot \left(\frac{\xi'(|\nabla \mathbf{u}|) \nabla \mathbf{u}}{|\nabla \mathbf{u}|} \right) + \lambda \mathbf{K}^* \left(\frac{\mathbf{K}\mathbf{u} - \mathbf{u}_0}{(\mathbf{K}\mathbf{u})^2} \right) = 0, \quad (4.7)$$

where $\xi(\mathbf{z}) = \frac{\mathbf{z}^p}{1+4\alpha\rho\mathbf{z}^p}$, here \mathbf{z} denotes $|\nabla\mathbf{u}|$ and \mathbf{K}^* is the adjoint of \mathbf{K} . Now let us write the above expression in an anisotropic manner using the explicit scheme as

$$-\alpha \left(\frac{\xi'(|\nabla\mathbf{u}|)}{|\nabla\mathbf{u}|} U_T + \xi''(|\nabla\mathbf{u}|) U_N \right) + \lambda \mathbf{K}^* \left(\frac{\mathbf{K}\mathbf{u} - \mathbf{u}_0}{(\mathbf{K}\mathbf{u})^2} \right) = 0, \quad (4.8)$$

where the second-order derivatives: tangent (U_T) and normal (U_N) to the level-curve are written respectively, as

$$U_T = \frac{1}{|\nabla\mathbf{u}|^2} (\mathbf{u}_x^2 \mathbf{u}_{yy} - 2\mathbf{u}_x \mathbf{u}_y \mathbf{u}_{xy} + \mathbf{u}_y^2 \mathbf{u}_{xx}) \quad (4.9)$$

and

$$U_N = \frac{1}{|\nabla\mathbf{u}|^2} (\mathbf{u}_x^2 \mathbf{u}_{xx} + 2\mathbf{u}_x \mathbf{u}_y \mathbf{u}_{xy} + \mathbf{u}_y^2 \mathbf{u}_{yy}), \quad (4.10)$$

where \mathbf{u}_x , \mathbf{u}_y and \mathbf{u}_{xx} are the first-order derivatives along x , y and second-order derivative along x , respectively. The first and second derivatives of the function $\xi(\cdot)$ are

$$\xi'(|\nabla\mathbf{u}|) = \frac{2|\nabla\mathbf{u}|}{(1 + (4\alpha\rho|\nabla\mathbf{u}|^2))^2} \quad (4.11)$$

and

$$\xi''(|\nabla\mathbf{u}|) = \frac{2(1 - 12\alpha\rho|\nabla\mathbf{u}|^2)}{(1 + (4\alpha\rho|\nabla\mathbf{u}|^2))^3}, \quad (4.12)$$

respectively. One of the major drawbacks of the explicit time marching scheme is its slow convergence rate. Moreover, the convergence heavily depends on the regularization parameter and the time step. These setbacks due to slow convergence and parameter dependency can be addressed to an extent using the fast numerical schemes such as SB scheme (Goldstein et al., 2010). In the following section, we detail the fast numerical scheme followed for solving the model.

4.3 Split-Bregman Iterative Scheme for the Model

We perform SB iteration scheme to solve the model proposed in the previous section. The proposed model under the SB scheme converges faster and the convergence is insensitive to the parameters of the functional, see Goldstein et al. (2010) for the details. In this section, the SB formulation of the proposed model is highlighted. Now let us

write the objective function for the proposed model:

$$\begin{aligned} \min_{\mathbf{u}} \int_{\Omega} \left\{ \alpha \left(\left(\frac{1}{1+4\alpha\rho|\nabla\mathbf{u}|^2} \right)^2 |\nabla\mathbf{u}|^2 + \frac{1}{4\alpha\rho} \left(\frac{1}{1+4\alpha\rho|\nabla\mathbf{u}|^2} - 1 \right)^2 \right) \right. \\ \left. + \lambda \left(\ln(\mathbf{K}\mathbf{u}) + \frac{\mathbf{u}_0}{\mathbf{K}\mathbf{u}} \right) \right\} dx dy. \end{aligned} \quad (4.13)$$

In order to solve the above model a new auxiliary variable \mathbf{d} is introduced as follows: i.e. $\mathbf{d} = \nabla\mathbf{u}$ (\mathbf{d} is a vector), so the constraint $\|\mathbf{d} - \nabla\mathbf{u}\|_2^2 = 0$ (squared l^2 norm) needs to be added

$$\begin{aligned} \min_{\mathbf{u}, \mathbf{d}} \int_{\Omega} \left\{ \alpha \left(\left(\frac{1}{1+4\alpha\rho|\mathbf{d}|^2} \right)^2 |\mathbf{d}|^2 + \frac{1}{4\alpha\rho} \left(\frac{1}{1+4\alpha\rho|\mathbf{d}|^2} - 1 \right)^2 \right) \right. \\ \left. + \lambda \left(\ln(\mathbf{K}\mathbf{u}) + \frac{\mathbf{u}_0}{\mathbf{K}\mathbf{u}} \right) \right\} dx dy, \\ \text{subject to } \|\mathbf{d} - \nabla\mathbf{u}\| = 0. \end{aligned} \quad (4.14)$$

For solving the above problem one has to convert it into an unconstrained optimization problem (using Lagrange formulation) as follows:

$$\begin{aligned} \min_{\mathbf{u}, \mathbf{d}} \int_{\Omega} \left\{ \alpha \left(\left(\frac{1}{1+4\alpha\rho|\mathbf{d}|^2} \right)^2 |\mathbf{d}|^2 + \frac{1}{4\alpha\rho} \left(\frac{1}{1+4\alpha\rho|\mathbf{d}|^2} - 1 \right)^2 \right) \right. \\ \left. + \lambda \left(\ln(\mathbf{K}\mathbf{u}) + \frac{\mathbf{u}_0}{\mathbf{K}\mathbf{u}} \right) + \frac{\beta}{2} \|\mathbf{d} - \nabla\mathbf{u}\|_2^2 \right\} dx dy, \end{aligned} \quad (4.15)$$

where β is a positive constant. Using SB iterative algorithm for solving the above problem gives two subproblems; \mathbf{u} subproblem and \mathbf{d} subproblem, i.e.,:

$$\mathbf{u}^{k+1} = \arg \min_{\mathbf{u}} \lambda \left(\ln(\mathbf{K}\mathbf{u}) + \frac{\mathbf{u}_0}{\mathbf{K}\mathbf{u}} \right) + \frac{\beta}{2} \|\nabla\mathbf{u} - \mathbf{d}^k + \mathbf{b}^k\|_2^2 \quad (4.16)$$

and

$$\begin{aligned} \mathbf{d}^{k+1} = \arg \min_{\mathbf{d}} \left\{ \alpha \left[\left(\frac{1}{1+4\alpha\rho|\mathbf{d}|^2} \right)^2 |\mathbf{d}|^2 + \frac{1}{4\alpha\rho} \left(\frac{1}{1+4\alpha\rho|\mathbf{d}|^2} - 1 \right)^2 \right] \right. \\ \left. + \frac{\beta}{2} \|\mathbf{d} - \nabla\mathbf{u}^{k+1} - \mathbf{b}^k\|_2^2 \right\}, \end{aligned} \quad (4.17)$$

with the update expression for \mathbf{b} (\mathbf{b} is a vector) as

$$\mathbf{b}^{k+1} = \mathbf{b}^k + (\nabla \mathbf{u}^{k+1} - \mathbf{d}^{k+1}). \quad (4.18)$$

Now let us derive an unconstrained SB iterative algorithm. Given $\mathbf{u}^0 = 0$, and $\mathbf{d}^0 = \mathbf{b}^0 = 0$

$$\begin{cases} \mathbf{u}^{k+1} = \arg \min_{\mathbf{u}} \lambda \left(\ln(\mathbf{K}\mathbf{u}) + \frac{\mathbf{u}_0}{\mathbf{K}\mathbf{u}} \right) + \frac{\beta}{2} \|\nabla \mathbf{u} - \mathbf{d}^k + \mathbf{b}^k\|_2^2 \\ \mathbf{d}^{k+1} = \arg \min_{\mathbf{d}} \alpha \left[\left(\frac{1}{1+4\alpha\rho|\mathbf{d}|^2} \right)^2 |\mathbf{d}|^2 + \frac{1}{4\alpha\rho} \left(\frac{1}{1+4\alpha\rho|\mathbf{d}|^2} - 1 \right)^2 \right] + \frac{\beta}{2} \|\mathbf{d} - \nabla \mathbf{u}^{k+1} - \mathbf{b}^k\|_2^2 \\ \mathbf{b}^{k+1} = \mathbf{b}^k + (\nabla \mathbf{u}^{k+1} - \mathbf{d}^{k+1}). \end{cases}$$

The \mathbf{u} subproblem is solved as follows

$$\mathbf{u}^{k+1} = \mathcal{F}^{-1} \left[\frac{\mathcal{F}[\lambda \mathbf{K}^* \mathbf{u}_0 + \beta (\mathbf{K}\mathbf{u})^2 \operatorname{div}(\mathbf{b} - \mathbf{d}) + \beta (\mathbf{K}\mathbf{u})^2 \Sigma(\mathbf{w}(x, y) \mathbf{u})]}{\lambda |\mathcal{F}[\mathbf{K}]|^2 + (\mathbf{K}\mathbf{u})^2 \beta \Sigma \mathbf{w}(x, y)} \right], \quad (4.19)$$

where \mathbf{K}^* is the adjoint of the operator \mathbf{K} , $\nabla^* = -\operatorname{div}$ represents the adjoint of ∇ , $\Delta = -\nabla^* \nabla$ and $\Delta \mathbf{u} = \Sigma(\mathbf{u}(y) - \mathbf{u}(x)) \mathbf{w}(x, y)$. Here $\mathbf{w}(x, y)$ is the weight function (matrix) derived from Buades et al. (2005). Further, the \mathbf{d} subproblem can be solved as follows

$$\begin{aligned} \mathbf{d}^{k+1} = \alpha \left[\left(\frac{1}{1+4\alpha\rho|\mathbf{d}|^2} \right)^2 |\mathbf{d}|^2 + \frac{1}{4\alpha\rho} \left(\frac{1}{1+4\alpha\rho|\mathbf{d}|^2} - 1 \right)^2 \right] \\ + \frac{\beta}{2} \|\mathbf{d} - \nabla \mathbf{u}^{k+1} - \mathbf{b}^k\|_2^2, \end{aligned} \quad (4.20)$$

or

$$\mathbf{d}^{k+1} = \alpha \left(\frac{\xi'(|\mathbf{d}|)}{|\mathbf{d}|} \right) U_T + \alpha \xi''(|\mathbf{d}|) U_N + \beta (\mathbf{d} - \nabla \mathbf{u} - \mathbf{b}), \quad (4.21)$$

where ξ' and ξ'' are already defined in (4.11) and (4.12), respectively. Further, the definitions for U_T and U_N are found in (4.9) and (4.10), respectively. The parameter λ is updated as described in Appendix B.4.

4.4 Experimental Results

In this research the intensity images are considered (images represented as intensity values) throughout our discussion, however the method can be applied to amplitude images by appropriately scaling them. As a primary step, it is required to prove that the speckle noise distribution in the input data follows a Gamma law. To testify this argu-

ment, homogeneous intensity regions were extracted from the input noisy SAR image shown in Figure 4.1. These homogeneous regions are selected such that the variance within these regions are mainly due to the speckles. Next, we evaluate the histogram of the pixels in the extracted regions and analyze the PDF. Further, the parameters (scale and shape) were estimated assuming a Gamma distribution for each of the regions of interest and Gamma PDF (curves) were plotted with these estimated parameters. Finally, it is confirmed that the PDF (curves) generated from the histograms of the input noisy regions (extracted from the noisy image) closely resembles with the PDF (curves) generated assuming the Gamma distribution with the estimated parameters. The unbiased estimators for scale and shape are

$$\sigma = \frac{n}{n-1} \frac{1}{n^2} (n \sum \mathbf{x}_i \ln(\mathbf{x}_i) - \sum \ln(\mathbf{x}_i) \sum \mathbf{x}_i) \quad (4.22)$$

(where n is the size of the sample and \mathbf{x}_i are the random samples selected from the population) and

$$k^{-1} = \frac{n}{n-1} \frac{n \sum \mathbf{x}_i \ln(\mathbf{x}_i) - \sum \ln(\mathbf{x}_i) \sum \mathbf{x}_i}{n \sum \mathbf{x}_i}, \quad (4.23)$$

respectively. Figure 4.1 shows the result of the experiment. Thus it may be confirmed that the noise distribution is more likely to follow a Gamma law. A further quantitative analysis is performed based on Kullback Leibler (KL) divergence and Jensen Shannon (JS) divergence. KL/JS divergence is an indicative measure of the divergence of two distributions. The KL divergence for two distributions P and Q of a continuous random variable is $D_{\text{KL}}(P, Q) = \int_{-\infty}^{\infty} \mathbf{p}(x) \ln \left(\frac{\mathbf{p}(x)}{\mathbf{q}(x)} \right) dx$, here \mathbf{p} and \mathbf{q} are the densities of P and Q respectively. Similarly the JS divergence is defined as $D_{\text{JS}}(P, Q) = \frac{1}{2} D_{\text{KL}}(P, M) + \frac{1}{2} D_{\text{KL}}(Q, M)$, where $M = \frac{1}{2}(P + Q)$. Here the PDF of the noisy data is extracted from the homogeneous intensity regions (selected in the previous step) and then find the KL and JS divergences of these distributions with the corresponding Gamma distributions generated from the parameters estimated from the region of interest (ROI). The KL and JS divergences for each of these regions are evaluated and tabulated in Table 4.1. The values are in sync with our assumption that the noise distribution of the speckles categorically follows the Gamma law. The KL/JS divergence values are close to zero for various regions extracted out of the image, which means the PDF of the extracted ROIs are closely aligned with the corresponding Gamma PDFs generated from the parameters. Therefore one can conclude that the noise PDF follow a Gamma law.

Now the input images are considered for testing under various state-of-the-art despeckling filters such as the ISRAD (Sun et al., 2004) (an improved speckle reducing

Table 4.1 KL and JS divergence for different regions shown in Figure 4.1

Region	KL divergence	JS divergence
Red	0.0876	0.0479
Blue	0.0324	0.0161
Green	0.0680	0.0329
Yellow	0.2848	0.1767

anisotropic diffusion), Aubert Aujol Method (Aubert and Aujol, 2008), BM3D model for SAR images (K. Dabov and Egiazarian, 2007), PPB method (Deledalle et al., 2009) (The PPB filter uses 7×7 patches and 21×21 search windows, the other details are found in Deledalle et al. (2009)) and FANS algorithm in Cozzolino et al. (2014) (The FANS filter uses 8×8 blocks, and 39×39 pixels search area; the remaining parameters are set as specified in Cozzolino et al. (2014)) along with the one proposed in this work. For doing so, the original SAR images are obtained which are corrupted by speckles.

To quantify the despeckling process there are various models discussed in the literature, among them the one proposed in Gomez et al. (2017) is being adopted. Before venturing into the quantitative assessments, some of the common estimators used to quality the assessments of despeckling filters used in SAR imaging literature are discussed. The first one among them is the Equal Number of Looks (ENL), which reflects the behavior of the well-known measure: Signal to Noise Ratio (SNR). So higher the ENL value, better the filtering is. However, unlike SNR, ENL does not demand the presence of an original image for its computation. The ENL is defined as $\frac{\mu_s^2}{\sigma_s^2}$, where μ_s and σ_s^2 denote the sample mean and sample variance, respectively. In other words, the ENL is the reciprocal of the squared coefficient of variation (CoV). ENL is evaluated for homogeneous intensity regions in test images. However, detecting homogeneous regions in speckled images is basically challenging. The method proposed in Gomez et al. (2017) is adopted to find the homogeneous region in a speckled neighborhood. The sliding window size (25×25) is used for this purpose and the threshold for detecting the textured regions from the difference of $|\text{ENL}_{\text{ratio}} - \text{ENL}_{\text{noisy}}|$ and $1 - \hat{\mu}$ is set adaptively.

Yet another measure to qualify the despeckling process is the Ratio Images (RI). This measure directly conveys the extent of information loss while despeckling the data. The RI measure is defined as $\frac{\mathbf{u}_0 \mathbf{n}}{\hat{\mathbf{u}}}$, technically it is the ratio of the distorted image to the restored one $\hat{\mathbf{u}}$. For a multiplicative speckle noise, this measure should ideally return only the speckle information. The phantom image (in its original form), its single-look SAR simulation (speckled form) and two multi-look original SAR images are shown in Figure 4.2. The ratio images for various restoration methods applied to a synthetic

phantom image (having four different squares with four different intensity values than its background, it simulates a single-look speckled SAR image) are shown in Figure 4.3 abreast with the corresponding restored versions. An ideal restoration process should retain only speckles in ratio images after the filter operation. As the ratio image corresponding to the proposed strategy retains more speckles and less structures compared to the other models, it literally outperforms its counterparts in terms of this measure. The ratio images along with the restored and original versions of two SAR (multi-look) images are shown in Figures 4.4 and 4.5. From these ratio images and the restored versions of the input images, one can easily conclude the proposed model performs a better despeckling and deblurring compared to the other PDE/Variational models considered in this work. However, it may be noted that FANS algorithm performs better in the bright scatter regions, whereas the overall performance in other (dark and light shaded) areas favours the proposed strategy as evident from the results shown in Figures 4.3, 4.4 and 4.5. The enlarged portion of the Flevoland SAR image is shown in Figure 4.6. A portion of the image filtered using different restoration methods considered in this work is shown here. Among the comparative models the ISRAD is a PDE based model and as already detailed in the experimental section of the previous chapter, the PDE based models eventually result in low resolution images due to piecewise approximation. The next model discussed herein is the BM3D. This model is considered to be the state of the art model for restoring images under data-independent noise. However, its performance is limited in data-correlated noise intervention scenarios. PPB and FANS models are the state of the art models for speckle reduction in SAR imagery. Nevertheless, their performance is pretty similar to non-local variational models. All these issues are considerably addressed in case the proposed model wherein a Bayesian approach based on the noise distribution is devised to improve the quality of reconstruction. These facts are quite evident from the test results shown in Figures 4.3, 4.4 and 4.5 discussed above.

Further quantitative measures based on the first and second order statistics mentioned in Gomez et al. (2017) are also used for comparative study. To this end, a measure denoted using M , which captures the characteristics of both first and second order statistic measures is used. The first order statistic measure combines the ENL and mean estimates to quantify the quality of the remaining speckles. It is defined as

$$r_{\widehat{\text{ENL}}, \hat{\mu}} = \frac{1}{2} \sum_{i=1}^n (r_{\widehat{\text{ENL}}}(i) + r_{\hat{\mu}}(i)), \quad (4.24)$$

$$r_{\widehat{\text{ENL}}}(i) = \frac{|\widehat{\text{ENL}}_{\text{noisy}}(i) - \widehat{\text{ENL}}_{\text{ratio}}(i)|}{\widehat{\text{ENL}}_{\text{noisy}}(i)} \quad (4.25)$$

$$r_{\hat{\mu}} = |1 - \hat{\mu}_{\text{ratio}}(i)|. \quad (4.26)$$

For an ideal despeckling filter this measure should yield zero. The proximity to idealness of a filter under consideration is its closeness to zero in terms of this measure. The ENL, $\hat{\mu}$ and standard deviation evaluated for the synthetic image (for four different regions and the background) are tabulated in Table 4.2. A higher ENL value indicates a better restoration, as noticeable from the table the proposed model is evaluated to have highest ENL for all different regions considered for comparative purpose. The optimal (maximum) values for ENL are highlighted using bold cases in the tabulated format. This in turn highlights the restoration capability of the proposed model in comparison to other models considered in this work. The estimated ENL ($\widehat{\text{ENL}}_{\text{ratio}}$) and mean $\hat{\mu}_{\text{ratio}}$ for the ratio images are close to one for the proposed method as observed for the other methods. The second-order filter is a measure of homogeneity evaluated from the co-occurrence matrix ($\mathbf{p}(i, j)$) and defined as

$$h = \sum_i \sum_j \frac{1}{1 + (i - j)^2} \mathbf{p}(i, j). \quad (4.27)$$

Further, the authors define

$$\delta h = 100|h_0 - \bar{h}_g|/h_0, \quad (4.28)$$

where h_0 and h_g are the means of all values of homogeneity obtained from the original ratio image \mathbf{u}_0 and from the result of randomly permuting all its values \mathbf{u}_g , respectively. There are enough reasons to believe that the probability distribution of the ratio image \mathbf{u} is invariant under random permutations. So h literally captures the geometric information contained in the input image, in other words, if there are no structures in \mathbf{u} , h will not change even after shuffling, but if \mathbf{u} contains structures, then shuffling will tend to destroy them. The value of δh should be minimum for an ideal structure preserving filter.

Finally, the first and second order measures are combined to define a new statistic $M = r_{\widehat{\text{ENL}}, \hat{\mu}} + \delta h$. For a perfect despeckling algorithm this value should ideally be zero and the deviation from zero indicates its magnitude of weakness in despeckling data. The measures: $r_{\widehat{\text{ENL}}, \hat{\mu}}$, δh and M are evaluated for both synthetic and real SAR images (of two different locations: Flevoland and San Francisco) and are tabulated in Tables 4.3, 4.4 and 4.5, respectively. The performance of the proposed model in terms of the measure δh is reflected in the tables for two different images. The optimal values for

δh are highlighted in these tables. In similar lines, the optimal value for the statistic M is highlighted using bold cases. From the highlighted values it is inferred that the proposed model gives optimal (minimum) values for the statistical measure M and δh signifying a better detail preservation and speckle alleviation from the SAR data.

The parameter values chosen for the AA method and the proposed method are given in Table 4.6. From the experimental study, it is observed that the proposed method takes less number of iterations to converge to the solution compared to the iterative models: AA model and ISRAD model. On an average, AA model has taken 450 iterations and ISRAD 470 iterations to converge, whereas the proposed model is taking only 10 iterations. This scenario is well explained by the fast convergence of the split-Bregman iteration scheme in comparison to the explicit schemes. Since the other methods compared here are (viz: BM3D, PPB, FANS) non-iterative models, the results regarding the number of iterations taken by the methods to converge are not provided explicitly.

Table 4.2 Quantitative evaluation of filters for the synthetic image (simulated as single look SAR image)

Simulated SAR data		True	Simulated (Noisy)	ISRAD	BM3D	AA	PPB	FANS	Proposed method
Background	μ	0.0074	0.0071	0.0076	0.0070	0.0071	0.0083	0.0082	0.0075
	s	0.0074	0.0071	0.0013	0.0007	0.0008	0.0017	0.0022	0.0020
	ENL	1	1.01	30.764	27.19	27.649	29.668	13.39	46.712
Top left square	μ	0.0014	0.0013	0.0019	0.0012	0.0014	0.0018	0.0014	0.0014
	s	0.0014	0.0013	0.0002	0.0002	0.0002	0.0003	0.0003	0.0003
	ENL	1	1.01	35.379	31.548	29.55	24.722	14.691	43.976
Top right square	μ	0.029	0.0289	0.0284	0.0276	0.0286	0.0386	0.0332	0.0313
	s	0.029	0.0289	0.0062	0.0052	0.0003	0.0077	0.0082	0.0050
	ENL	1	0.9967	20.922	28.022	30.784	24.649	16.375	31.627
Bottom left square	μ	0.043	0.0426	0.0413	0.0422	0.0425	0.0594	0.050	0.0495
	s	0.043	0.0426	0.0103	0.0118	0.0051	0.0120	0.0115	0.0100
	ENL	1	1.0017	16.046	12.807	29.666	24.539	18.822	31.70
Bottom right square	μ	0.058	0.0578	0.0554	0.0571	0.0575	0.0761	0.0673	0.0605
	s	0.058	0.0578	0.0141	0.0238	0.0095	0.0168	0.0162	0.0145
	ENL	1	1.0156	15.355	15.747	26.329	20.457	17.227	27.636
Ratio image	\overline{ENL}_{ratio}	1	-	1.06544	1.0433	1.0736	1.0534	1.0254	1.0058
	$\hat{\mu}_{ratio}$	1	-	0.9916	0.9995	0.9998	0.9789	0.9892	1.0023

In this work a level-set driven anisotropic diffusion model has been studied to restore SAR images which are generally corrupted with data-correlated speckles following a Gamma law. The experimental demonstrations both visual and numerical ones substantiate the efficient restoration capability of the studied model in comparison to the other state-of-the-art models considered in this work (for comparative study). Both synthetic and real images are exposed to analyze and study the behavior of the model.

Table 4.3 Quantitative evaluation of the second order statistics for the synthetic data, computed on $n = 134$ automatically detected homogeneous areas.

Filter	h_0	h_g	δh	$r_{\widehat{\text{ENL}}, \hat{\mu}}$	M
ISRAD	0.64	0.63	0.9576	30.6763	63.21
BM3D	0.4677	0.4685	0.1734	7.92	12.6327
AA	0.4084	0.4072	0.3091	5.11	18.20
PPB	0.2155	0.2150	0.2428	40.03	32.15
FANS	0.1892	0.1890	0.1532	25.32	20.32
Proposed method	0.7995	0.7995	0.0040	17.6993	9.0483

Table 4.4 Quantitative evaluation of the second order statistics for the real SAR (Flevoland Ratio image) data, computed on $n = 90$ automatically detected homogeneous areas.

Filter	h_0	h_g	δh	$r_{\widehat{\text{ENL}}, \hat{\mu}}$	M
ISRAD	0.4371	0.4404	0.7425	9.3483	41.8002
BM3D	0.6417	0.6436	0.3044	5.0397	17.7406
AA	0.9999	0.9999	0.0006157	22.1969	11.1292
PPB	0.2585	0.2580	0.2231	36.8764	29.5919
FANS	0.2170	0.2168	0.0879	21.66	15.22
Proposed method	0.7995	0.7995	0.0018	17.6993	8.9419

Table 4.5 Quantitative evaluation of the second order statistics for the real SAR (San Francisco bay) data, computed on $n = 45$ automatically detected homogeneous areas.

Filter	h_0	h_g	δh	$r_{\widehat{\text{ENL}}, \hat{\mu}}$	M
ISRAD	0.5780	0.5637	2.5494	158.816	81.8002
BM3D	0.7405	0.7320	1.1594	138.576	77.2602
AA	0.9999	0.9999	0.6157	122.196	75.1292
PPB	0.2613	0.2554	2.3154	171.567	69.5505
FANS	0.2170	0.2168	0.1879	121.656	65.22
Proposed method	0.1986	0.1982	0.1670	174.950	55.8230

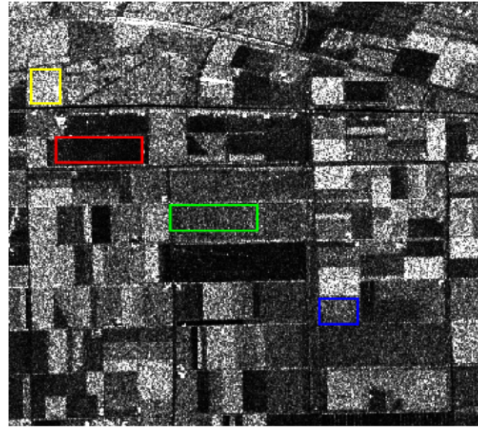
Table 4.6 Different parameter values used for the real test images (Phantom image and AIRSAR image) under various restoration models.

Method Name	λ	ρ	α	β	No. of Iterations
AA	{0.8,0.6}	{0.0001,0.001}	-		{250,200}
Proposed Method	{0.001,0.09}	{0.5,0.5}	{5.8,1.8}	{0.0032,0.2}	{10,10}

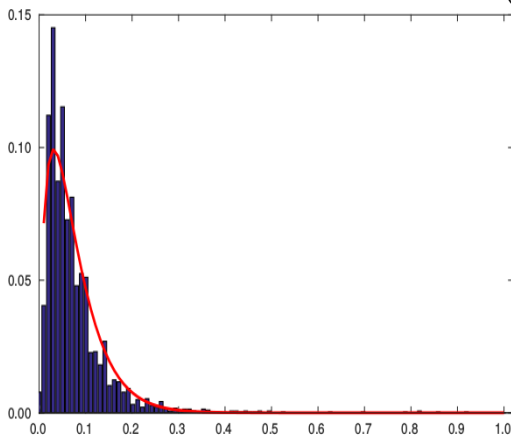
A theoretical analysis has been carried-out to prove the existence of a minimizer of the studied model in this work. A thorough study reveals that the studied model is stable and provides a better restoration in light of statistical study carried-out in this work.

Moreover, the experimental and the theoretical study duly endorses the efficiency of this work.

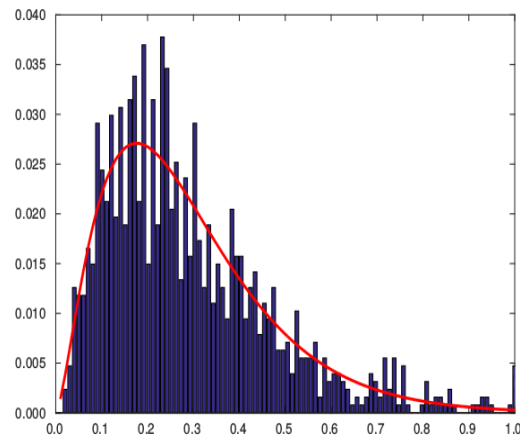
0 1 2 3
km
Centre latitude : 52° 22' 0" N
Centre longitude : 5° 23' 16" E



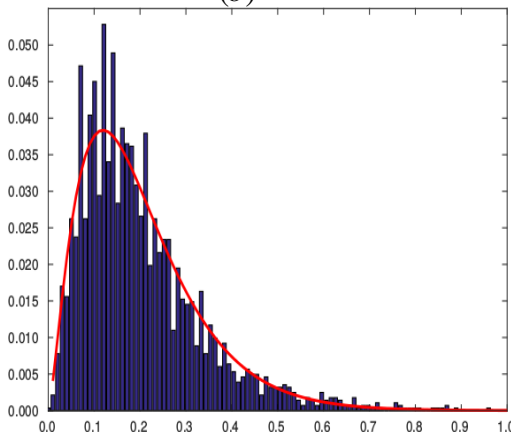
(a)



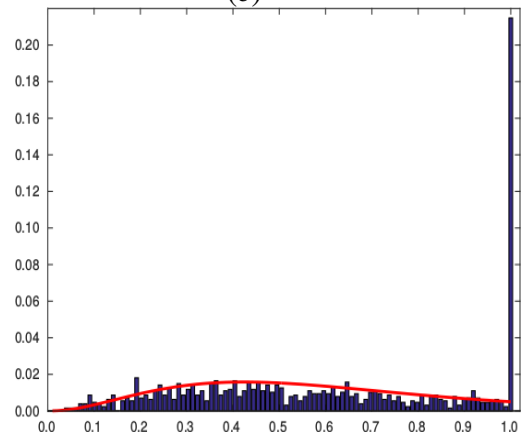
(b)



(c)



(d)



(e)

Figure 4.1 (a) . Original SAR image (showing homogeneous intensity regions in different colours); (b) . The PDF of the intensity distribution of the red coloured region fitted with Gamma using the estimated parameters (Shape 1.0812, Size: 0.0689); (c) . The PDF of the intensity distribution of the blue coloured region fitted with Gamma using the estimated parameters (Shape: 2.4455 Size: 0.0826); (d) . The PDF of the intensity distribution of the green coloured region fitted with Gamma using the estimated parameters (Shape: 2.5470 Size: 0.1138); (e) . The PDF of the intensity distribution of the yellow coloured region fitted with Gamma using the estimated parameters (Shape: 3.2929 Size: 0.1848).

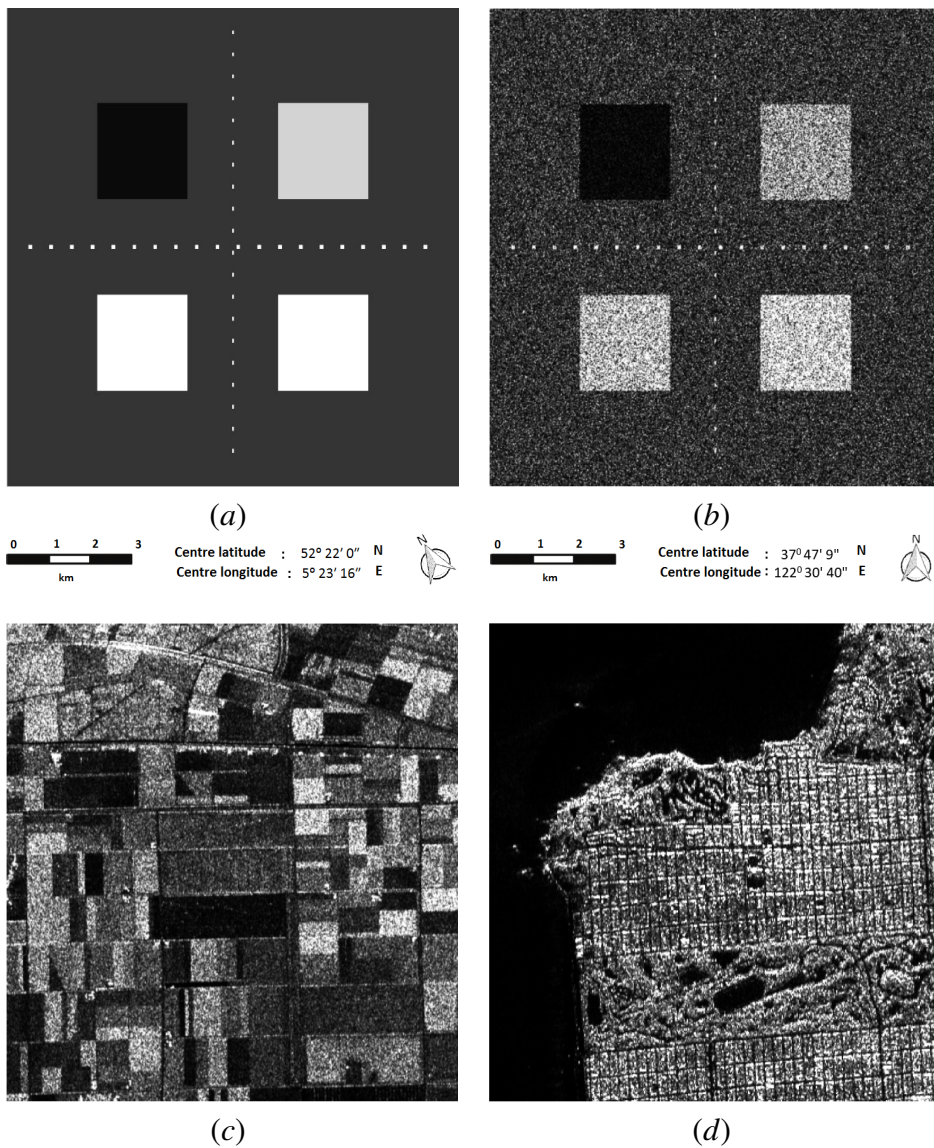


Figure 4.2 (a). Original Phantom image; (b). Single look, Intensity phantom image; (c). Intensity AIRSAR image, HH polarization, three looks; (d). Intensity AIRSAR image, HH polarization, three looks.

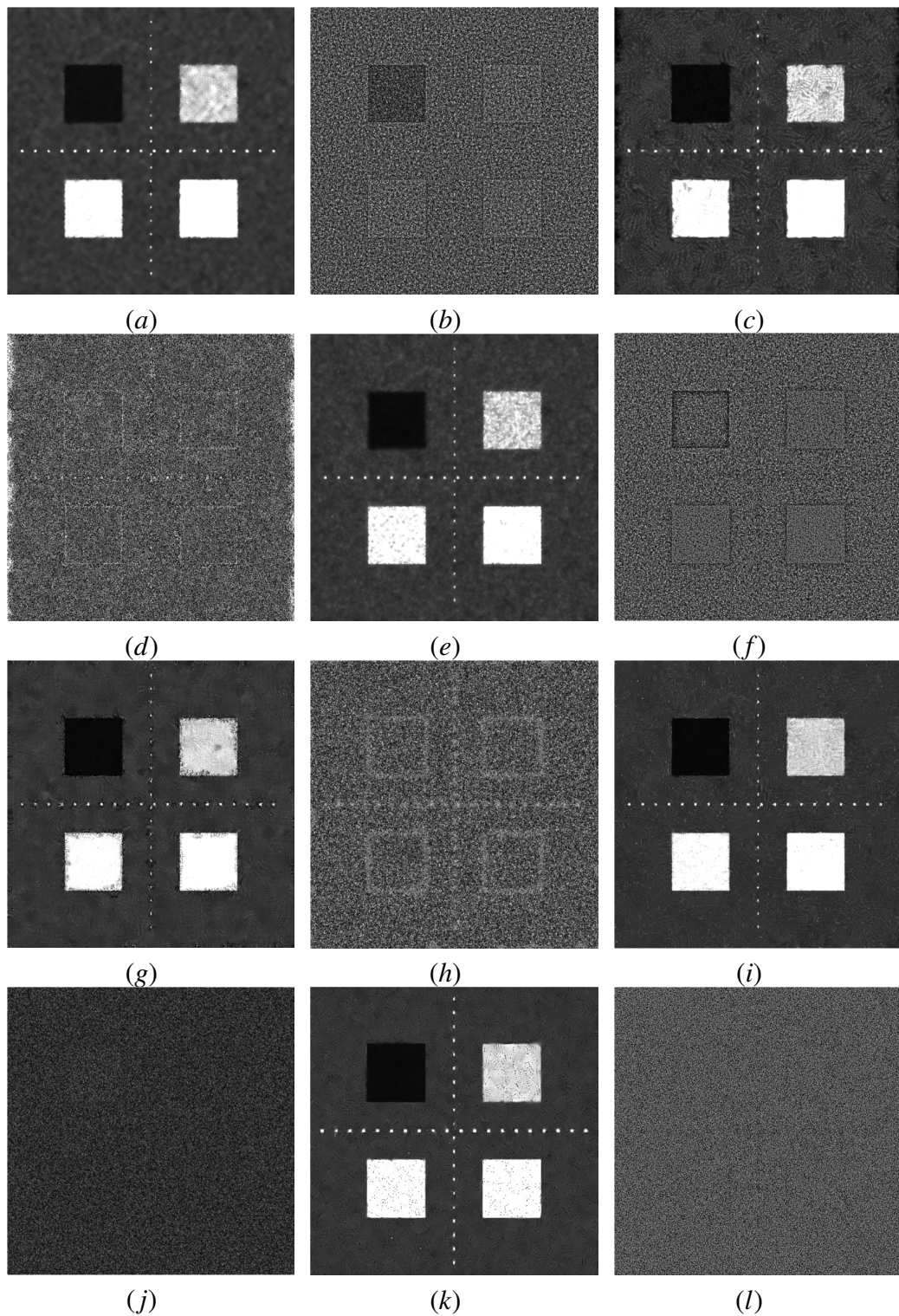


Figure 4.3 Results for the simulated single-look intensity data. (a) . The restored image by ISRAD method; (b) . The Ratio image; (c) . The restored image by BM3D; (d) . The Ratio image; (e) . The restored image by AA method; (f) . The Ratio image; (g) . The restored image by PPB method; (h) . The Ratio image; (i) . The restored image by FANS method; (j) . The Ratio image (k) . The restored image by proposed method; (l) . The Ratio image.

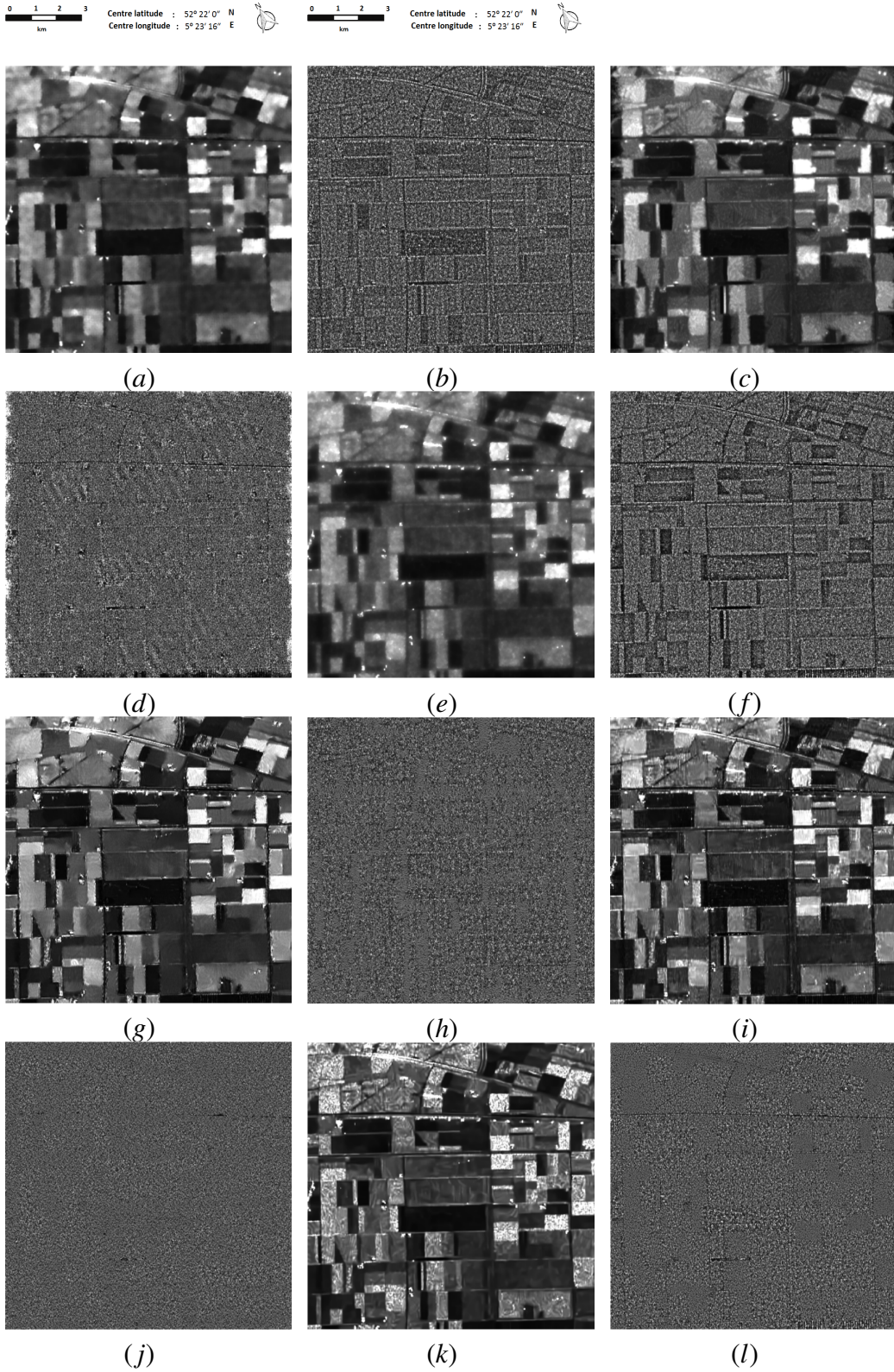


Figure 4.4 Results for the three-look SAR (intensity) image (Flevoland SAR image). (a) . The restored image by ISRAD method; (b) . The Ratio image; (c) . The restored image by BM3D; (d) . The Ratio image; (e) . The restored image by AA method; (f) . The Ratio image; (g) . The restored image by PPB method; (h) . The Ratio image (i) . The restored image by FANS method; (j) . The Ratio image; (k) . The restored image by proposed method; (l) . The Ratio image.

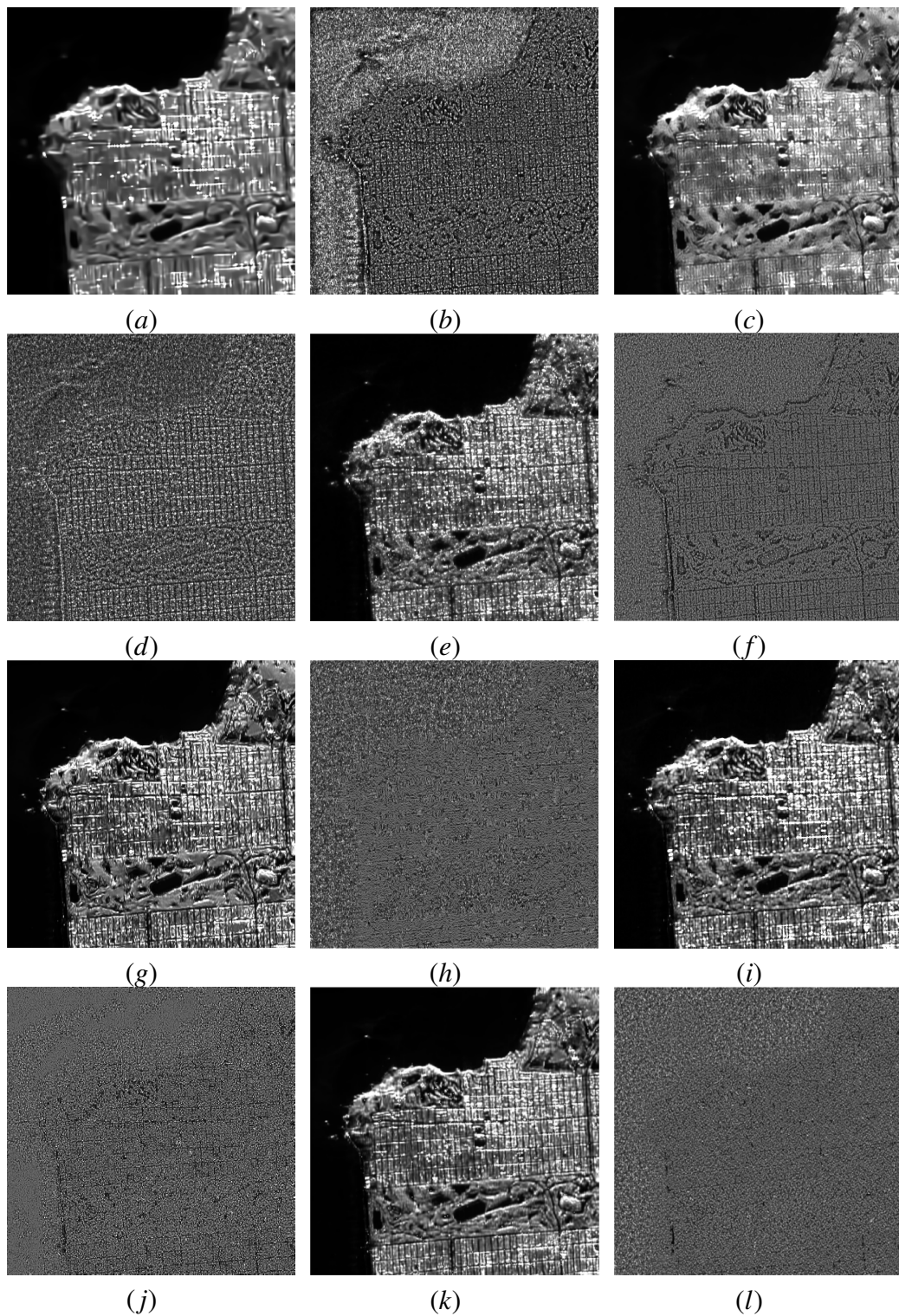


Figure 4.5 Results for the simulated San Francisco bay image. (a) . The restored image by ISRAD method; (b) . The Ratio image; (c) . The restored image by BM3D; (d) . The Ratio image; (e) . The restored image by AA method; (f) . The Ratio image; (g) . The restored image by PPB method; (h) . The Ratio image; (i) . The restored image by FANS method; (j) . The Ratio image (k) . The restored image by proposed method; (l) . The Ratio image.

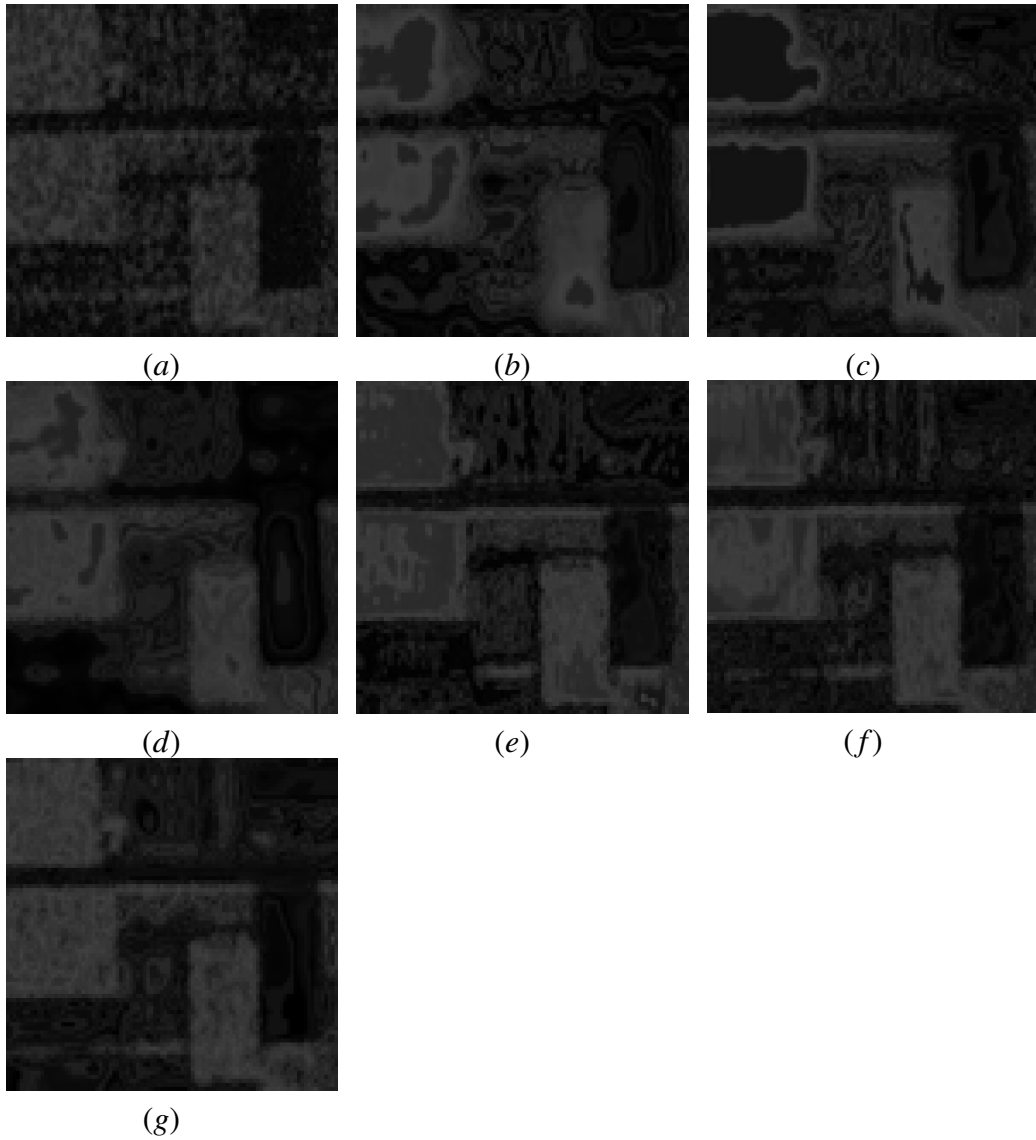


Figure 4.6 Results for the three-look SAR (intensity) enlarged portion of the image (Flevoland SAR image). (a) Original Flevoland zoomed SAR image; (b) . The restored image by ISRAD method; (c) . The restored image by BM3D; (d) . The restored image by AA method; (e) . The restored image by PPB method; (f) . The restored image by FANS method; (g) . The restored image by proposed method.

Chapter 5

NON-LOCAL GRADIENT FIDELITY MODEL FOR MULTIPLICATIVE GAMMA NOISE REMOVAL

5.1 Introduction

The fundamental PDE and Variational models of image restoration have advanced very fast in the last few decades. Starting from the basic nonlinear diffusion model by Perona and Malik (1990) (PM) and total variation (TV) model by Rudin et al. (1992), quite a few variational and PDE models were introduced for image restoration and enhancement as minor modifications of these methods (see Weickert (1997)). Nevertheless, if we analyze these models closely, they have their own merits and issues as discussed in Chapter 1 of the thesis. In the first place, many of these methods assume a data-independent Gaussian distributed noise model. The degradation model assumed in some of these works follow:

$$\mathbf{u}_0 = \mathbf{u} + \mathbf{n}, \quad (5.1)$$

where \mathbf{u} stands for the original clean image and \mathbf{u}_0 is the noisy observed image and \mathbf{n} is Gaussian distributed. As detailed in the Chapter 1, it makes sense to note that the Gaussian-distributed noise assumption in these models puts a limit to their applications as most of the real-time imaging modalities yield non-Gaussian noise distributions.

The main focus of this Chapter is to provide an elegant solution to piecewise linear approximation problem of the second order diffusion models proposed for despeckling images. The piecewise linear approximation results in spurious edges during the diffusion process, which hinders the further analysis of the data. Though, the fourth order diffusion models can address this issue to a considerable extent, they tend to smoothen the data causing severe damages to the sharp edges in images.

There are some models proposed in the literature to deal with the piecewise linear approximation (stair-case formation) of the second order anisotropic diffusion models, see Jidesh and Bini (2013) and Yu et al. (2011), for the details. The staircase formation is addressed using a convex combination of TV and L^2 norms in Jidesh (2014), a complex diffusion driven despeckling in Jidesh and Bini (2013) and an adaptive p -laplacian filter in Wei and Xu (2009). Gradient fidelity based restoration is yet another relevant method for image restoration, which considerably alleviates the linear approximation of the second order models. The energy formulation of gradient fidelity model proposed in Lixin and Deshen (2008) is

$$E(\mathbf{u}) = \int_{\Omega} \lambda (\mathbf{u} - \mathbf{u}_0)^2 + \alpha (\|\nabla \mathbf{u} - \nabla(G_{\sigma} * \mathbf{u}_0)\|)^2 dx dy, \quad (5.2)$$

where

$$G_{\sigma}(x, y) = \frac{1}{2\pi\sigma^2} e^{-(x^2+y^2)/2\sigma^2}, \quad (5.3)$$

λ and α are the parameters to control the fidelity terms, Ω is the region of image support and $*$ denotes the linear convolution. It is not difficult to notice that in the constant intensity regions, when the piecewise constant patches are formed the gradient fidelity term tries to reduce the intensity variations by minimizing the difference norm of gradient and its smoothed value, subsequently reducing the staircase formation. In Xiao et al. (2010) the authors have plugged in the Perona and Malik (1990) and Rudin et al. (1992) the diffusion terms along with the gradient fidelity to perform a second order nonlinear anisotropic diffusion along with the gradient fidelity. The diffusion equation for TV based gradient fidelity is:

$$\mathbf{u}_t = \nabla \cdot \left(\frac{\nabla \mathbf{u}}{|\nabla \mathbf{u}|} \right) + \alpha (\Delta \mathbf{u} - G_{\sigma} * \Delta(p_{\lambda} \mathbf{u}_0) + \lambda (\mathbf{u} - \mathbf{u}_0)), \quad (5.4)$$

where $\Delta \mathbf{u} - G_{\sigma} * \Delta(p_{\lambda} \mathbf{u}_0)$ is called curvelet shrinkage-based gradient data-fidelity term and is designed to force the gradient of \mathbf{u} to be close to $\Delta(p_{\lambda} \mathbf{u}_0)$ the gradient estimation and to alleviate the staircase effect. Furthermore, authors incorporate a pixel-based controlling parameter $\alpha(x, y)$ (unlike the scalar value) to preserve the textured regions more effectively. The locally adaptive gradient fidelity term helps to retain finer details and textures by locally controlling the magnitude of diffusion.

In Liu et al. (2014) the authors proposed a novel non-convex gradient fidelity functional for restoring images from their blurred observations. The model takes the following form

$$\min_{\mathbf{u}} \left\{ \|\mathbf{u} - \mathbf{u}_0\|_{L^2}^2 + \lambda \|\ |\nabla \mathbf{u} - \nabla \mathbf{u}_0|^{\alpha-1} \otimes |\nabla \mathbf{u} - \nabla \mathbf{u}_0| \|_{L^2}^2 \right\}, \quad (5.5)$$

where $\|\cdot\|_{L^2}^2$ denotes the squared L^2 norm, \otimes is the point-wise multiplication operator and $\alpha \in [0 - 1]$ is the power of the weighing term $|\nabla \mathbf{u} - \nabla \mathbf{u}_0|$. When $\alpha = 1$, the model transforms to an ordinary gradient fidelity model.

Majority of the models discussed above were designed for additive data-independent noise. However, there are some other models introduced for restoring images corrupted by data-dependent Gamma and Poisson noise distributions as well, see Aubert and Aujol (2008) and Le et al. (2007), respectively for the details. In these models the TV regularization term is fitted along with a noise adaptive fidelity term derived based on the Bayesian MAP estimator. As known from the literature, these TV based models eventually settle down to constant patch approximations resulting in block effect and moreover the textured regions are not properly preserved in the course of their evolution. Gradient vector fields were introduced in the literature to address the issues related to the piecewise linear approximation of second order nonlinear PDE models, see Dong and Liu (2009) and Shi (2016) for the details of the subject matter.

In this chapter a gradient fidelity based image despeckling approach is proposed for restoring images. This approach is slightly different from the previous two approaches proposed in Chapters 3 and 4. This model does not possess a direct energy functional (unlike the usual variational models), rather it is designed as a PDE approach for despeckling the data. This model is also solved using a fast numerical scheme based on the SB iteration, yielding a faster convergence. The main focus of this model is to despeckle and deblur data without forming constant patches in the restored version unlike the usual second order PDE models. This method is tested using various kinds of images from SAR and US applications along with natural and synthetic images. Since the method does not possess a direct functional a deep theoretical study regarding the existence and uniqueness of the model is not performed. However, a detailed empirical study has been carried-out regarding the performance of the model.

The remaining sections of this chapter are organized as follows. In the Section 5.2, we introduce a non-local total variational functional coupled with non-local gradient fidelity and noise adaptive fidelity term to restore images from Gamma distributed data-dependent noise and linear shift-invariant blur. The Section 5.3 is dedicated for the explanations regarding the SB formulation for the proposed model. In Section 5.4, the experimental results and discussions are provided.

5.2 The Proposed Non-Local Gradient Fidelity Model

The first task is to determine the MAP estimator for the original image \mathbf{u} given the observed one \mathbf{u}_0 (see Appendix B.2 for details of the derivation). We use non-local TV

prior in place of the prior probability $p(\mathbf{u})$.

Now we design the regularization prior using the non-local total variation formulation given by Gilboa and Osher (2008). The proposed Non-Local Gradient Fidelity (NLGF) model for data-dependent Gamma noise distribution (based on Liu et al. (2014)) whose minimization functional takes the form,

$$\min_{\mathbf{u}} \left\{ \|\nabla_{\text{NL}} \mathbf{u}\| + \lambda (\ln(\mathbf{K}\mathbf{u}) + \mathbf{u}_0/(\mathbf{K}\mathbf{u})) + \beta \left\| |\nabla_{\text{NL}} \mathbf{u} - \nabla_{\text{NL}} \mathbf{u}_0|^{\alpha-1} \otimes |\nabla_{\text{NL}} \mathbf{u} - \nabla_{\text{NL}} \mathbf{u}_0| \right\|_{L^2}^2 \right\}, \quad (5.6)$$

subject to the constraint $\mathbf{d} = \nabla_{\text{NL}} \mathbf{u}$, where ∇_{NL} denotes the non-local gradient. Now considering an unconstrained formulation of the above problem yields

$$\min_{\mathbf{d}, \mathbf{u}} \left\{ \|\mathbf{d}\| + \lambda (\ln(\mathbf{K}\mathbf{u}) + \mathbf{u}_0/(\mathbf{K}\mathbf{u})) + \beta \left\| |\mathbf{d} - \nabla_{\text{NL}} \mathbf{u}_0|^{\alpha-1} \otimes |\mathbf{d} - \nabla_{\text{NL}} \mathbf{u}_0| \right\|_{L^2}^2 + \gamma \|\mathbf{d} - \nabla_{\text{NL}} \mathbf{u} - \mathbf{b}^k\|_{L^2}^2 \right\} \quad (5.7)$$

where $\mathbf{b}^{n+1} = \mathbf{b}^n + \gamma(\mathbf{d}^{n+1} - \nabla_{\text{NL}} \mathbf{u}^{n+1})$ and $\|\nabla_{\text{NL}} \mathbf{u}\|$ denotes the non-local total Variation norm. (see Gilboa and Osher (2008)) for further details. The detailed definition of non-local derivatives were given in Chapter 2 of this thesis, it is being revisited here to ensure continuity in reading.

The non-local gradient in the above expression i.e., $(\nabla_{\text{NL}} \mathbf{u})(x, y)$ is defined as

$$(\nabla_{\text{NL}} \mathbf{u})(x, y) = (\mathbf{u}(y) - \mathbf{u}(x)) \sqrt{\mathbf{w}(x, y)},$$

(see Buades et al. (2005)) and non-local Laplacian is

$$\Delta_{\text{NL}}(\mathbf{u}(k)) = \sum_{l \in \mathcal{N}_k} \mathbf{w}(k, l) (\mathbf{u}(l) - \mathbf{u}(k)),$$

where the smoothing non-local window function

$$\mathbf{w}(x, y) = \mathbf{d}(x, y)^{-2},$$

and the distance function is given by

$$\mathbf{d}(\mathbf{u}(x), \mathbf{u}(y)) = \int_{\Omega} G_{\sigma}(t) |\mathbf{u}(x+t) - \mathbf{u}(y+t)|^2 dt,$$

where $G_\sigma(t)$ denotes the Gaussian convolved version of t with σ as the spread of the Gaussian kernel.

5.3 Numerical Implementation of the Model

There are many techniques proposed in the literature for solving the model numerically. Starting from the basic gradient descent methods to sophisticated augmented Lagrangian scheme (Chan et al. (2011)), Chambolle projection scheme (Chambolle (2004)) and split-Bregman iteration scheme (Goldstein and Osher, 2009). Here we use Split-Bregman iteration method with alternating minimization procedure to solve the above model, as this scheme is less complex, more powerful and has a good convergence rate. Now the problem

$$\min_{\mathbf{d}, \mathbf{u}} \left\{ \|\mathbf{d}\| + \lambda (\ln(\mathbf{K}\mathbf{u}) + \mathbf{u}_0/(\mathbf{K}\mathbf{u})) + \beta \|\mathbf{d} - \nabla_{\text{NL}}\mathbf{u}_0\|^{\alpha-1} \otimes \|\mathbf{d} - \nabla_{\text{NL}}\mathbf{u}_0\|_{L^2}^2 + \gamma \|\mathbf{d} - \nabla_{\text{NL}}\mathbf{u} - \mathbf{b}^k\|_{L^2}^2 \right\} \quad (5.8)$$

can be split into two parts: \mathbf{u} -subproblem and \mathbf{d} -subproblem. The \mathbf{u} -subproblem is

$$\min_{\mathbf{u}} \left\{ \lambda (\ln(\mathbf{K}\mathbf{u}) + \mathbf{u}_0/(\mathbf{K}\mathbf{u})) + \gamma \|\mathbf{d} - \nabla_{\text{NL}}\mathbf{u} - \mathbf{b}^k\|_{L^2}^2 \right\}. \quad (5.9)$$

Taking the variation of the above sub problem in the direction of u we get

$$\lambda (\mathbf{K}^*(\mathbf{K}\mathbf{u} - \mathbf{u}_0)/(\mathbf{K}\mathbf{u})^2) + \gamma (\text{div}_{\text{NL}}(\mathbf{d} - \mathbf{b}^k) - \Delta_{\text{NL}}\mathbf{u}) = 0. \quad (5.10)$$

The above expression can be solved to get \mathbf{u} . Similarly the \mathbf{d} -subproblem is

$$\min_{\mathbf{d}} \left\{ \|\mathbf{d}\| + \beta \|\mathbf{d} - \nabla_{\text{NL}}\mathbf{u}_0\|^{\alpha-1} \otimes \|\mathbf{d} - \nabla_{\text{NL}}\mathbf{u}_0\|_{L^2}^2 + \gamma \|\mathbf{d} - \nabla_{\text{NL}}\mathbf{u} - \mathbf{b}^k\|_{L^2}^2 \right\}. \quad (5.11)$$

Now taking variation along \mathbf{d} and equating to zero gives the solution to the variable \mathbf{d} . Solving these two sub problems yields the optimal solution for the problem under consideration.

5.4 Experimental Results and Discussions

In this research work, performance of the proposed algorithm is evaluated using different test images. Though the algorithm is tested with a large class of images, the result is shown only for four test images. Further it is confirmed that the model works in similar lines for other images as well. Four different types of images are used to show the test results. A synthetic/phantom image (with constant intensity regions), a natural image (homogeneous intensity regions) and two real speckles images (from US and SAR imaging applications) are selected for demonstrating the test results of various methods considered in this chapter. The first two images (the phantom image and the natural image) are synthetically corrupted with Gamma distributed speckle whereas the other two images are speckled in its original form.

The test results are shown in Figures 5.1 and 5.2 for the natural image and phantom image, respectively, which are synthetically corrupted by the Gamma noise. Similarly, Figure 5.3 shows the test results of the US image of a woman breast and Figure 5.4 shows the results of the SAR image acquired from Sandia National Laboratory. The results in favour of the proposed method are shown in the last sub-figures of each figure (i.e. Figure 5.1(h), 5.2 (h), 5.3 (g) and 5.4 (g)). The restoration capability of various models are demonstrated in these figures. The methods used for comparison are Aubert and Aujol (2008) model, SRAD (Yu and Acton, 2002), OSRAD (Krissian et al., 2007), gradient-fidelity model by Liu et al. (2014). As evident from these test results the proposed method has restored the images duly preserving the image details and piecewise linear approximation is not as evident as in other second order models such as Aubert and Aujol (2008) model (shown in the respective sub-figures of each figure). The natural image is shown to demonstrate the performance of the filters in homogeneous intensity regions and the synthetic/phantom image is shown for demonstration of the performance of the filters in constant intensity regions, edges and corners and the original speckled images are meant to show the performance in real-time applications. From these test results it is pretty obvious that the proposed strategy has categorically demonstrated its performance in despeckling and deblurring data under these different image characteristics.

Further the statistical measures like Peak Signal to Noise Ratio (PSNR) and mean Structural Similarity (SSIM) index (see Wang et al. (2004)) are used for quantitatively analyzing the noise reduction, structure and contrast preservation capability of the models under consideration. The formulation of PSNR and SSIM were given in equation (3.15) and (3.16), respectively. The results obtained for PSNR and SSIM after restoring with different methods are shown in Tables 5.2 and 5.3, respectively. The higher PSNR

value indicates a better signal preservation capability. Similarly the SSIM values in the range $[0 - 1]$ indicate the structure preservation capability of the model (the value of the measure is 1 for the ideal case). The detailed description and definition of these measures are given in equations (3.15) and (3.16) respectively. From the tables showing the statistical measures, one can conclude that the proposed model outperform others in terms of signal, structure and contrast preservation. The values of PSNR and SSIM are higher for the proposed model compared to the other ones. The number of iterations taken to converge to the desired solution by various methods are given in Table 5.1. From this table it is evident that, the proposed model converges faster under the split-Bregman formulation compared to the other methods (using the explicit schemes).

As evident from these results (both visual and numerical) we conclude that, the proposed model (using the gradient fidelity) performs pretty well in terms of noise reduction and structure preservation in comparison to the other models considered for the comparison purpose.

Table 5.1 Number of iterations taken by each method to converge to the desired solution for various test images.

Image name	Noisy & Blurred image	AA	SRAD	OSRAD	NLGF	Proposed method
Peppers	0.1,2	500	5200	450	300	80
Phantom	0.1,2	450	530	400	300	70
Woman breast (ultrasound)		300	320	250	260	50
SAR		450	420	400	350	60

In a nut shell, the gradient fidelity model is found to be efficient in removal of speckles and blur from various input images falling under different categories and derived from different application domains. The effect of the gradient fidelity along with the normal data-fidelity is duly noticeable in the test results (both visual and statistical ones).

Table 5.2 PSNR (in dB) evaluated for various restoration methods for different images. (The Gamma noise variance of the input image is :0.2)

Image name	Noisy & Blurred image	AA	SRAD	OSRAD	BM3D	NLGF	proposed method
Phantom	27.67	29.17	28.41	28.89	28.94	29.26	29.53
Baboon	24.2	26.5	27.1	27.5	27.8	25.3	28.2
Boat	24.3	26.2	27.2	28.1	27.6	25.4	28.9
Woman	24.6	26.4	27.1	27.8	26.25	25.8	28.2

Table 5.3 SSIM evaluated for various restoration methods for different images. (The Gamma noise variance of the input image is :0.2)

Image name	Noisy & Blurred image	AA	SRAD	OSRAD	BM3D	NLGF	proposed method
Phantom	0.81	0.90	0.91	0.92	0.92	0.91	0.93
Baboon	0.65	0.72	0.73	0.75	0.76	0.67	0.78
Boat	0.66	0.74	0.76	0.79	0.78	0.64	0.81
Woman	0.64	0.72	0.75	0.77	0.78	0.68	0.80

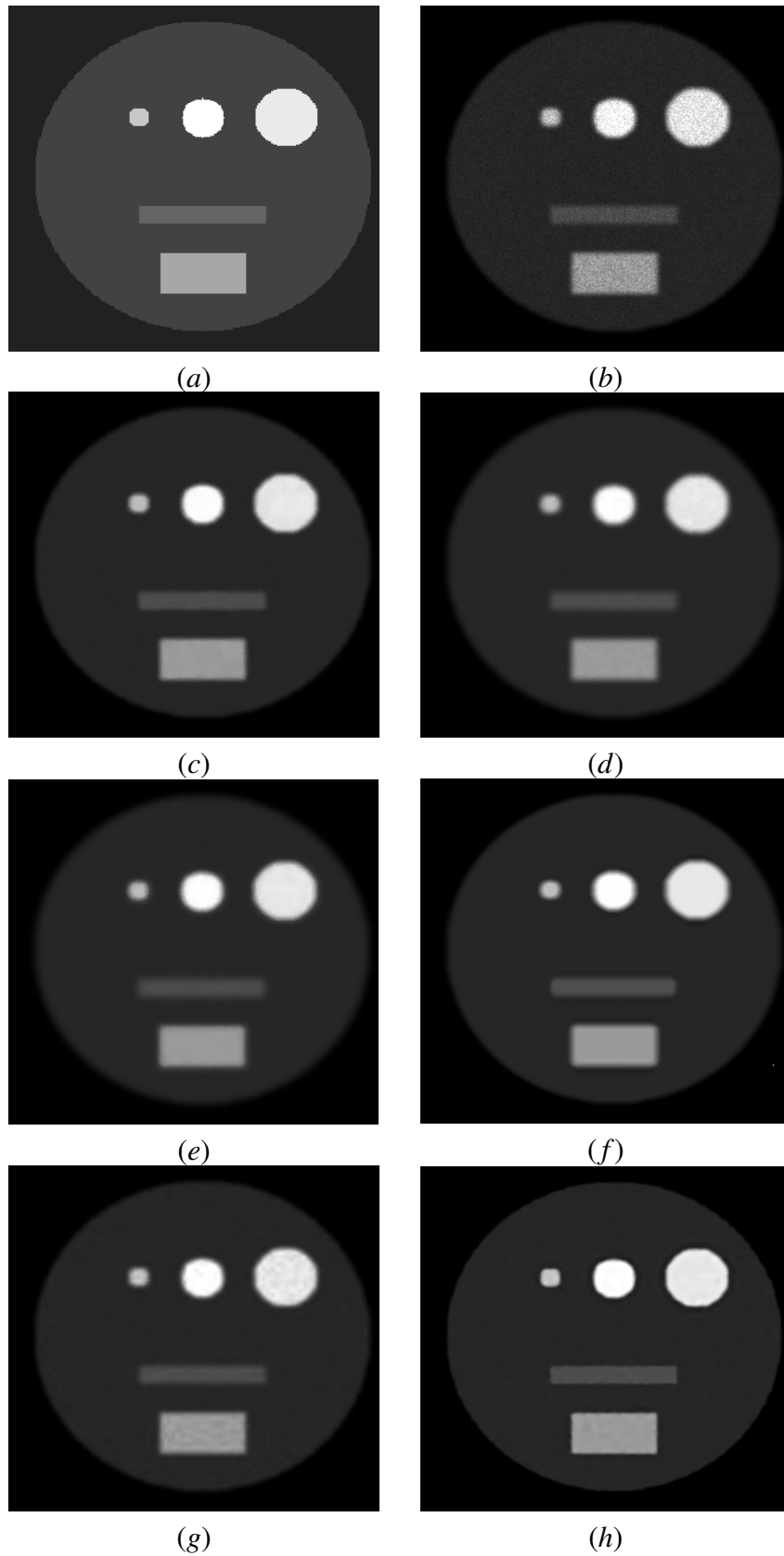


Figure 5.1 (a). Original Phantom image; (b). Noisy and Blur (0.1 and 2 respectively) image; (c). Restored using AA method; (d). SRAD method; (e). OSRAD method; (f). BM3D method; (g) NLGF method; (h). Restored using the proposed method.

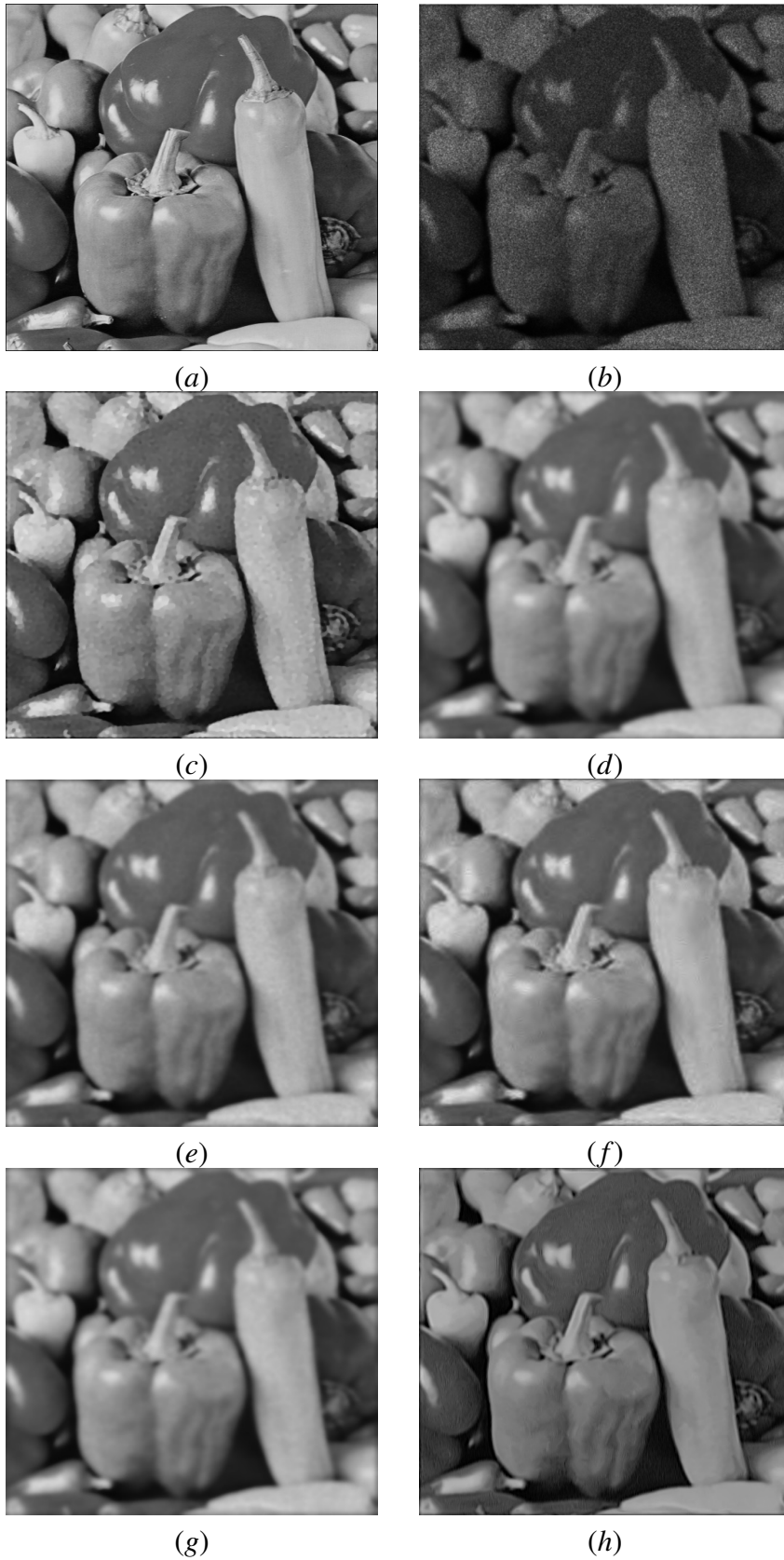


Figure 5.2 (a). Original peppers image; (b). Noisy and Blur (0.1 and 2 respectively) image; (c). Restored using AA method; (d). SRAD method; (e). OSRAD method; (f). BM3D method; (g) NLGF method; (h). Restored using the proposed method.

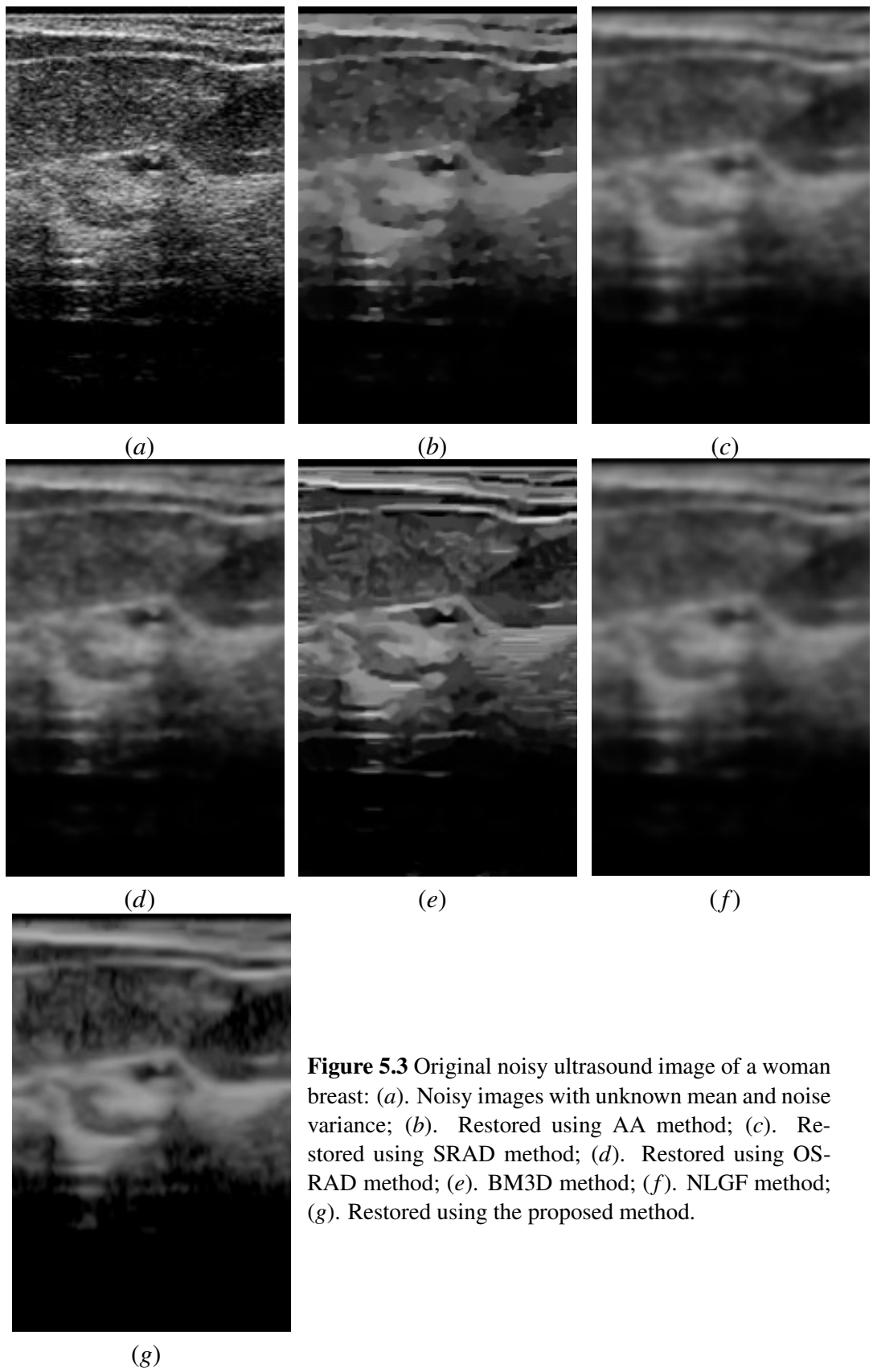


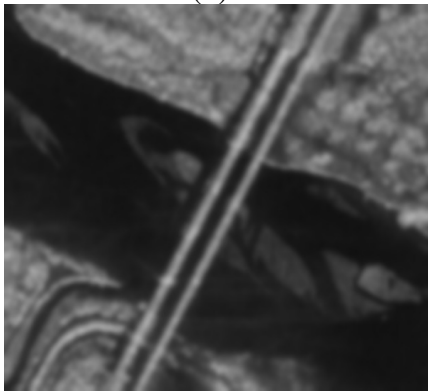
Figure 5.3 Original noisy ultrasound image of a woman breast: (a). Noisy images with unknown mean and noise variance; (b). Restored using AA method; (c). Restored using SRAD method; (d). Restored using OS-RAD method; (e). BM3D method; (f). NLGF method; (g). Restored using the proposed method.



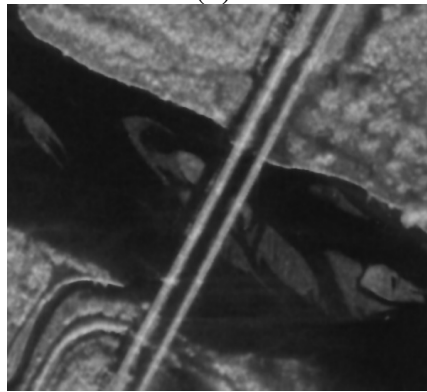
(a)



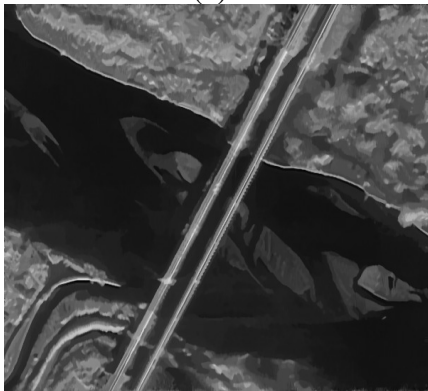
(b)



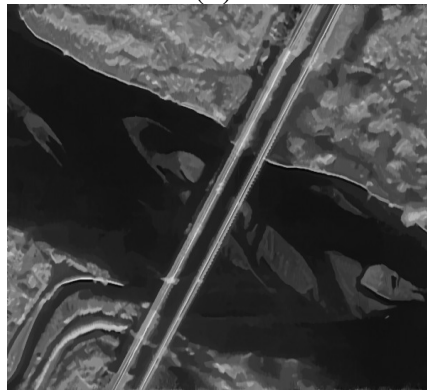
(c)



(d)



(e)



(f)



(g)

Figure 5.4 SAR image from the Sandia National Laboratory, restored using various methods: (a). Noisy images with unknown mean and noise variance; (b). Restored using AA method; (c). SRAD method; (d). OSRAD method; (e). BM3D method; (f). NLGF method; (g). Restored using the proposed method.

Chapter 6

CONCLUSION AND FUTURE SCOPE

6.1 Concluding Remarks

In this thesis three novel methods were proposed for despeckling and deblurring images which are corrupted with Gamma distributed speckles and linear blurring artefacts. Two non-local variational approaches and a non-local Gradient fidelity based PDE approach was introduced as a part of this thesis. All methods are numerically implemented using fast solvers to improve the convergence rate and reduce the parameter sensitivity. The implementation of these model are done using Matlab R2017b (some sample codes used for implementation are given in Appendix D). All comparative analysis are performed using an Intel Core i7-6700 processor with 16GB DDRAM with a graphic card configuration: 4GB NVIDIA 940MX.

The first variational approach (discussed in Chapter 3) is based on the non-local total bounded variation was designed to handle speckles in US images. Since US images contains numerous fine details, despeckling them usually results in smoothed structures, which eventually results in improper diagnosis of the data. This has been addressed effectively by using non-local TBV regularization approach which eventually preserve the details in the course of its evolution. The model is defined in the space of bounded variation where the total variation is bounded, leading to a stable solution. The condition for existence of a unique solution is analysed. The problem has a unique solution under the conditions mentioned in Appendix B.1 as the functional becomes convex in the strict sense, under the conditions. The parameter sensitivity has been reduced and the convergence rate has been improved in the model by employing the SB scheme. An adaptive choice of the parameter makes the model more generic.

In the fourth chapter, another variational approach has been proposed for despeckling SAR imagery. The SAR images contain various constant intensity regions separated by well defined edges. Therefore, the usual despeckling models distorts the edge

information during their evolution. Moreover, the constant patches formed by the piecewise linear approximation yields spurious regions severely hindering the analysis phase. These issues were duly addressed in this Chapter, where a despeckling and deblurring model has been designed to restore the SAR images from their speckled observations. The level-set formulation using the modified Mumford-Shah and Ambrosio Tortorelli formulation evolves the level curves and stop their evolution at the edge points. The functional of the level-set contains a smoothing term and an edge-detection term. The smoothing term controls the magnitude of diffusion and the edge-detection term acts as a stopping condition. The curves evolve within the image unlike the segmentation algorithms (wherein the curves evolve in a separate image). The curve evolution eventually removes speckles in the data without affecting the edge features. Since the model is anisotropic in nature it tends to smoothen the data along the edges but not across it (as component normal to the level-curve in this model is negligible). Though, it can preserve the edges pretty well compared to the other despeckling models including the one presented in the first chapter, it performs slightly on the lower side in terms of the preservation of image details. This is very well explained by the behavior of level-set models which tends to smoothen the structures during the evolution of the level-curves.

Finally, a gradient fidelity model has been proposed in Chapter 5. This can work with both SAR and US images however, since the model is non-convex, the solution is not globally optimal. The model may converge to sub optimal solution (for an appropriately chosen time-step) in the course of its evolution however, adopting the SB scheme can reduce the effect of the time-step on the convergence rate of the model. Nevertheless, the model has been observed to perform well for various input images from different application domains. Though it removes speckles from various kinds of images, it works slightly on the lower side compared to the two methods discussed above in case of US and SAR imagery. As observed from the literature the level-set methods identify and preserve the edges better compared to the anisotropic methods and moreover, the smoothing happens along the level curve, which could reduce the noise along the edges. Secondly, the first variational model has better noise adaptability and detail preservation capability compared to the other models due to the presence of non-local TBV as the regularization prior. Since each model is defined for a particular task, the cross comparison of the proposed models is not done explicitly.

6.1.1 Comparative analysis of the proposed models

A cross comparison between the proposed models has been performed in this section. Three models have been proposed as a part of this thesis work. The first two models

are based on the variational framework and the last one is a gradient fidelity model. The first two models are derived using the Bayesian framework considering the noise distribution as Gamma. Here the models tune their data fidelity aspects based on the assumption of the noise distribution. Therefore, they are more efficient in restoring speckles with Gamma distribution. Among these variational models, one uses a total bounded variation to regularize and it is more effective in restoring speckled images compared to the rest of the models. This fact can be verified from the visual representations of various test results. The switching of norms in total bounded variation makes it more robust. However, the model based on level-set formulation yields a stable solution which converges at a higher rate under a split-Bregman iterative scheme. The gradient fidelity model mainly addressed the issue due to piecewise linear approximation of non-linear PDE and L^1 regularization models. The results shown in Figure 6.1 demonstrates the performance of various models proposed in this thesis. From visual analysis one can observe the facts stated above.

The models are statistically verified using PSNR and SSIM in tables 6.1,6.2, respectively. The variational model using total bounded variation is observed to outperform the other models in terms of these measures. The level set model performs slightly inferior to the earlier model. Finally, the gradient fidelity model performs slightly inferior to the other two models due to the reasons stated in the experimental section of Chapter 5.

Table 6.1 PSNR (Blurring kernel size and noise variance: 2, 0.1, respectively) evaluated for different images using proposed restoration models.

Image name	Noisy& Blurred image	NLGF method	Level-set method	NLTBV method
Lena	25.83	26.65	27.14	27.89
Satellite	25.26	25.68	25.56	26.97
Synthetic	19.42	22.68	22.69	22.96

Table 6.2 SSIM (Blurring kernel size and noise variance: 2, 0.1, respectively) evaluated for different images using proposed restoration models.

Image name	Noisy& Blurred image	NLGF method	Level-set method	NLTBV method
Lena	0.60	0.76	0.77	0.78
Satellite	0.85	0.89	0.90	0.91
Synthetic	0.49	0.81	0.82	0.83

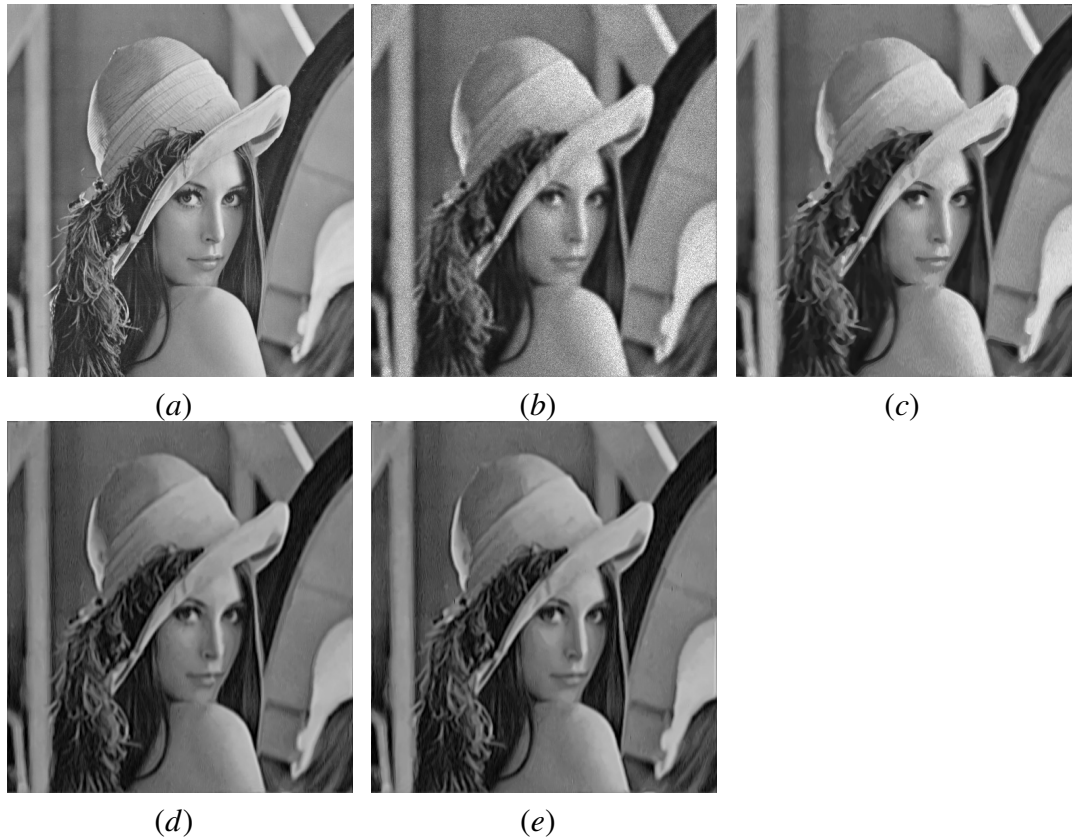


Figure 6.1 Images [(a) Lena (b) Noisy and blurred image (c) The restored image by NLGF method (d) The restored image by speckle reducing Level-set method (e)The restored image by NLTBV method

6.2 Future Research Directions

Even though, we had proposed three fast and efficient algorithms for despeckling and deblurring the data, further improvisations are possible in terms of computational speed or reducing the cost, using the other comparable schemes such as projections methods. Projection methods have taken a step forward in comparison to the existing fast solvers. It is possible to reformulate the problems under a projection framework to improve the computational speed. Moreover, as already pointed out earlier in this thesis, restoration is an approximation problem which is inverse and ill-posed in nature, so it is always possible to improve the approximation in terms of the regularization and the data fidelity. Therefore, improvement in terms of accuracy is still open for exploration.

Appendix A

A.1 Ultrasound Images

An US or ultrasonography is a medical imaging technique which uses high frequency sound waves to capture live images of organs within the human body. Similar technology is being used by radars and sonars, which are primarily used in the defense applications to detect ships and aeroplanes. An US imaging technique allows doctors to see problems of internal organs of a human body, blood vessels, tissues, size, structure and injuries without actually making an incision. The US imaging has been extensively used for the last two decades in medical imaging applications and it has a remarkable safety record (Chan and Perlas, 2011). The US imaging is based on non-ionizing radiation, hence it is less hazardous to the humans compared to x-rays. Further, it is inexpensive compared to the other imaging systems and can fetch real-time data (because of live screening) from the subject.

A.1.1 Ultrasound Image Formation

Ultrasound imaging technique uses sound waves in the range of 1-20 MHz, however lower frequency waves (2-5 MHz) are used for imaging deeper structures as they have more penetration capacity (Chan and Perlas, 2011). A transducer (hand-held probe) is used for transmitting sound waves into patient's body, which gets in contact with the body through a gel. While passing through the human tissue US waves gets partly transmitted, reflected, scattered or transformed into heat based on the tissue property (Chan and Perlas, 2011). The echos reflected back to the transducer gets recorded and further processed by the scanner to form the final gray-scale image called ultrasonogram. If US wave hits a surface smaller than its wavelength, or rough it gets scattered (Chan and Perlas, 2011). The waves after scattering will be of random phase and their superposition will lead to dark and bright spots in images called speckles, refer Forouzanfar and Abrishami-Moghaddam (2010) for the details. Formation of this noise will be

Disk storage device:- Stores the acquires images.

Printer:- Prints the image from the displayed data.

The parts of US machine are shown in Figure A.2. The image formation in an US system is demonstrated in this figure. As the sound signals transmitted by the transducer undergoes partial scattering, the reflected waves captured through the echoes are generally out-of phase and suffer from scattering issues like speckles, as pointed out earlier.

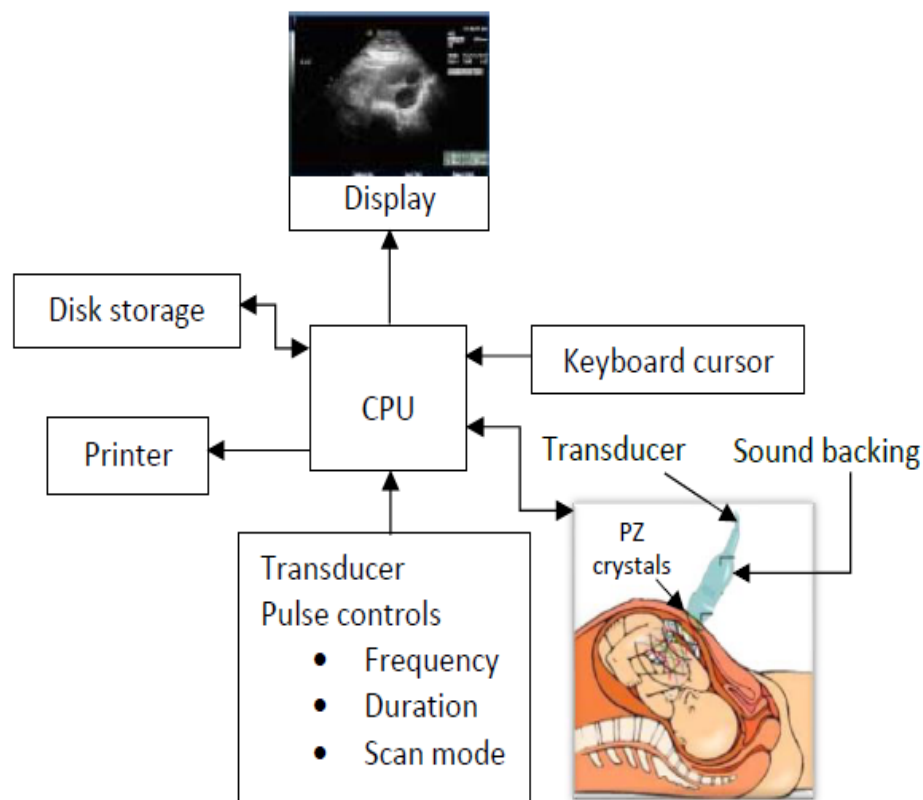


Figure A.2 The parts of an ultrasound machine.

US imaging has become a popular medical imaging technique over the last few years. US imaging can be employed in all medical imaging application. In particular, since US imaging is a low-risk and a painless application, it can be used in sensitive areas, such as in prenatal care or examination of the obstetrics, gynecology, urology (urinary), nephrology (kidneys), cardiology (heart) etc.

A.2 Synthetic Aperture Radar Images

Radio Detection and Ranging, popularly known as RADAR has been widely used in various domains such as military, oceanography, meteorology etc. for monitoring, imaging, detecting and positioning events, objects or scenes. A RADAR system has mainly five components which include a transmitter, switch, antenna, receiver and recorder (Chan and Koo, 2008). Figure A.3 shows the basic block diagram of a radar system. The transmitter generates electromagnetic signals and switch controls the antenna and switches it between transmitting and receiving signals. The antenna either sends electromagnetic signals for imaging or receives the reflected signals. The receiver processes echo signals and the recorder records or stores the data for later processing (Kuttikkad and Chellappa, 2000). The amount of details a radar system can resolve gets affected by its antenna size. In a real array imaging radar, antenna produces a fan beam and here beam width and pulse length determines the resolution. SAR comes under RADAR based systems but it gives finer resolution than the typical beam scanning radars as it uses a moving radar antenna. SAR is mainly used for imaging objects or landscapes and it generally gives the two dimensional(2D) or three-dimensional mapping of the scene. Figure A.4 shows a 2D-SAR image released by European Remote Sensing (ERS) satellite. Compared to the optical sensors that work in the visible or infrared band, SAR images provide different information about the imaging area which includes surface roughness, geometric structure, orientation, moisture content etc. The electro-optical cameras are only capable of day-light imaging whereas a SAR system used in appropriate frequency with its own source of illumination can form the images at any time and any weather conditions (Chan and Koo, 2008; Kuttikkad and Chellappa, 2000). The electromagnetic waves transmitted from the SAR system will be always in phase and their interaction with the surroundings will be very less. However, after hitting the target the waves reflected back will never be in phase due to several reasons, like bounce scattering of some waves due to roughness, the difference in distance the waves travel etc. According to Herve et al. (1998), the movement of the synthesized antenna can also cause the signal to go out of phase (Goodman, 1976). The constructive and destructive interference of these out of phase waves produces the granular noise called speckle and hence the SAR image fails to have a constant mean radiometric level in homogeneous areas (Bruniquel and Lopes, 1997).

Speckle noise in Radar images has a standard deviation linearly related to the mean and is often modeled as a multiplicative process. This means that, for a higher strength of the signal the noise variance also will be higher. As a result, more speckle noise is

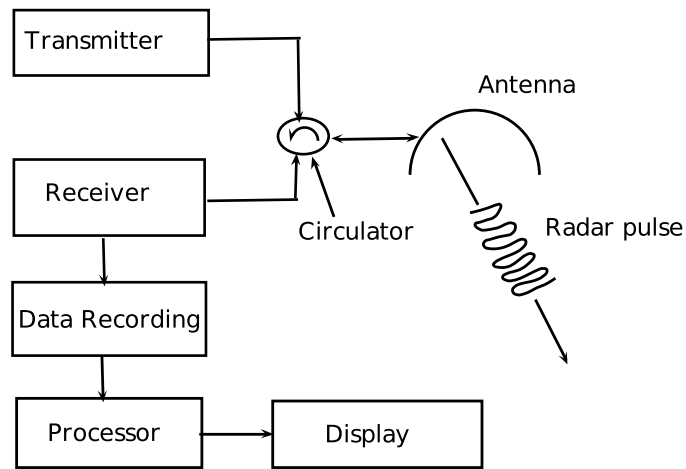


Figure A.3 Basic Block Diagram of Radar System

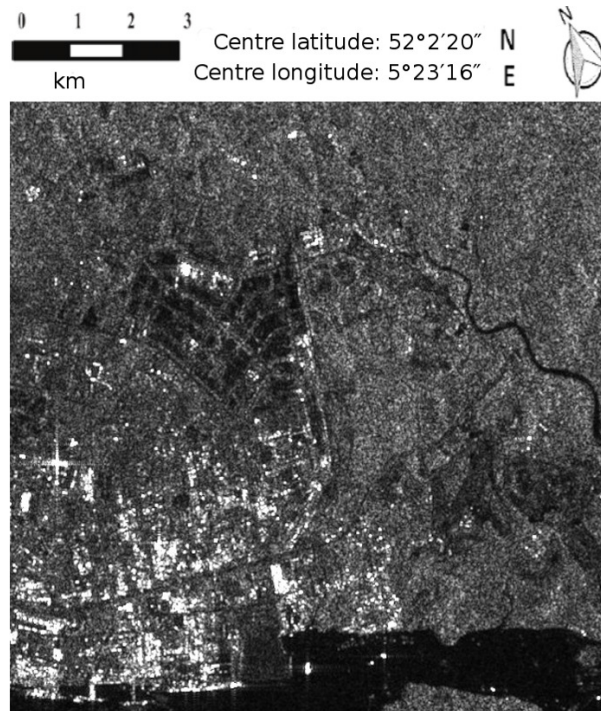


Figure A.4 ERS Satellite SAR image

commonly present near brighter pixel areas (North and Yu, 2001). According to Hervet et al. (1998), the statistics of the speckle noise are well known. The noise of single-look SAR amplitude imagery often has a Rayleigh distribution, whereas a multi-look SAR imagery usually follows a gamma distribution, assuming the looks are independent (Lee, 1980).

A radar sends a coherent wave, which reflects on the ground and then gets registered by the radar sensor (Tuthill et al., 1988). When the coherent wave gets reflected

on a coarse surface (compared to the radar wavelength), then the image processed by the system is degraded by a large amplitude noisy signal, this gives a speckled aspect to the image and this is the reason such a noise is called speckle, refer (Jidesh, 2014) for further details. Since speckle is a multiplicative data dependent noise, the noise distribution varies with reference to the intensity characteristics of the image. In (Tuthill et al., 1988), the authors analyzed that, when the scatter density (the number of scatters per resolution cell) is more than 10, this speckle noise follows a Rayleigh distribution. However, in satellite images the final image is obtained by adding n images with independent intensity distributions and a common mean, hence the intensity follows a Gamma law and therefore the speckle noise is also assumed to follow a Gamma law with mean equals to one, refer (Aubert and Aujol, 2008) for further details. While denoising, distribution of noise also needs to be considered to perform a meaningful restoration and the distribution varies with the imaging techniques used.

The presence of speckle may decrease the utility of SAR imagery by reducing the ability to detect ground targets and obscuring the recognition of spatial patterns (Sheng and Xia, 1996). Consequently, it not only complicates the visual image interpretation but also makes automated digital image classification a difficult problem. Therefore, speckle noise in radar data must often be reduced before the data can be used for further analysis or information extraction. Several despeckling filters have been proposed in order to remove multiplicative speckle noise. In general, no filter consistently outperforms all the others. Each filter has its unique strengths and limitations.

A.2.1 Applications of the Synthetic Aperture Radar Imaging Systems

The applications of SAR imaging are increasing day by day due to the advent of new technologies. The major areas, where this imaging technique used are highlighted below:

- Moving target indication.
- Reconnaissance, Surveillance, and Targeting.
- Environmental monitoring.

Appendix B

In this section the existence and uniqueness of the solution (of the functional given in (3.3)), the derivation of its MAP estimator, MLE of the noise parameters, evaluation of the regularization parameter and the convergence of the solution are being analyzed.

B.1 Theoretical Analysis of the Model

This section provides the required mathematical preliminaries to prove the existence and uniqueness of the given restoration model. The following definition, propositions and theorem are extracted (and modified to suit the proposed model) from Liu and Huang (2010) and Liu and Huang (2012) and presented here for completeness of the work. Consider the proposed total bounded variation model for image restoration

$$\min_{\mathbf{u} \in S(\Omega)} \int_{\Omega} |\nabla_{\text{NL}} \mathbf{u}| + \frac{\beta}{2} \|\mathbf{u}\|_{L^2}^2 + \lambda \int_{\Omega} \left(\ln(\mathbf{K}\mathbf{u}) + \frac{\mathbf{u}_0}{\mathbf{K}\mathbf{u}} \right) dx \quad (\text{B.1})$$

where $S(\Omega) = \{\mathbf{u} \in \text{BV}(\Omega), \mathbf{u} > 0\}$, $\Omega \subseteq \mathbb{R}^N$ is a bounded open subset with Lipschitzian boundary, $\lambda > 0, \beta \geq 0$ are the given parameters and $\mathbf{K} \in \mathcal{L}(L^2(\Omega) \cap \text{BV}(\Omega))$. Note that $L^2(\Omega)$ denotes the space of all square-integrable functions and \mathcal{L} is an intersection of L^2 and BV spaces. Assume that \mathbf{K} is a bounded linear blur operator, subject to $\mathbf{K}.1 \neq 0, \mathbf{u}_0 > 0$ and bounded. According to Giusti (1984) we have $\text{BV}(\Omega) \subset L^2(\Omega)$. Thus, the space: $\text{BV}(\Omega)$, equipped with the full norm $|\nabla_{\text{NL}} \mathbf{u}|_1 + \frac{\beta}{2} \|\mathbf{u}\|_{L^2}^2$ is also a Banach space (a complete space with respect to the norm)..

Definition B.1.1. Let $\Omega \subseteq \mathbb{R}^N$ be a open bounded domain. Let $\mathbf{u} \in L^1_{loc}(\Omega)$. Then the total variation of \mathbf{u} follows the definition:

$$\int_{\Omega} |\nabla \mathbf{u}| = \sup_{\xi \in C_c^1(\Omega, \mathbb{R}^N)} \left(\int_{\Omega} \mathbf{u}(x) \text{div} \xi(x) dx : |\xi(x)|_{L^\infty} \leq 1, \forall x \in \Omega \right), \quad (\text{B.2})$$

where L^∞ is the infinity/supremum norm and C_c^1 denotes smooth (continuous) functions with compact support.

Proposition B.1.1. (Lower semicontinuity): Suppose that $\{\mathbf{u}_n\}_{n=1}^\infty \subset \text{BV}(\Omega)$ and $\mathbf{u} \in L^1(\Omega)$ (the space of absolute-integrable functions) is such that $\mathbf{u}_n \rightarrow \mathbf{u}$ in $L^1(\Omega)$, then

$$\int_{\Omega} |\nabla \mathbf{u}| dx \leq \liminf_{n \rightarrow \infty} \int_{\Omega} |\nabla \mathbf{u}_n| dx,$$

Proposition B.1.2. If $\mathbf{u} \in \text{BV}(\Omega)$ then there exists a minimizing sequence $\{\mathbf{u}_n\}_{n=1}^\infty \subset \text{BV}(\Omega)$ such that

$$\lim_{n \rightarrow \infty} \|\mathbf{u}_n - \mathbf{u}\|_{L^1(\Omega)} = 0,$$

and

$$\lim_{n \rightarrow \infty} \int_{\Omega} |\nabla \mathbf{u}_n| dx = \int_{\Omega} |\nabla \mathbf{u}| dx.$$

At this stage we can present the existence and uniqueness of the optimization problem in (B.1).

B.1.1 Existence and Uniqueness

In this section, it is shown that there exists a solution for the problem (B.1) and it is unique.

Theorem B.1.1. Let \mathbf{u}_0 be in $L^\infty(\Omega)$ with $\inf_{\Omega} \mathbf{u}_0 > 0$; then problem (B.1) has at least one solution \mathbf{u} in $\text{BV}(\Omega)$. If \mathbf{K} is injective, then the solution is unique such that $0 < \mathbf{u} < 2\mathbf{u}_0$, satisfying

$$0 < \inf_{\Omega} \mathbf{u}_0 \leq \mathbf{u} \leq \sup_{\Omega} \mathbf{u}_0 \quad (\text{B.3})$$

We note that *sup* and *inf* are the supremum and the infimum of the set.

Proof. Now let us denote $\inf \mathbf{u}_0$ by α and $\sup \mathbf{u}_0$ by β . Let us consider a minimizing sequence $(\mathbf{u}_n) \in S(\Omega)$ for problem (B.1). Let us consider that $J(\mathbf{u}) = \int_{\Omega} |\nabla_{\text{NL}} \mathbf{u}|$, thus the proposed minimization problems takes the form

$$E(\mathbf{u}) = J(\mathbf{u}) + \frac{\beta}{2} \|\mathbf{u}\|_{L^2}^2 + \lambda \int_{\Omega} \left(\ln(\mathbf{K}\mathbf{u}) + \frac{\mathbf{u}_0}{\mathbf{K}\mathbf{u}} \right) \quad (\text{B.4})$$

Now the proof is split into two parts to make it more clear.

Part 1. First show that we can assume without restriction that $\alpha \leq \mathbf{u}_n \leq \beta$. Then remark that $\mathbf{x} \mapsto \ln(\mathbf{x}) + \frac{\mathbf{u}_0}{\mathbf{x}}$ is decreasing if $\mathbf{x} \in (0, \mathbf{u}_0)$ and increasing if $\mathbf{x} \in (\mathbf{u}_0, +\infty)$.

Therefore, if $\mathbf{M} \geq \mathbf{u}_0$, one always has

$$\left(\ln(\min(\mathbf{K}\mathbf{x}, \mathbf{M})) + \frac{\mathbf{u}_0}{\min(\mathbf{K}\mathbf{x}, \mathbf{M})} \right) \leq \left(\ln(\mathbf{K}\mathbf{x}) + \frac{\mathbf{u}_0}{\mathbf{K}\mathbf{x}} \right) \quad (\text{B.5})$$

let $\mathbf{M} = \beta = \sup \mathbf{u}_0$, then find

$$\left(\ln(\inf(\mathbf{K}\mathbf{u}, \beta)) + \frac{\mathbf{u}_0}{\inf(\mathbf{K}\mathbf{u}, \beta)} \right) \leq \left(\ln(\mathbf{K}\mathbf{u}) + \frac{\mathbf{u}_0}{\mathbf{K}\mathbf{u}} \right) \quad (\text{B.6})$$

Moreover, according to (see Lemma 1 in section 4.3 of Kornprobst et al. (1999), for instance)

$$J(\inf(\mathbf{u}, \beta)) \leq J(\mathbf{u})$$

and

$$\inf(\mathbf{u}, \beta) \leq \mathbf{u}$$

thus deduce that

$$E(\inf(\mathbf{u}, \beta)) \leq E(\mathbf{u})$$

similarly $E(\sup(\mathbf{u}, \alpha)) \leq E(\mathbf{u})$, where $\alpha = \inf \mathbf{u}_0$.

Part 2: From the above proof, one can assume that $\alpha \leq \mathbf{u}_n \leq \beta$. This implies in particular that \mathbf{u}_n is bounded in $L^1(\Omega)$.

By the definition of (\mathbf{u}_n) , the sequence $E(\mathbf{u}_n)$ is bounded, i.e., there exists a constant C such that

$$J(\mathbf{u}_n) + \frac{\beta}{2} \|\mathbf{u}_n\|_{L^2}^2 + \lambda \int_{\Omega} \left(\ln(\mathbf{K}\mathbf{u}_n) + \frac{\mathbf{u}_0}{\mathbf{K}\mathbf{u}_n} \right) \leq C.$$

Moreover $\int_{\Omega} \left(\ln(\mathbf{K}\mathbf{u}_n) + \frac{\mathbf{u}_0}{\mathbf{K}\mathbf{u}_n} \right) dx$ reaches its minimum value $\int_{\Omega} (1 + \ln(\mathbf{K}\mathbf{u}_0)) dx$ when $\mathbf{K}\mathbf{u}_0 = \mathbf{K}\mathbf{u}_n$, so it can be concluded that \mathbf{u}_n is bounded in $BV(\Omega)$. Considering that $\mathbf{K} \in \mathcal{L}(BV(\Omega))$ and the boundedness of $\|\nabla \mathbf{u}\|_1$, one can deduce that $\{\mathbf{u}_n\}_{n=1}^{\infty}$ is a bounded sequence in $BV(\Omega)$. By the Rellich- Kondrachov compactness theorem, the sequence $\{\mathbf{u}_n\}_{n=1}^{\infty}$ is precompact in $L^1(\Omega)$. Therefore, there exists a function \mathbf{u} satisfying $\mathbf{u}_n \rightarrow \mathbf{u}$ a.e.. The function appears as convex and coercive in $BV(\Omega)$. Necessarily, we have $0 \leq \alpha \leq \mathbf{u} \leq \beta$ and following Fatous lemma and the lower semi-continuity of the total variation, we obtain that \mathbf{u} is a solution of the problem in (B.1).

Next let us prove the uniqueness of the solution. Let $g(\mathbf{u}) = \int_{\Omega} \left(\ln(\mathbf{u}) + \frac{\mathbf{u}_0}{\mathbf{u}} \right) dx$ with $\mathbf{u} = \mathbf{K}\mathbf{u}$. For the given $\mathbf{u}_0 > 0$, we have $g'(\mathbf{u}) = \frac{1}{\mathbf{u}} - \frac{\mathbf{u}_0}{\mathbf{u}^2} = \frac{\mathbf{u} - \mathbf{u}_0}{\mathbf{u}^2}$ and $g''(\mathbf{u}) = \frac{-1}{\mathbf{u}^2} + \frac{2\mathbf{u}_0}{\mathbf{u}^3} = \frac{2\mathbf{u}_0 - \mathbf{u}}{\mathbf{u}^3}$. It can be deduced that if $0 < \mathbf{u} < 2\mathbf{u}_0$, then $g(\mathbf{u})$ is a strictly convex functional, implying the uniqueness of a minimizer. \square

B.2 Derivation of the MAP Estimator

The speckle noise \mathbf{n} follows a Gamma law and the PDF is

$$g(\mathbf{n}) = \frac{L^L}{\Gamma(L)} \mathbf{n}^{L-1} e^{-L\mathbf{n}} \mathbf{1}\{\mathbf{n} \geq 0\}, \quad (\text{B.7})$$

where L stands for the number of images available for averaging purpose and Γ denotes the Gamma function in its usual sense. In satellite imaging sense, high resolution images are formed by averaging many slices after proper registration. Nevertheless, the value of L is 1 when dealing with a single image. To denoise Gamma noise corrupted image, Aubert and Aujol (2008) proposed a modified Total variation model using Bayesian MAP estimator. The MAP estimator is extracted from Aubert and Aujol (2008) and given here for completeness. Adopting Bayes rule: Assume \mathbf{U} and \mathbf{N} are independent variables, with continuous density functions $g_{\mathbf{U}}$ and $g_{\mathbf{N}}$, respectively. Denote by $\mathbf{U}_0 = \mathbf{U}\mathbf{N}$ (for a multiplicative noise set-up). Then for $\mathbf{u} > 0$:

$$g_{\mathbf{N}}\left(\frac{\mathbf{u}_0}{\mathbf{u}}\right) \frac{1}{\mathbf{u}} = g_{\mathbf{U}_0|\mathbf{U}}(\mathbf{u}_0|\mathbf{u}). \quad (\text{B.8})$$

Let us assume that \mathbf{n} follows a gamma law with mean one, and with density function $g_{\mathbf{u}}(\cdot)$, then

$$g_{\mathbf{N}}(\mathbf{n}) = \frac{L^L}{\Gamma(L)} \mathbf{n}^{L-1} e^{-L\mathbf{n}} \mathbf{1}\{\mathbf{n} \geq 0\}, \quad (\text{B.9})$$

deriving the basic concepts from the Bayesian conditional probability we arrive at:

$$g_{\mathbf{U}_0|\mathbf{U}}(u_0|u) = \frac{L^L}{\mathbf{u}^L \Gamma(L)} \mathbf{u}_0^{L-1} e^{(-L\mathbf{u}_0)/\mathbf{u}}. \quad (\text{B.10})$$

Also assume that \mathbf{u} follows a Gibbs prior:

$$g_{\mathbf{U}}(\mathbf{u}) = \frac{1}{Z} \exp(-\lambda \phi(\mathbf{u})), \quad (\text{B.11})$$

where Z is a normalizing constant and ϕ a non negative function. From Bayes rule, we have $P(\mathbf{U}|\mathbf{U}_0) = \frac{P(\mathbf{U}_0|\mathbf{U})P(\mathbf{U})}{P(\mathbf{U}_0)}$. Further, maximizing $P(\mathbf{U}|\mathbf{U}_0)$ amounts to minimizing the negative log-likelihood which implies:

$$\min_{\mathbf{U}} \{-\ln(P(\mathbf{U}|\mathbf{U}_0))\} = \min_{\mathbf{U}} \{-\ln(P(\mathbf{U}_0|\mathbf{U})) - \ln(P(\mathbf{U})) + \ln(P(\mathbf{U}_0))\}. \quad (\text{B.12})$$

Assume that the samples of the noise on each pixel $x \in \mathbf{S}$ (\mathbf{S} is a discrete image domain) are mutually independent and identically distributed with density $g_{\mathbf{N}}$. Therefore we

have:

$$P(\mathbf{U}_0|\mathbf{U}) = \prod_{s \in \mathbf{S}} P(\mathbf{U}_0(s)|\mathbf{U}(s)). \quad (\text{B.13})$$

Since $\ln(P(\mathbf{U}_0))$ is a constant just need to minimize the rest of the terms in B.12. Using B.9 and since Z is a constant and eventually see that minimizing $-\log(P(\mathbf{U}_0|\mathbf{U}))$ amounts to minimizing:

$$\min_{\mathbf{U}} \left\{ - \sum_{s \in \mathbf{S}} \left(\left(L(\ln \mathbf{U}(s) + \frac{\mathbf{U}_0(s)}{\mathbf{U}(s)}) \right) + \lambda \phi(\mathbf{U}(s)) \right) \right\}. \quad (\text{B.14})$$

The previous computation leads to propose the following functional (in the continuous domain) for restoring images corrupted with gamma noise (here assume that the image \mathbf{u}_0 to be a linear blurred and speckled version i.e $\mathbf{u}_0 = \mathbf{K}\mathbf{u}$ where \mathbf{K} is a blurring operator ¹:

$$\int_{\Omega} \left(\ln(\mathbf{K}\mathbf{u}) + \frac{\mathbf{u}_0}{\mathbf{K}\mathbf{u}} \right) dx dy + \frac{\lambda}{L} \int_{\Omega} \phi(\mathbf{u}) dx dy. \quad (\text{B.15})$$

Now replacing the Gibbs prior with NLTBV prior i.e., $\phi(\mathbf{u}) = (|\nabla_{\text{NL}}\mathbf{u}| + \frac{\beta}{2}\|\mathbf{u}\|_{L^2}^2)$ the above expression forms (assuming $L = 1$). So the corresponding energy minimization problem is given as follows:

$$\min_{\mathbf{u}} \left\{ E(\mathbf{u}) = \int_{\Omega} \lambda \left(|\nabla_{\text{NL}}\mathbf{u}| + \frac{\beta}{2}\|\mathbf{u}\|_{L^2}^2 \right) dx dy + \int_{\Omega} \left(\ln(\mathbf{K}\mathbf{u}) + \frac{\mathbf{u}_0}{\mathbf{K}\mathbf{u}} \right) dx dy \right\}. \quad (\text{B.16})$$

B.3 MLE of Noise Parameters

The PDF of a Gamma distribution of a random variable $\mathbf{x} \in (0, \infty)$ with parameters shape $k > 0$ and scale $\theta > 0$ is given as (an additional parameter β is introduced for making the derivations simple). By setting $\beta = 1$ one can get the PDF of the Gamma distribution.

$$p(\mathbf{x}|k, \theta) = \frac{\beta \mathbf{x}^{\beta k - 1}}{\Gamma(k) \theta \beta^k} e^{-(\frac{\mathbf{x}}{\theta})^\beta}. \quad (\text{B.17})$$

The mean and variance of the distribution are evaluated as $\mu = k\theta$ and $\sigma^2 = k\theta^2$, respectively. The mean and variance of the distribution are set as 1 and $1/k$ respectively for the synthetic noisy data and it is evaluated from a homogeneous intensity region using MLE for original noisy data (where these parameters are not known a priori). Now considering \mathbf{x} to be x_1, x_2, \dots, x_n , n independent identically distributed (i.i.d) data.

¹Here we note that in \mathbf{U} and \mathbf{U}_0 (the random variables) are substituted with the original \mathbf{u} and observed \mathbf{u}_0 , images respectively and further the indices are dropped hereafter to avoid confusion in the notation.

Further, from the literature one can know that optimizing a function is equivalent to optimizing its log likelihood. So let us rewrite the above problem in terms of its log likelihood.

$$\ln p(\mathbf{x}_i|k, \theta) = -(\ln \Gamma(k)) - \beta k \ln(\theta) + \ln(\beta) + \frac{1}{n} \sum_{i=1}^n \left((\beta k - 1) \ln(\mathbf{x}_i) - \left(\frac{\mathbf{x}_i}{\theta} \right)^\beta \right). \quad (\text{B.18})$$

Now the parameters can be evaluated by optimizing the function with respect to these parameters. Now maximizing the log likelihood (with reference to the parameters) gives the MLE i.e.

$$\begin{aligned} \max_{k, \theta} \ln p(\mathbf{x}_i|k, \theta) &= \max_{k, \theta, \beta} \{ -(\ln(\Gamma(k))) - \beta k \ln(\theta) + \ln(\beta) \} \\ &+ \max_{k, \theta, \beta} \left\{ \frac{1}{n} \sum_{i=1}^n \left((\beta k - 1) \ln(\mathbf{x}_i) - \left(\frac{\mathbf{x}_i}{\theta} \right)^\beta \right) \right\}, \end{aligned} \quad (\text{B.19})$$

Since the function above is assumed as concave (with respect to the variables) it is possible to take a derivative w.r.t θ , β and k to get two simultaneous equations solving which leads to the estimation of parameters under consideration. Now taking the derivative w.r.t. θ gives

$$\frac{1}{n} \sum_{i=1}^n \frac{\mathbf{x}_i}{\theta} = k, \quad (\text{B.20})$$

or

$$\theta = \frac{\sum_{i=1}^n \mathbf{x}_i}{nk}. \quad (\text{B.21})$$

Now taking the derivative of the above expression w.r.t. β and k gives

$$0 = \frac{1}{\beta} + \frac{k}{n} \sum_{i=0}^n \ln \left(\frac{\mathbf{x}_i}{\alpha} \right) - \frac{1}{n} \sum_{i=0}^n \ln \left(\frac{\mathbf{x}_i}{\alpha} \right) \left(\frac{\mathbf{x}_i}{\alpha} \right)^\beta \quad (\text{B.22})$$

and

$$0 = -\beta \ln(\alpha) - \frac{\Gamma'(k)}{\Gamma(k)} + \frac{\beta}{n} \sum_{i=0}^n \ln(\mathbf{x}_i), \quad (\text{B.23})$$

respectively. Now substituting the value of θ in equation(B.21), gives

$$k = \frac{n \sum \mathbf{x}_i^\beta}{n\beta \sum \mathbf{x}_i^\beta \ln(\mathbf{x}_i) - \beta \sum \ln(\mathbf{x}_i) \sum \mathbf{x}_i^\beta}. \quad (\text{B.24})$$

Further setting $\beta = 1$ (as the distribution is Gamma) gives the estimate for k and then denote it by \hat{k} i.e.

$$\hat{k} = \frac{n \sum \mathbf{x}_i}{n \sum \mathbf{x}_i \ln(\mathbf{x}_i) - \sum \ln(\mathbf{x}_i) \sum \mathbf{x}_i}. \quad (\text{B.25})$$

Substituting the value of k in equation(B.21) yields the estimate for the parameter θ ,

$$\hat{\theta} = \frac{1}{n^2} (n \sum \mathbf{x}_i \ln(\mathbf{x}_i) - \sum \ln(\mathbf{x}_i) \sum \mathbf{x}_i). \quad (\text{B.26})$$

The unbiased estimators for θ and $1/k$ are defined as:

$$\theta = \frac{n}{n-1} \hat{\theta}, \quad (\text{B.27})$$

and

$$k^{-1} = \frac{n}{n-1} \frac{1}{\hat{k}}, \quad (\text{B.28})$$

therefore,

$$\theta = \frac{n}{n-1} \frac{1}{n^2} (n \sum \mathbf{x}_i \ln(\mathbf{x}_i) - \sum \ln(\mathbf{x}_i) \sum \mathbf{x}_i), \quad (\text{B.29})$$

and

$$k^{-1} = \frac{n}{n-1} \frac{(n \sum \mathbf{x}_i \ln(\mathbf{x}_i) - \sum \ln(\mathbf{x}_i) \sum \mathbf{x}_i)}{n \sum \mathbf{x}_i}. \quad (\text{B.30})$$

B.4 Evaluation and Update of λ

The parameter λ is evaluated adaptively in each iteration. The noise model of our assumption is

$$\begin{aligned} \mathbf{u}_0 &= \mathbf{K} \mathbf{u} \mathbf{n} \\ \implies \mathbf{n} &= \frac{\mathbf{u}_0}{\mathbf{K} \mathbf{u}}, \end{aligned} \quad (\text{B.31})$$

assuming a unit mean for the multiplicative Gamma noise we get,

$$(\mathbf{n} - 1)^2 = \left(\frac{\mathbf{u}_0}{\mathbf{K} \mathbf{u}} - 1 \right)^2,$$

now integrating both sides yields:

$$\frac{1}{|\Omega|} \int_{\Omega} (\mathbf{n} - 1)^2 dx dy = \frac{1}{|\Omega|} \int_{\Omega} \left(\frac{\mathbf{u}_0}{\mathbf{K} \mathbf{u}} - 1 \right)^2 dx dy,$$

$\frac{1}{|\Omega|} \int_{\Omega} (\mathbf{n} - 1)^2 dx dy$ defines the noise variance σ^2 , i.e.

$$\sigma^2 = |\Omega| \frac{\|\mathbf{u}_0 - \mathbf{K} \mathbf{u}\|_{L^2}^2}{\|\mathbf{K} \mathbf{u}\|_{L^2}^2},$$

now the parameter λ can be defined in terms of σ^2 (here $|\Omega|$ stands for total number of pixels in the area of image support Ω) as,

$$\lambda_{i+1} = \lambda_i \frac{\|\mathbf{u}_0 - \mathbf{K}\mathbf{u}\|_{L^2}^2}{\sigma^2 \|\mathbf{K}\mathbf{u}\|_{L^2}^2}, \quad (\text{B.32})$$

where λ_0 is initialized as $\frac{1}{\sigma^2}$. The parameter λ is a function of noise variance and when $\frac{\|\mathbf{K}\mathbf{u}\|_{L^2}^2}{\|\mathbf{u}_0 - \mathbf{K}\mathbf{u}\|_{L^2}^2}$ approaches σ^2 the parameter λ converges. The noise variance is evaluated using the MLE as described in Section B.3 for real noisy data.

B.5 Convergence Analysis

Here a notion of converge is provided using the experimental results. Readers are invited to refer Jia et al. (2009) for detailed analysis of the convergence of a similar variational set-up. As already discussed earlier, the minimization problem

$$\min_{\mathbf{u}} E(\mathbf{u}) \quad \text{subject} \quad \mathbf{u}_0 = \mathbf{K}\mathbf{u}, \quad (\text{B.33})$$

has a unique solution $\hat{\mathbf{u}}$. Then one can possibility conclude that, the sequence of iterates (\mathbf{u}_n) converges to the solution $\hat{\mathbf{u}}$ (i.e. $\lim_{n \rightarrow \infty} \mathbf{u}_n = \hat{\mathbf{u}}$) provided $\lim_{n \rightarrow \infty} (\mathbf{u}_n - \mathbf{u}_{n-1}) = 0$, as the sequence is proved to be bounded in the BV space. This can be easily verified using the plot given in Figure 3.9, i.e. as n increases the relative absolute difference: $\frac{\|\mathbf{u}_{n+1} - \mathbf{u}_n\|}{\|\mathbf{u}_{n+1}\|}$ tends to zero. This gives a notion of convergence.

Appendix C

In this Appendix the condition for the existence of a unique solution of the functional in (4.6) is being analyzed.

C.1 Existence of a Unique Solution

Consider the MS functional below:

$$\inf_{\mathbf{u}} \left\{ F(\mathbf{u}) = \beta \int_{\Omega \setminus S_{\mathbf{u}}} \left(\ln(K\mathbf{u}) + \frac{\mathbf{u}_0}{K\mathbf{u}} \right) dx dy + \int_{\Omega \setminus S_{\mathbf{u}}} \alpha |\nabla \mathbf{u}|^2 dx dy + \mathcal{H}^{d-1}(S_{\mathbf{u}}) \right\}. \quad (\text{C.1})$$

In order to show that (C.1) has a solution, the notion of Special functions of Bounded Variation (SBV) and the following important lemma due to Ambrosio (1988) are necessary. These definitions and lemma are extracted from Ambrosio (1988); Bar et al. (2011); Ambrosio et al. (2000) and provided here to ensure completeness of the work and to improve the readability of the text.

Definition C.1.1. (SBV) A function $\mathbf{u} \in L^1(\Omega)$ is a special function of bounded variation on Ω if its distributional derivative can be written as

$$D\mathbf{u} = \nabla \mathbf{u} dx + (\mathbf{u}^+ - \mathbf{u}^-) \vec{N}_{\mathbf{u}} \mathcal{H}^{d-1}|_{S_{\mathbf{u}}} \quad (\text{C.2})$$

such that $\nabla \mathbf{u} \in L^1(\Omega)$, $S_{\mathbf{u}}$ is of finite Hausdorff measure, $(\mathbf{u}^+ - \mathbf{u}^-) \vec{N}_{\mathbf{u}} \chi_{S_{\mathbf{u}}} \in L^1(\Omega, \mathcal{H}^{d-1}|_{S_{\mathbf{u}}}, \mathbb{R}^d)$, where \mathbf{u}^+ and \mathbf{u}^- are the traces of \mathbf{u} on each side of the jump part $S_{\mathbf{u}}$, and $\vec{N}_{\mathbf{u}}$ is the unit normal to $S_{\mathbf{u}}$. The space of spacial functions of bounded variation is denoted by $\text{SBV}(\Omega)$.

Lemma C.1.1. Let $\mathbf{u}_n \in \text{SBV}(\Omega)$ be a sequence of functions such that there exists a constant $C > 0$ with $|\mathbf{u}_n(x)| \leq C < \infty$ a.e. $x \in \Omega$ and $\int_{\Omega} |\nabla \mathbf{u}_n|^2 dx + \mathcal{H}^{d-1}(S_{\mathbf{u}_n}) \leq C$. Then there exists a subsequence \mathbf{u}_{n_k} converging a.e to a function $\mathbf{u} \in \text{SBV}(\Omega)$. Moreover,

$\nabla \mathbf{u}_{n_k}$ converges weakly in $L^2(\Omega)^d$ to $\nabla \mathbf{u}$, and

$$\mathcal{H}^{d-1}(S_u) \leq \liminf_{n_k \rightarrow \infty} \mathcal{H}^{d-1}(S_{u_{n_k}}) \quad (\text{C.3})$$

Theorem C.1.2. Let $\mathbf{u}_0 \in L^\infty(\Omega)$ with $\Omega \subset \mathbb{R}^d$ be open, bounded and connected. There is a minimizer $\mathbf{u} \in \text{SBV}(\Omega) \cap L^\infty(\Omega)$ of

$$F(\mathbf{u}) = \beta \int_{\Omega \setminus S_u} \left(\ln(K\mathbf{u}) + \frac{\mathbf{u}_0}{K\mathbf{u}} \right) dx dy + \int_{\Omega \setminus S_u} \alpha |\nabla \mathbf{u}|^2 dx dy + \mathcal{H}^{d-1}(S_u)$$

Proof:

We notice that $0 \leq \inf_{\text{SBV}(\Omega) \cap L^\infty(\Omega)} F < \infty$ because we can take $\mathbf{u}^0 = 0 \in \text{SBV}(\Omega) \cap L^\infty(\Omega)$ (initial image) and using the fact that $\mathbf{u}_0 \in L^\infty(\Omega) \subset L^2(\Omega)$, $F(\mathbf{u}^0) < \infty$. Thus, there is a minimizing sequence $\mathbf{u}_n \in \text{SBV}(\Omega) \cap L^\infty(\Omega)$ (\mathbf{u}_n denotes the image at n^{th} iteration) satisfying $\lim_{n \rightarrow \infty} F(\mathbf{u}_n) = \inf F$. We also notice that, by the truncation argument from before, we can assume that $\|\mathbf{u}_n\|_\infty \leq \|\mathbf{u}_0\|_\infty < \infty$. Since $F(\mathbf{u}_n) \leq C < \infty$ for all $n \geq 0$ and using $\mathbf{u}_0 \in L^\infty(\Omega) \subset L^2(\Omega)$, we deduce that $\|\mathbf{u}_n\|_2 \leq C$ and $\int_{\Omega \setminus S_{u_n}} |\nabla \mathbf{u}_n|^2 dx + \mathcal{H}^{d-1}|_{S_{u_n}} < C$ for some positive real constant C . Using these and Ambrosio compactness result, it can be deduced that there is a subsequence \mathbf{u}_{n_k} of \mathbf{u}_n , and $\mathbf{u} \in \text{SBV}(\Omega)$, such that $\mathbf{u}_{n_k} \rightarrow \mathbf{u}$ in $L^2(\Omega)$, $\nabla \mathbf{u}_{n_k} \rightarrow \nabla \mathbf{u}$ in $L^2(\Omega)^d$. Therefore, $F(\mathbf{u}) \leq \liminf_{n_k \rightarrow \infty} F(\mathbf{u}_{n_k}) = \inf F$, and it can be also deduced that $\|\mathbf{u}\|_\infty \leq \|\mathbf{u}_0\|_\infty$. \square

C.1.1 Ambrosio Tortorelli Approximations

Let $X = L^2(\Omega)^2$ then the AT proposed a sequence of elliptic functionals to approximate the MS functional, the modified version of AT approximation for the proposed model (speckled distribution) is:

$$A_\sigma(\mathbf{u}, \mathbf{v}) = \begin{cases} \int_{\Omega} \left\{ \lambda \left(\ln(K\mathbf{u}) + \frac{\mathbf{u}_0}{K\mathbf{u}} \right) + \sigma |\nabla \mathbf{v}|^2 + \alpha \left(\mathbf{v}^2 |\nabla \mathbf{u}|^2 + \frac{(\mathbf{v}-1)^2}{4\alpha\sigma} \right) \right\} dx dy, \\ \text{if } (\mathbf{u}, \mathbf{v}) \in W^{1,2}(\Omega)^2, 0 \leq \mathbf{v} \leq 1 \\ +\infty \quad \text{otherwise} \end{cases} \quad (\text{C.4})$$

the limiting Mumford-Shah functional is,

$$F(\mathbf{u}, \mathbf{v}) = \begin{cases} \int_{\Omega} \left(\lambda \left(\ln(K\mathbf{u}) + \frac{\mathbf{u}_0}{K\mathbf{u}} \right) + \alpha |\nabla \mathbf{u}|^2 \right) dx + \mathcal{H}^{d-1}(S_u) \text{ if } \mathbf{u} \in \text{SBV}(\Omega), \mathbf{v} = 1, \\ +\infty \quad \text{otherwise.} \end{cases}$$

The following theorem is due to Ambrosio and Tortorelli (1990) and Ambrosio and Tortorelli (1992) and is replicated here for continuity in reading.

Theorem C.1.3. A_σ Γ -convergence to F as $\sigma \rightarrow 0$ in $L^2(\Omega)$. Moreover, A_σ admits a minimizer $(\mathbf{u}_\sigma, \mathbf{v}_\sigma)$ such that up to subsequence, \mathbf{u}_σ converges to some $\mathbf{u} \in \text{SBV}(\Omega)$ a minimizer of $F(\mathbf{u}, 1)$ and $\inf A_\sigma(\mathbf{u}_\sigma, \mathbf{v}_\sigma) \rightarrow F(\mathbf{u}, 1)$.

Proof: See proof of Theorem 4 in (Bar et al., 2011) for the details. \square

From the above theorem we can conclude the existence of a minimizer for the proposed functional in (4.5).

Appendix D

A sample matlab code for the implementation of NLTV regularization with Augmented Lagrangian is shown in this section.

D.1 Sample code of Augmented Lagrangian for Non-local Total Variation

```
function split_breg_Nonlocal()
    img=mat2gray(imread('cameraman.tif')); %input image
%   img=mat2gray(imread('/home/balaji/lena.png'));%input image
    [n,m]=size(img);
    N=n*m;
    img=double(img);
    figure(1), imshow(img,[]) %Dispaly original image
    nv=0.1; %noise Variance
    noise = (gamrnd(1/nv^2, nv^2,size(img)));
    img=double(img).*noise; %noisy image
    figure(2), imshow(img,[]); %display noisy image
    img=log(img);
    u=img(:); f=img(:);
    ws=5;ps=3;ms=10;binary=false;h=15;sigma2=3.0;weight_thres=0;
    W=weights_nonlocal(img,ws,ps,ms,binary,sigma2,h,weight_thres);
    prev_u=zeros(n,m);
    b=sparse(N,N);
    v=sparse(N,N);
    conv=1; lam=.5; beta=.09; tol=1e-4;
    iter=0;
    while iter<2
        u1=(lam*f+beta*W*u-beta*nonlocal_divergence(W,v-b));
```

```

        u2=(lam + beta*sum(W,2));
        u=u1./u2;
        del_u=nonlocal_gradient(W,u);
        v=shrink2(del_u+b , beta);
        b=b+del_u-v;
        x=reshape(u,n,m);
        iter=iter+1;
    end
    x=reshape(u,n,m);
    x=exp(x);
    figure(3), imshow(x,[]);
end
%.....
function x=shrink2(del_ub,beta)
    st=sign(del_ub);
    ft=abs(del_ub);
    ft(ft>0)=ft(ft>0)-beta;
    ft(ft<0)=0;
    x=ft.*st;
end
%.....
function W=weights_nonlocal(f,ws,ps,ms,binary,sigma,h,weight_thres)
%function to construct non-local weight matrix between image pixels
% as introduced by Buades, Coll and Morel.
%
%       $W(x,y) := \exp(-d^2(\text{patch}(x),\text{patch}(y))/h^2),$ 
% where
% $d^2(\text{pach}(x),\text{pach}(y))=\text{sum}(\text{interms of } t)\{G_{\text{sigma}}(t)*(f(x+t)-f(y+t))^2\}$ 

    if (nargin==1)
        binary = false;
        sigma = 3.0;
        ws = 10;
        ps = 5;
        ms = 8;
    end
    [m, n] = size(f);

```



```

r = m*n;
G = fspecial('gaussian', [40, 40], sigma);
% Computing distance
dist = zeros((2*ws+1)*(2*ws+1), r);
padu = padarray(f, [ws ws], 'symmetric', 'both');
for i = -ws:ws
    for j = -ws:ws
        sp=padarray(f, [ws-i ws-j], 'symmetric', 'pre');
        shiftpadu=padarray(sp, [ws+i ws+j], 'symmetric', 'post');
        tempu = (padu-shiftpadu);
        % tempu(r,c)=f(r,c)-f(r+i,c+j);
        tempu = tempu(1+ws:m+ws, 1+ws:n+ws);
        padtempu = padarray(tempu, [ps, ps], 'symmetric', 'both');
        uu = conv2(padtempu.^2, G, 'same');
        uu = uu(1+ps:m+ps, 1+ps:n+ps);
        k=(j+ws)*(2*ws+1)+i+ws+1;
        dist(k, :) = reshape(uu, 1, []);
    end
end
% Computing the weight
W = sparse(r, r);
idx = (0:r-1)';
idx = idx*(2*ws+1)^2;
%Assign a large value->don't count that pixel itself
dist(dist==0) = 1e+5;
for i = 1 : ms
    [y, minindex]= min(dist);% choose the ms smallest distance
    % position in the vector image f
    ind1 = [1:r]';
    minindex = minindex';
    y1=floor((minindex-1)/(2*ws+1));
    ind2=y1*(m-2*ws-1)+minindex+ind1-ws-1-ws*m;
    tmpindex = find(ind2>0 &ind2<=r);
    if (binary)
        W=W+sparse(ind1(tmpindex), ind2(tmpindex), 1, r, r);
    else
        values = max(exp(-y(tmpindex)/h^2), weight_thres);
    end
end

```

```

        W=W+sparse(ind1(tmpindex),ind2(tmpindex),values,r,r);
    end
    idx2 = idx + minindex; % position in the matrix dist
    %assign inf so that we can come to the next smallest distance
    dist(idx2) = inf;
end
end
%.....
function grad=nonlocal_gradient(W,I)
    N = length(I(:));
    [row,col,~] = find(W);
    z = sparse(row,col, I(col)-I(row),N,N);
    % fgrad = f(z,tau);
    grad = z.*sqrt(W);
end
%.....
function div = nonlocal_divergence( W, v )
% function that computes the non-local divergence of vector v
    N = size( W, 1 );
    in = sqrt(W).*v;
    in = in - in';
    div = in*ones(N,1);
    return
end

```

Bibliography

- Aja-Fernández, S. and Alberola-López, C. (2006). "On the estimation of the coefficient of variation for anisotropic diffusion speckle filtering". *Image Processing, IEEE Transactions on*, 15(9), 2694–2701.
- Ambrosio, L. (1988). "A compactness theorem for a special class of functions of bounded variation". Scuola normale superiore.
- Ambrosio, L., Fusco, N., and Pallara, D. (2000). "Functions of bounded variation and free discontinuity problems", 254. Clarendon Press Oxford.
- Ambrosio, L. and Tortorelli, V. (1992). "On the approximation of free discontinuity problems". *Bollettino dell'Unione Matematica Italiana*, 6(1), 105–123.
- Ambrosio, L. and Tortorelli, V. M. (1990). "Approximation of functional depending on jumps by elliptic functional via t -convergence". *Communications on Pure and Applied Mathematics*, 43(8), 999–1036.
- Amirmazlaghani, M. and Amindavar, H. (2012). "A novel sparse method for despeckling SAR images". *IEEE Transactions on Geoscience and Remote Sensing*, 50(12), 5024–5032.
- Argenti, F., Bianchi, T., Lapini, A., and Alparone, L. (2012). "Fast MAP despeckling based on Laplacian–Gaussian modeling of wavelet coefficients". *IEEE Geoscience and remote sensing letters*, 9(1), 13–17.
- Aubert, G. and Aujol, J.-F. (2008). "A variational approach to removing multiplicative noise". *SIAM Journal on Applied Mathematics*, 68(4), 925–946.
- Aubert, G. and Kornprobst, P. (2002). "Mathematical problems in image processing, volume 147 of Applied Mathematical Sciences".
- Bar, L., Chan, T. F., Chung, G., Jung, M., Kiryati, N., Mohieddine, R., Sochen, N., and Vese, L. A. (2011). "Mumford and shah model and its applications to image seg-

- mentation and image restoration". In *Handbook of mathematical methods in imaging*, 1095–1157. Springer.
- Bertero, M. and Boccacci, P. (1998). *"Introduction to inverse problems in imaging"*. CRC press.
- Bini, A. and Bhat, M. (2013). "A fourth-order Partial Differential Equation model for multiplicative noise removal in images". In *Emerging Trends in Communication, Control, Signal Processing & Computing Applications (C2SPCA), 2013 International Conference on*, 1–5. IEEE.
- Bruniquel, J. and Lopes, A. (1997). "Multi-variate optimal speckle reduction in SAR imagery". *International journal of remote sensing*, 18(3), 603–627.
- Buades, A., Coll, B., and Morel, J.-M. (2005). "A non-local algorithm for image denoising". In *2005 IEEE Computer Society Conference on Computer Vision and Pattern Recognition (CVPR'05)*, 2, 60–65. IEEE.
- Chambolle, A. (2004). "An algorithm for total variation minimization and applications". *Journal of Mathematical imaging and vision*, 20(1-2), 89–97.
- Chan, S. H., Khoshabeh, R., Gibson, K. B., Gill, P. E., and Nguyen, T. Q. (2011). "An augmented Lagrangian method for total variation video restoration". *IEEE Transactions on Image Processing*, 20(11), 3097–3111.
- Chan, T. F. and Shen, J. J. (2005). *"Image processing and analysis: variational, PDE, wavelet, and stochastic methods"*. Siam.
- Chan, T. F. and Wong, C.-K. (1998). "Total variation blind deconvolution". *IEEE transactions on Image Processing*, 7(3), 370–375.
- Chan, V. and Perlas, A. (2011). "Basics of ultrasound imaging". In *Atlas of ultrasound-guided procedures in interventional pain management*, 13–19. Springer.
- Chan, Y. K. and Koo, V. C. (2008). "An introduction to synthetic aperture radar (SAR)". *Progress In Electromagnetics Research*, 2, 27–60.
- Chang, S. G., Yu, B., and Vetterli, M. (2000). "Adaptive wavelet thresholding for image denoising and compression". *IEEE transactions on image processing*, 9(9), 1532–1546.

- Chen, B., Cai, J.-L., Chen, W.-S., and Li, Y. (2012). "A multiplicative noise removal approach based on partial differential equation model". *Mathematical Problems in Engineering*, 2012.
- Cozzolino, D., Parrilli, S., Scarpa, G., Poggi, G., and Verdoliva, L. (2014). "Fast adaptive nonlocal SAR despeckling". *IEEE Geoscience and Remote Sensing Letters*, 11(2), 524–528.
- Deledalle, C.-A., Denis, L., and Tupin, F. (2009). "Iterative weighted maximum likelihood denoising with probabilistic patch-based weights". *IEEE Transactions on Image Processing*, 18(12), 2661–2672.
- Dong, F.-F. and Liu, Z. (2009). "A new gradient fidelity term for avoiding staircasing effect". *Journal of Computer Science and Technology*, 24(6), 1162.
- Donoho, D. L. (1995). "De-noising by soft-thresholding". *IEEE transactions on information theory*, 41(3), 613–627.
- Donoho, D. L. and Johnstone, I. M. (1995a). "Adapting to unknown smoothness via wavelet shrinkage". *Journal of the american statistical association*, 90(432), 1200–1224.
- Donoho, D. L. and Johnstone, I. M. (1995b). "Adapting to unknown smoothness via wavelet shrinkage". *Journal of the american statistical association*, 90(432), 1200–1224.
- Forouzanfar, M. and Abrishami-Moghaddam, H. (2010). "Ultrasound speckle reduction in the complex wavelet domain". *Principles of Waveform Diversity and Design. SciTech Publishing an imprint of the IET*, 558–577.
- Frost, V. S., Stiles, J. A., Shanmugan, K. S., and Holtzman, J. C. (1982). "A model for radar images and its application to adaptive digital filtering of multiplicative noise". *Pattern Analysis and Machine Intelligence, IEEE Transactions on*, (2), 157–166.
- Gao, F., Xue, X., Sun, J., Wang, J., and Zhang, Y. (2016). "A SAR Image Despeckling Method Based on Two-Dimensional S Transform Shrinkage". *IEEE Transactions on Geoscience and Remote Sensing*, 54(5), 3025–3034.
- Geman, S. and Geman, D. (1984). "Stochastic relaxation, Gibbs distributions, and the Bayesian restoration of images". *IEEE Transactions on Pattern Analysis and Machine Intelligence*, (6), 721–741.

- Gilboa, G. and Osher, S. (2008). "Nonlocal operators with applications to image processing". *Multiscale Modeling & Simulation*, 7(3), 1005–1028.
- Giusti, E. (1984). "Minimal surfaces and functions of bounded variation". *Monogr. Math.*, 80.
- Goldstein, T., Bresson, X., and Osher, S. (2010). "Geometric applications of the split Bregman method: segmentation and surface reconstruction". *Journal of Scientific Computing*, 45(1-3), 272–293.
- Goldstein, T. and Osher, S. (2009). "The split Bregman method for L1-regularized problems". *SIAM journal on imaging sciences*, 2(2), 323–343.
- Gomez, L., Ospina, R., and Frery, A. C. (2017). "Unassisted quantitative evaluation of despeckling filters". *Remote Sensing*, 9(4), 389.
- Goodman, J. W. (1976). "Some fundamental properties of speckle*.". *JOSA*, 66(11), 1145–1150.
- Gunturk, B. K. and Li, X. (2012). *"Image restoration: fundamentals and advances"*. CRC Press.
- Hadamard, J. and Morse, P. M. (1953). "Lectures on Cauchy's problem in linear partial differential equations". *Physics Today*, 6, 18.
- Hansen, P. C., Nagy, J. G., and O'leary, D. P. (2006). *"Deblurring images: matrices, spectra, and filtering"*, 3. Siam.
- Hervet, E., Fjortoft, R., Marthon, P., and Lopes, A. (1998). "Comparison of wavelet-based and statistical speckle filters". In *Remote Sensing*, 43–54.
- Huang, L.-L., Xiao, L., and Wei, Z.-H. (2010). "Multiplicative noise removal via a novel variational model". *Journal on Image and Video Processing*, 2010, 1.
- Huang, Y.-M., Ng, M. K., and Wen, Y.-W. (2009). "A new total variation method for multiplicative noise removal". *SIAM Journal on Imaging Sciences*, 2(1), 20–40.
- Iijima, T. (1962). "Basic theory on normalization of pattern (in case of typical one-dimensional pattern)". *Bulletin of the Electrotechnical Laboratory*, 26(1), 368–388.
- Jia, R.-Q., Zhao, H., and Zhao, W. (2009). "Convergence analysis of the Bregman method for the variational model of image denoising". *Applied and Computational Harmonic Analysis*, 27(3), 367–379.

- Jidesh, P. (2014). "A convex regularization model for image restoration". *Computers & Electrical Engineering*, 40(8), 66–78.
- Jidesh, P. and Bini, A. (2013). "A complex diffusion driven approach for removing data-dependent multiplicative noise". In *International Conference on Pattern Recognition and Machine Intelligence*, 284–289. Springer.
- Jin, Z. and Yang, X. (2011). "A variational model to remove the multiplicative noise in ultrasound images". *Journal of Mathematical Imaging and Vision*, 39(1), 62–74.
- K. Dabov, A. Foi, V. K. and Egiazarian, K. (2007). "Image denoising by sparse 3D transform-domain collaborative filtering". *IEEE Transactions on Image Processing*, 16(8), 2080–2095.
- Kornprobst, P., Deriche, R., and Aubert, G. (1999). "Image sequence analysis via partial differential equations". *Journal of Mathematical Imaging and Vision*, 11(1), 5–26.
- Krissian, K., Kikinis, R., Westin, C.-F., and Vosburgh, K. (2005). "Speckle-constrained filtering of ultrasound images". In *Computer Vision and Pattern Recognition, 2005. CVPR 2005. IEEE Computer Society Conference on*, 2, 547–552. IEEE.
- Krissian, K., Westin, C.-F., Kikinis, R., and Vosburgh, K. G. (2007). "Oriented speckle reducing anisotropic diffusion". *Image Processing, IEEE Transactions on*, 16(5), 1412–1424.
- Kuan, D. T., Sawchuk, A. A., Strand, T. C., and Chavel, P. (1985). "Adaptive noise smoothing filter for images with signal-dependent noise". *Pattern Analysis and Machine Intelligence, IEEE Transactions on*, (2), 165–177.
- Kuttikkad, S. and Chellappa, R. (2000). "Statistical modeling and analysis of high-resolution synthetic aperture radar images". *Statistics and Computing*, 10(2), 133–145.
- Le, T., Chartrand, R., and Asaki, T. J. (2007). "A variational approach to reconstructing images corrupted by Poisson noise". *Journal of mathematical imaging and vision*, 27(3), 257–263.
- Lee, J.-S. (1980). "Digital image enhancement and noise filtering by use of local statistics". *Pattern Analysis and Machine Intelligence, IEEE Transactions on*, (2), 165–168.

- Li, H.-C., Hong, W., Wu, Y.-R., and Fan, P.-Z. (2013). "Bayesian wavelet shrinkage with heterogeneity-adaptive threshold for SAR image despeckling based on generalized gamma distribution". *IEEE Transactions on Geoscience and Remote Sensing*, 51(4), 2388–2402.
- Li, Y., Gong, H., Feng, D., and Zhang, Y. (2011). "An adaptive method of speckle reduction and feature enhancement for SAR images based on curvelet transform and particle swarm optimization". *IEEE Transactions on Geoscience and Remote Sensing*, 49(8), 3105–3116.
- Liu, J., Huang, T.-Z., Xu, Z., and Lv, X.-G. (2013). "High-order total variation-based multiplicative noise removal with spatially adapted parameter selection". *JOSA A*, 30(10), 1956–1966.
- Liu, Q., Liu, J., Xiong, B., and Liang, D. (2014). "A non-convex gradient fidelity-based variational model for image contrast enhancement". *EURASIP journal on advances in signal processing*, 2014(1), 154.
- Liu, X. and Huang, L. (2010). "Split Bregman iteration algorithm for total bounded variation regularization based image deblurring". *Journal of Mathematical Analysis and Applications*, 372(2), 486–495.
- Liu, X. and Huang, L. (2012). "Total bounded variation-based Poissonian images recovery by split Bregman iteration". *Mathematical Methods in the Applied Sciences*, 35(5), 520–529.
- Lixin, Z. and Deshen, X. (2008). "Staircase effect alleviation by coupling gradient fidelity term". *Image and Vision Computing*, 26(8), 1163–1170.
- Lu, T., Li, S., Fang, L., and Benediktsson, J. A. (2016). "SAR image despeckling via structural sparse representation". *Sensing and Imaging*, 17(1), 2.
- Lu, Y. (2017). "Out-of-focus Blur: Image De-blurring". *arXiv preprint arXiv:1710.00620*.
- Lysaker, M., Lundervold, A., and Tai, X.-C. (2003). "Noise removal using fourth-order partial differential equation with applications to medical magnetic resonance images in space and time". *Image Processing, IEEE Transactions on*, 12(12), 1579–1590.
- Mumford, D. and Shah, J. (1989). "Optimal approximations by piecewise smooth functions and associated variational problems". *Communications on pure and applied mathematics*, 42(5), 577–685.

- North, H. and Yu, O. (2001). "An edge-preserving filter for imagery corrupted with multiplicative noise". *Photogrammetric engineering and remote sensing*, 67(1), 57–64.
- Parrilli, S., Poderico, M., Angelino, C. V., and Verdoliva, L. (2012). "A nonlocal SAR image denoising algorithm based on LLMSE wavelet shrinkage". *IEEE Transactions on Geoscience and Remote Sensing*, 50(2), 606–616.
- Perona, P. and Malik, J. (1990). "Scale-space and edge detection using anisotropic diffusion". *Pattern Analysis and Machine Intelligence, IEEE Transactions on*, 12(7), 629–639.
- Ranjani, J. J. and Thiruvengadam, S. (2010). "Dual-tree complex wavelet transform based SAR despeckling using interscale dependence". *IEEE Transactions on Geoscience and Remote Sensing*, 48(6), 2723–2731.
- Rudin, L., Lions, P.-L., and Osher, S. (2003). "Multiplicative denoising and deblurring: Theory and algorithms". *Geometric Level Set Methods in Imaging, Vision, and Graphics*, 103–119.
- Rudin, L. I., Osher, S., and Fatemi, E. (1992). "Nonlinear total variation based noise removal algorithms". *Physica D: Nonlinear Phenomena*, 60(1), 259–268.
- Sheng, Y. and Xia, Z.-G. (1996). "A comprehensive evaluation of filters for radar speckle suppression". In *Geoscience and Remote Sensing Symposium, 1996. IGARSS'96. Remote Sensing for a Sustainable Future., International*, 3, 1559–1561. IEEE.
- Shi, J. and Osher, S. (2008). "A nonlinear inverse scale space method for a convex multiplicative noise model". *SIAM Journal on imaging sciences*, 1(3), 294–321.
- Shi, M. (2016). "Image Restoration Using the Alternation Direction Method Based on the Gradient Cepstrum Analysis PSF Estimation Strategy". In *Proceedings of the 2015 International Conference on Communications, Signal Processing, and Systems*, 725–732. Springer.
- Solbo, S. and Eltoft, T. (2004). "Homomorphic wavelet-based statistical despeckling of SAR images". *IEEE Transactions on Geoscience and Remote Sensing*, 42(4), 711–721.
- Stergiopoulos, S. (2000). *Advanced signal processing handbook: theory and implementation for radar, sonar, and medical imaging real time systems*. CRC press.

- Sumaiya, M. and Kumari, R. S. S. (2017). "SAR image despeckling using heavy-tailed Burr distribution". *Signal, Image and Video Processing*, 11(1), 49–55.
- Sun, Q., Hossack, J. A., Tang, J., and Acton, S. T. (2004). "Speckle reducing anisotropic diffusion for 3D ultrasound images". *Computerized Medical Imaging and Graphics*, 28(8), 461–470.
- Tuthill, T., Sperry, R., and Parker, K. (1988). "Deviations from Rayleigh statistics in ultrasonic speckle". *Ultrasonic imaging*, 10(2), 81–89.
- Wang, Y., Yang, J., Yin, W., and Zhang, Y. (2008). "A new alternating minimization algorithm for total variation image reconstruction". *SIAM Journal on Imaging Sciences*, 1(3), 248–272.
- Wang, Y., Yin, W., and Zhang, Y. (2007). "A fast algorithm for image deblurring with total variation regularization".
- Wang, Z., Bovik, A. C., Sheikh, H. R., and Simoncelli, E. P. (2004). "Image quality assessment: from error visibility to structural similarity". *IEEE transactions on image processing*, 13(4), 600–612.
- Wei, S. and Xu, H. (2009). "Staircasing reduction model applied to total variation based image reconstruction". In *Signal Processing Conference, 2009 17th European*, 2579–2583. IEEE.
- Weickert, J. (1997). "A review of nonlinear diffusion filtering". In *International Conference on Scale-Space Theories in Computer Vision*, 1–28. Springer.
- Xiao, L., Huang, L.-L., and Roysam, B. (2010). "Image variational denoising using gradient fidelity on curvelet shrinkage". *EURASIP Journal on Advances in Signal Processing*, 2010(1), 398410.
- Yahya, N., Kamel, N. S., and Malik, A. S. (2014). "Subspace-based technique for speckle noise reduction in ultrasound images". *Biomedical engineering online*, 13(1), 154.
- You, Y.-L. and Kaveh, M. (2000). "Fourth-order partial differential equations for noise removal". *Image Processing, IEEE Transactions on*, 9(10), 1723–1730.
- Yu, X., Wu, C., Wang, L., and Qi, Y. (2011). "An improved total variation model with adaptive local constraints and its applications to image denoising, deblurring and inpainting". *J. Int. J. Digit. Content Technol. Appl*, 5(12), 170–177.

Yu, Y. and Acton, S. T. (2002). "Speckle reducing anisotropic diffusion". *Image Processing, IEEE Transactions on*, 11(11), 1260–1270.

LIST OF PUBLICATIONS

Journal Publications

- [1] P. Jidesh and Balaji B. “Image despeckling with non-local total bounded variation regularization”, *Computers and Electrical Engineering (Elsevier)*, Vol. 70, Pages 631-646, 2018 Published online : DOI: <http://dx.doi.org/10.1016/j.compeleceng.2017.09.013>
- [2] P. Jidesh and Balaji B., “Adaptive non-local level-set model for despeckling and deblurring of Synthetic Aperture Radar imagery”, *International Journal of Remote Sensing*, Published online, <https://www.tandfonline.com/doi/full/10.1080/01431161.2018.1460510> DOI: <https://doi.org/10.1080/01431161.2018.1460510>,

Conference Proceedings

- [1] B.Balaji and P. Jidesh, “Non-local Gradient Fidelity Model for Multiplicative Gamma Noise Removal”, ICAPR-2017, ISI Bangalore, IEEE proceedings.

BIO-DATA

Name : Balaji Banothu
Email Id : balajiwgl@gmail.com
Contact No : +91-8971027077/9989520454
Date of Birth : June 05, 1984
Permanent address : S/o. Sevyu Banothu,
(Vi) Dubba Thanda,
(Post) Veeraram,
(Mad) Maripeda,
(Dist) Mahabubabad,
(State) Telangana, India,
Pin Code-506315.

Educational Qualifications:

Degree	Course Duration	Year of Passing	University
B.Sc. Mathematics	3 Years	2005	Kakatiya University, Warangal.
M.Sc. Mathematics	2 Years	2008	Kakatiya University, Warangal
M.Tech. Computer Science and Data Processing	2 Years	2010	IIT Kharagpur, Kharagpur